Titre: Title:	Paramètres pour l'instabilité fluidélastique : dérivées de stabilité et amortissement diphasique
Auteur: Author:	Constant Charreton
Date:	2014
Type:	Mémoire ou thèse / Dissertation or Thesis
Référence: Citation:	Charreton, C. (2014). Paramètres pour l'instabilité fluidélastique : dérivées de stabilité et amortissement diphasique [Mémoire de maîtrise, École Polytechnique de Montréal]. PolyPublie. https://publications.polymtl.ca/1677/

URL de PolyPublie: PolyPublie URL:	https://publications.polymtl.ca/1677/
Directeurs de recherche: Advisors:	Stéphane Étienne, Annie Ross, & Michel Pettigrew
Programme: Program:	Génie mécanique

UNIVERSITÉ DE MONTRÉAL

PARAMÈTRES POUR L'INSTABILITÉ FLUIDÉLASTIQUE : DÉRIVÉES DE STABILITÉ ET AMORTISSEMENT DIPHASIQUE

CONSTANT CHARRETON
DÉPARTEMENT DE GÉNIE MÉCANIQUE
ÉCOLE POLYTECHNIQUE DE MONTRÉAL

MÉMOIRE PRÉSENTÉ EN VUE DE L'OBTENTION
DU DIPLÔME DE MAÎTRISE ÈS SCIENCES APPLIQUÉES
(GÉNIE MÉCANIQUE)
SEPTEMBRE 2014

UNIVERSITÉ DE MONTRÉAL

ÉCOLE POLYTECHNIQUE DE MONTRÉAL

Ce mémoire intitulé :

PARAMÈTRES POUR L'INSTABILITÉ FLUIDÉLASTIQUE : DÉRIVÉES DE STABILITÉ ET AMORTISSEMENT DIPHASIQUE

présenté par : CHARRETON Constant
en vue de l'obtention du diplôme de : Maîtrise ès sciences appliquées
a été dûment accepté par le jury d'examen constitué de :

M. VÉTEL Jérôme, Doct., président
M. ÉTIENNE Stéphane, Doct., membre et directeur de recherche
Mme ROSS Annie, Ph. D., membre et codirectrice de recherche
M. PETTIGREW Michel, post. grad. Dipl., membre et codirecteur de recherche
M. TEYSSEDOU Alberto, Ph. D., membre

À Éther et Poséidon,

REMERCIEMENTS

Je tiens à remercier chaleureusement mes trois directeurs de recherche, Stéphane Étienne pour son expertise et sa confiance, Annie Ross pour sa rigueur et ses encouragements, et Michel Pettigrew pour sa grande expérience industrielle. Leur encadrement et complémentarité ont été bénéfiques pour l'aboutissement de ce travail.

Plus particulièrement, un grand merci à Cédric Béguin dont les ressources et connaissances ont été d'une aide inestimable. Nos discussions n'ont eu de cesse de faire mûrir mon intérêt pour ce sujet industriel.

Merci à Étienne qui a aussi enduré ces deux années bien chargées pour le meilleur et le pire, sans oublier Jean-Michel, Samy, Eliott, Marion, François et toute la gang de méca. Grâce à tous, travailler dans le labo a pris une toute autre dimension !

Je n'oublie pas tous mes amis pour leur intérêt et soutien. Je pense à Tix, Thibs, Leif', Fauve, Flo, Julz, LV, Rico, Simon, Victor, Isa, Fab, et tous les autres !

Je tiens aussi à remercier le soutien financier de Babcock & Wilcox Canada, l'Énergie Atomique du Canada Limitée et le Conseil de Recherches en Sciences Naturelles et en Génie du Canada.

Enfin, merci à Allison et à toute ma famille pour leurs encouragements.

RÉSUMÉ

Les échangeurs de chaleur et générateurs de vapeur sont des organes cruciaux pour le fonctionnement des centrales nucléaires. Ils se composent de milliers de tubes conduisant l'eau issue du réacteur, chauffée par la fission. Cette chaleur est transmise à un second circuit d'eau externe aux tubes. L'eau du circuit secondaire se change alors en vapeur pour alimenter les turbines et générer ainsi de l'électricité. Lors du changement de phase, l'écoulement diphasique (liquide/vapeur) transverse aux tubes cause différents phénomènes vibratoires sur les tubes. Ceux-ci peuvent être préjudiciables à l'intégrité structurale du générateur de vapeur et sont responsables d'arrêts de production des centrales. Une compréhension accrue des paramètres en jeu conduirait à une meilleure prédiction de la durée de vie des générateurs de vapeur.

Un des phénomènes vibratoires les plus destructeurs est sans conteste l'instabilité fluidélastique car elle conduit à des collisions entre les tubes de l'échangeur. Ceci peut mener à une usure prématurée par frottement, à des fissurations par fatigue, puis à des fuites d'eau radioactive. Ainsi, il est crucial de savoir prédire les conditions menant à l'instabilité, afin de contrôler la dégradation des tubes. Dans ce mémoire, nous visons à identifier les paramètres d'intérêt pour prédire l'instabilité fluidélastique. Pour ce faire, nous nous appuyons sur un modèle théorique, le modèle quasi-stationnaire. On montre que l'équation de prédiction de la vitesse critique d'instabilité comprend deux paramètres compliqués à déterminer. Il s'agit de la dérivée du coefficient de portance sur un cylindre d'une part, et de l'amortissement d'autre part. L'objectif principal de ce projet est la mesure expérimentale de ces deux paramètres.

Nous avons mesuré expérimentalement la dérivée du coefficient de portance car son signe est une condition suffisante pour déterminer l'existence de l'instabilité fluidélastique. L'étude expérimentale a été menée pour des nombres de Reynolds faibles et modérés dans un faisceau de tubes avec un écoulement monophasique. Ceci comble le vide de la littérature où l'on ne trouve que des valeurs à des nombres de Reynolds très élevés. En parallèle, des méthodes numériques sont utilisées. Elles sont fondées sur une résolution numérique directe des équations de Navier-Stokes par la méthode des éléments finis, et sur la théorie des écoulements potentiels. Les résultats pour la dérivée du coefficient portance sont comparés à nos expériences, ainsi que celles de la littérature. De surcroît, ces méthodes numériques permettent d'étudier l'influence de paramètres géométriques du faisceau sur la dérivée du coefficient de portance.

La tendance des résultats montre que la dérivée du coefficient de portance devient indépendante du nombre de Reynolds à haut régime. À l'aide de valeurs de la littérature, une relation pour ce paramètre en fonction du nombre de Reynolds est proposée. Elle est injectée

dans le modèle quasi-stationnaire pour tenter de prédire le seuil d'instabilité. Des cartes de stabilité pour différentes valeurs du nombre de Reynolds sont proposées, en utilisant des valeurs typiques d'amortissement pour les tubes. Aucun test de stabilité n'a été effectué pour de faibles nombres de Reynolds, aussi de tels tests permettraient de confirmer ces cartes à bas Reynolds. À plus haut régime, les prédictions ne concordent pas avec les tests de stabilité de la littérature. Il semble que le modèle quasi-stationnaire ne représente pas la réalité.

En pratique, une bonne estimation de l'amortissement total d'un tube est nécessaire pour savoir où se placer sur la carte de stabilité. Or, dans les générateurs de vapeur, l'écoulement diphasique induit un amortissement beaucoup plus important qu'en monophasique, et dont l'origine reste inconnue. Par conséquent, nous avons caractérisé l'amortissement diphasique au moyen d'une section d'essais, pour un écoulement interne. En effet, de précédentes études suggèrent que le mécanisme d'amortissement diphasique est similaire pour un tube en écoulement transverse et pour un écoulement interne. Notre étude se concentre sur la compréhension du mécanisme dissipatif en jeu.

Le banc d'essais est un système masse-ressort soumis à un écoulement diphasique vertical interne. Il est soumis à une force d'excitation sinusoïdale externe en direction transverse. Le taux d'amortissement est extrait à partir de la fonction de réponse en fréquence du tube rigide oscillant. Le banc d'essais permet de faire varier des paramètres d'excitation tels que la fréquence ou la force d'excitation. En parallèle, le mouvement de la phase gazeuse est caractérisé au moyen du traitement de vidéos du tube oscillant. L'amplitude relative du mouvement des bulles est reliée aux valeurs d'amortissement diphasique via un modèle théorique de forces sur les bulles.

Les mesures d'amortissement diphasique confirment la nature visqueuse (proportionnelle à la vitesse) de cette dissipation et sa dépendance avec la transition d'écoulement, observée antérieurement. La combinaison des vidéos et du modèle analytique suggère que la puissance dissipée par la force de traînée sur les bulles joue un rôle prédominant dans le mécanisme d'amortissement diphasique. Cependant, la sur-prédiction de l'amplitude du mouvement latéral des bulles par le modèle suggère que la pseudo-turbulence (turbulence due au mouvement des bulles) générée par le mouvement du tube est aussi un phénomène à prendre en compte.

Les résultats de cette étude constituent une base de données expérimentale pour utilisation dans des modèles théoriques d'instabilité fluidélastique. Plus particulièrement, les expériences en diphasique aideront à la validation de méthodes numériques, en ce qui concerne l'amortissement diphasique et le comportement de la phase gazeuse. Ce travail aide ainsi à la modélisation et à la compréhension des vibrations induites par les écoulements diphasiques.

ABSTRACT

Heat exchangers and steam generators are crucial components in nuclear power plants. Water heated by nuclear fission is flowing through thousands of tubes inside a steam generator. Heat is transmitted to a second water network, external to the tubes. Steam is generated from the water of the secondary to power the turbines that produce electrical power. In this process, two-phase cross flow across the tubes causes several excitation phenomena. Vibration induced on the tubes can compromise the structural integrity of the steam generator, and can lead to power plant shutdowns. Better understanding of parameters at stake would lead to improved power plant safety and reliability.

Fluidelastic instability is without doubt one of the most destructive vibration phenomena. It causes the steam generator tubes to collide against one another. This can lead to premature wear on the tubes, cracks due to fatigue and eventually, leaks leading to radioactive water contamination. Therefore, predicting conditions leading to fluidelastic instability would allow to control the damage on the tubes. In this thesis, we aim at identifying the key parameters to predict fluidelastic instability. To do so, a theoretical approach is based on the quasi-steady model. It is shown that the equation used to predict fluidelastic instability comprises two parameters that are hard to characterize. There is, on one hand, the derivative of the lift coefficient on a cylinder, and damping on the other hand. The main objective of this project is to measure these parameters experimentally.

Knowing that the sign of the lift coefficient derivative is a sufficient indicator of fluidelastic instability, this derivative was measured. The experiments were carried out on the center tube of an array. The flow is single-phase and values of Reynolds number are low to moderate, thus filling a gap in the literature. Indeed, the lift coefficient derivative is known for high values of the Reynolds number only. Meanwhile, numerical methods are developed. They are based on the direct resolution of Navier-Stokes equations with the finite-element method, and on potential flow theory. Results for the lift coefficient derivative are compared to the measurements. Furthermore, the influence of geometric parameters of the array are investigated.

The trend in the results show that the derivative of the lift coefficient becomes Reynolds independent for high values. From the literature and the measurements, a relationship is proposed for the lift coefficient derivative with respect to the Reynolds number. Values are injected in the quasi-steady model to predict the critical velocity for the onset of instability of a single flexible tube. Stability maps for various Reynolds numbers are proposed, using typical values for the tube damping. However, the maps do not compare well with critical

velocities found in the literature for high values of the Reynolds number. Stability tests would be necessary to confirm the validity of the maps for low Reynolds, as fluidelastic has never been investigated in this range of Reynolds number. Yet, for high values of the Reynolds number, it seems like the quasi-steady model fails to predict the behavior of the experiments.

An accurate value for the total damping of a tube is required to locate instability results on a map. However, in steam generators subjected to two-phase flow, damping on a tube is much more important than for single-phase flow. Yet, its origin is unknown. Therefore, we measured two-phase damping for internal flow using a specific test section. Indeed, a few studies on two-phase flow suggest that the damping mechanism is the same for a tube in cross-flow and for a tube subjected to internal flow. The present study focuses on the physics underlying the two-phase damping mechanism.

The test bench consists of a sliding rigid tube subjected to upward internal two-phase flow. It essentially is a mass-spring system subjected to a transverse sinusoidal force. The damping is extracted from the frequency response function of the tube. Meanwhile, gas phase motion is characterized through video processing of the oscillating tube. The relative amplitude of the gas phase is related to two-phase flow damping values via a model of the forces acting on the bubbles.

Varying excitation parameters such as frequency and excitation force confirms that two-phase damping is a viscous (velocity dependent) dissipation mechanism. Its direct relation with flow pattern transitions was confirmed. Furthermore, the combination of the videos and the analytical model suggests that the power dissipated by the drag force on the bubbles is significant in the two-phase damping mechanism. However, the model over-predicts the amplitude of the gas phase. This suggests that pseudo-turbulence generated by the motion of the tube is to be considered.

The results of this study form an experimental database that can be used as input for fluidelastic instability models. Particularly, two-phase flow experiments will eventually help validating numerical methods, regarding the damping as well as the behavior of the gas phase. This work contributes to modeling and understanding two-phase flow induced vibration.

TABLE DES MATIÈRES

LISTE DES TABLEAUX

LISTE DES FIGURES

LISTE DES ANNEXES

LISTE DES SIGLES ET ABRÉVIATIONS

c	Coefficient d'amortissement
C_D	Coefficient de traînée (*drag*)
C_L	Coefficient de portance (*lift*)
D	Diamètre
F	Force
f	Fréquence
k	Constante de raideur
P	Distance inter-tubes (*pitch*)
Q	Débit volumique
m	Masse
Re	Nombre de Reynolds
U	Vitesse du fluide
V	Volume
We	Nombre de Weber
β	Fraction volumétrique
δ	Décrément logarithmique
ζ	Ratio d'amortissement
ε	Taux de vide
ρ	Masse volumique
σ	Tension de surface
χ	Aplatissement de la bulle
ω	Pulsation

Indices

a	Ajoutée (masse)
b	Bulle
c	Critique (vitesse)
g	Gaz
l	Liquide
n	Naturelle (*e.g.* fréquence naturelle)
s	Structure
2φ	Diphasique
∞	À l'infini

Abréviations

AVB	*Anti-Vibration Bars*
DNS	*Direct Numerical Simulation*
FEI	*Fluidelastic Instability*
IFE	Instabilité Fluide-Élastique
VIV	Vibrations Induites par Vortex (ou *Vortex-Induced Vibration*)

D'autres variables sont définies directement dans les articles. Elles ne sont pas indiquées ici par souci de clarté, étant donné que certaines notations diffèrent d'un article à l'autre.

CHAPITRE 1

INTRODUCTION

Les phénomènes d'interaction fluide-structure sont courants. Ils se retrouvent dans des cas anodins comme un drapeau flottant au gré du vent ou le mouvement des algues marines sous l'effet de l'onde, mais conduisent aussi à des applications industrielles. On peut citer le dimensionnement d'un gratte-ciel ou d'une hélice de bateau. L'interaction fluide-structure fait le pont entre la mécanique des solides et des fluides dans le sens qu'elle aspire à trouver les équations du mouvement des corps solides sous l'action des forces exercées par le fluide. Souvent, le fluide est à l'origine de vibrations de la structure ; on parle alors de vibrations induites par les écoulements.

1.1 Mise en contexte

Nous nous intéressons aux vibrations qui existent dans les générateurs de vapeur des centrales nucléaires. Ceux-ci sont composés d'une myriade de tubes en forme de U conduisant de

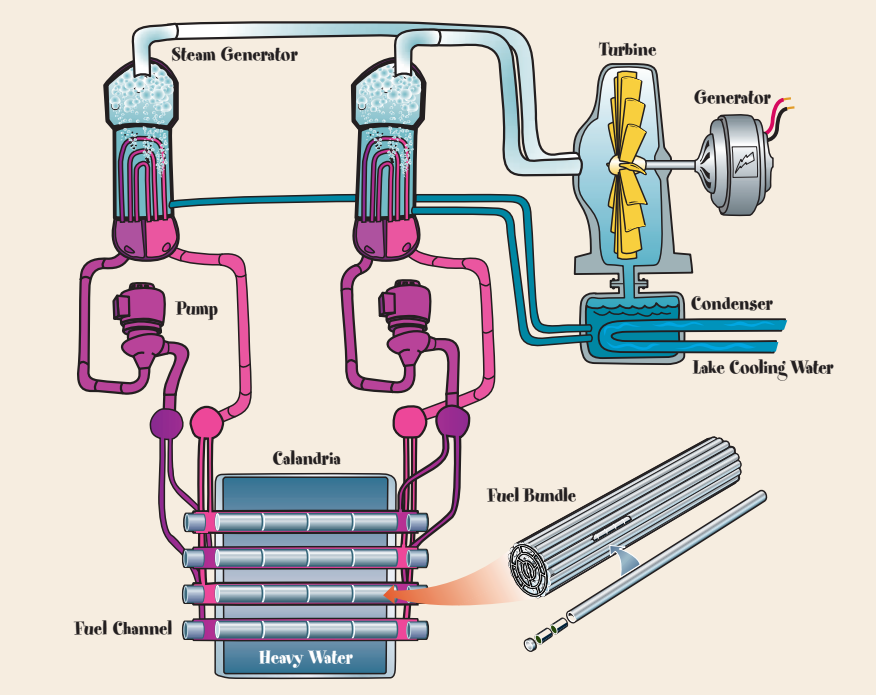

Figure 1.1 Schéma de principe d'une centrale nucléaire CANDU.

l'eau à haute température issue du réacteur (circuit en mauve sur la Fig. 1.1) et par l'intermédiaire desquels la chaleur est transmise au circuit secondaire (circuit bleu). L'eau du circuit secondaire ainsi chauffée se change en vapeur et s'élève dans le générateur de vapeur. Trois

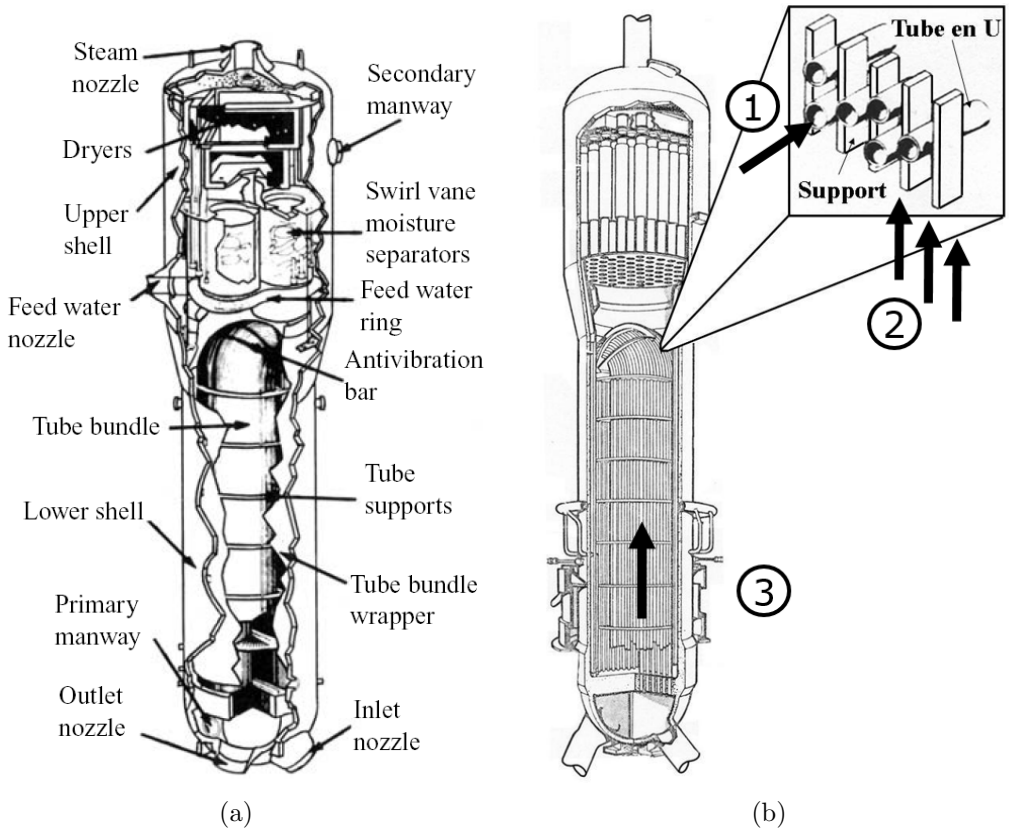

Figure 1.2 (a) : Anatomie d'un générateur de vapeur, Païdoussis (1980). (b) : Les trois catégories d'écoulement dans un générateur.

catégories d'écoulement responsables de vibrations ont été identifiées sur la Fig 1.2(b) : ① : l'écoulement monophasique axial interne du circuit primaire dans les tubes ; ② : écoulement diphasique transverse à l'apex des tubes (partie en U) ; ③ : axial externe autour de la partie verticale des tubes. C'est l'écoulement transverse qui génère le plus de vibrations. Des AVB (*anti-vibration bars*) sont installées pour limiter l'amplitude des vibrations. En contrepartie, les tubes s'usent progressivement par frottement sur leurs supports et des fissures par fatigue peuvent survenir (les supports et AVB sont définis sur la Fig. 1.2(a)). Ceci est nuisible car des fissures peuvent mener à une pollution du circuit secondaire par l'eau irradiée du circuit primaire. Il est globalement admis que le phénomène vibratoire le plus critique est l'Instabilité Fluide-Élastique (IFE). Elle résulte d'un couplage fort entre le fluide diphasique et les tubes, et est caractérisée par un mouvement des tubes de grande amplitude menant à la

dégradation du générateur sur quelques années. Depuis une quarantaine d'années, l'objectif de la recherche est de trouver des modèles pour prédire la vitesse critique menant à l'instabilité. Des modèles monophasiques démontrent une assez bonne corrélation avec les résultats expérimentaux. Cependant, les écoulements considérés sont diphasiques par nature, ce qui complique considérablement l'étude. Il est donc important d'avoir une bonne connaissance des écoulements diphasiques et de leur interaction avec les tubes pour prédire adéquatement les phénomènes de vibration dans les échangeurs.

Les écoulements diphasiques représentent 50% des écoulements industriels (Pettigrew et Taylor, 1994). Cela concerne tous les systèmes frigorifiques qui utilisent le changement de phase, ou les *risers* (tubes prolongateurs) des plates-formes pétrolières. Dans le cas des échangeurs de chaleur de centrales nucléaires, il s'agit d'un écoulement eau-vapeur. Les paramètres liés au caractère diphasique dépendent significativement du taux de vide (rapport entre le volume occupé par la phase gazeuse et le volume total) et de la configuration de l'écoulement. De plus, les paramètres de couplage entre le fluide et la structure dépendent autant des conditions d'écoulements que de la structure considérée. La détermination de ces paramètres se fait au moyen de bancs d'essais spécifiques.

1.2 Objectifs de recherche

Un des objectifs ultimes de la Chaire en Interaction Fluide-Structure de l'École Polytechnique de Montréal est de prédire l'instabilité fluidélastique en écoulement diphasique. Pour cela, le groupe de recherche s'appuie sur des modèles qui ont été développés pour des écoulements monophasiques. Cela étant, la migration de ces modèles passe par la mainmise des paramètres empiriques en diphasique et leur influence sur la vitesse critique d'instabilité.

En parallèle, des méthodes numériques, reposant sur la théorie des écoulements potentiels ou la résolution des équations de Navier-Stokes sous certaines hypothèses, aspirent à reproduire l'IFE. Ces modèles sont attrayants car ils nécessitent beaucoup moins de données expérimentales. Cependant, ils s'appuient sur des relations de fermeture pour décrire les interactions entre les fluides et la structure. Ces relations comprennent notamment les forces interfaciales entre les deux phases (masse ajoutée, traînée et portance sur les bulles par exemple). Afin d'utiliser correctement ces relations de fermeture, une bonne compréhension des phénomènes physiques en écoulement diphasique est nécessaire. Cette compréhension passe par des expérimentations. En outre, les résultats expérimentaux constituent une base de données expérimentales pour la validation des méthodes numériques.

Nous proposons deux objectifs de recherche pour ce mémoire :

– Identifier les paramètres d'influence pour l'instabilité fluidélastique.

– Mesurer expérimentalement ces paramètres et caractériser les mécanismes physiques en jeu, expliquant les résultats.

1.3 Organisation du mémoire

Ce mémoire présente les résultats expérimentaux dégagés au cours de cette maîtrise.

Lors du chapitre suivant, une revue de littérature met l'accent sur un modèle monophasique d'IFE dans le but d'identifier les paramètres d'intérêt pour notre étude. Il s'agit des dérivées de stabilité dans un faisceau de tubes d'une part, et de l'amortissement diphasique d'autre part. Nous verrons en quoi l'instabilité fluidélastique est le pont qui relie ces deux travaux.

Le chapitre 3 prend la forme d'un article de journal. Il synthétise le travail expérimental sur les dérivées de stabilité. Des comparaisons avec les valeurs obtenues à l'aide de différentes méthodes numériques, ainsi que les valeurs de la littérature, sont commentées. Enfin, l'injection des valeurs mesurées dans un modèle théorique d'IFE permet de proposer des cartes de stabilité pour différents nombres de Reynolds.

Le chapitre 4 est aussi un article soumis à un journal. Il présente une nouvelle section d'essai du laboratoire qui avait été conçue spécifiquement pour mesurer l'amortissement diphasique en faisant varier de nombreux paramètres. Un modèle analytique et le traitement de vidéos de la phase gazeuse donnent des informations sur le mécanisme d'amortissement.

Enfin, le chapitre 5 est complémentaire au chapitre sur l'amortissement. Il justifie certains choix d'expérimentations et énonce les difficultés rencontrées lors d'expériences supplémentaires.

CHAPITRE 2

REVUE CRITIQUE DE LA LITTÉRATURE

2.1 Vibrations dans les échangeurs de chaleur

L'engouement pour la recherche dans le domaine des vibrations dans les échangeurs provient d'un besoin réel de l'industrie des centrales nucléaires. Les problèmes rencontrés étaient récurrents et similaires d'une centrale à l'autre. Heureusement, ces dysfonctionnements ont été publiés dans des rapports, ce qui a quelque peu facilité la recherche au cours des dernières années (Païdoussis, 2006). Comme nous l'avons dit précédemment, les catégories d'écoulement responsables de vibrations sont les écoulements externes axiaux, externes transverses et internes axiaux, dans le cas des générateurs de vapeur (Païdoussis, 1983). Ce sont nénamoins les écoulements transverses à travers la partie verticale des tubes en U qui génère le plus de vibrations. On modélise cette zone critique par un écoulement à travers un faisceau de cylindres. Il existe quatre configurations de faisceaux correspondant à différents designs de générateurs, décrits dans la Fig. 2.1.

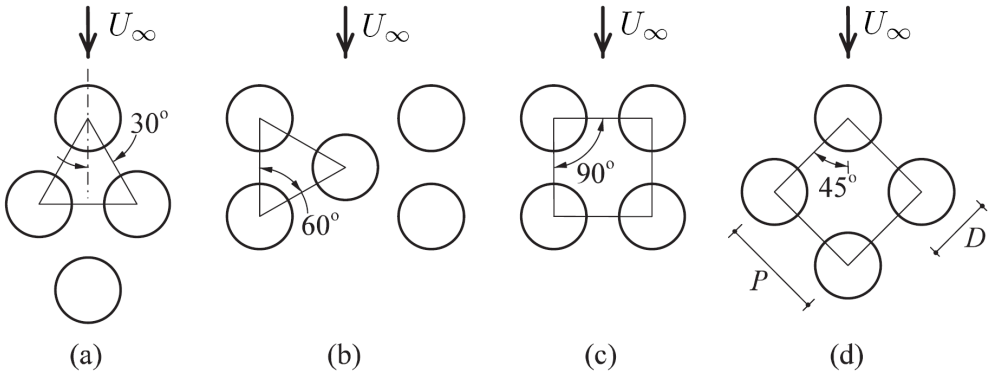

Figure 2.1 Les quatre configurations de faisceaux typiques. (a) : triangulaire normale, (b) : triangulaire tournée (ou *parallel triangular*), (c) : carré normal, (d) : carré tourné (Païdoussis *et al.*, 2011).

La Fig. 2.2 présente trois des principales sources de vibrations dans un faisceau en fonction de la vitesse de l'écoulement. Le pic d'amplitude central correspond aux fluctuations dues aux détachements tourbillonnaires. Aussi appelés tourbillons de Von Karman, ils apparaissent en aval d'un cylindre placé dans un écoulement monophasique. Lorsque la vitesse de l'écoulement augmente, des vortex se forment derrière le cylindre et se détachent alternativement de chaque

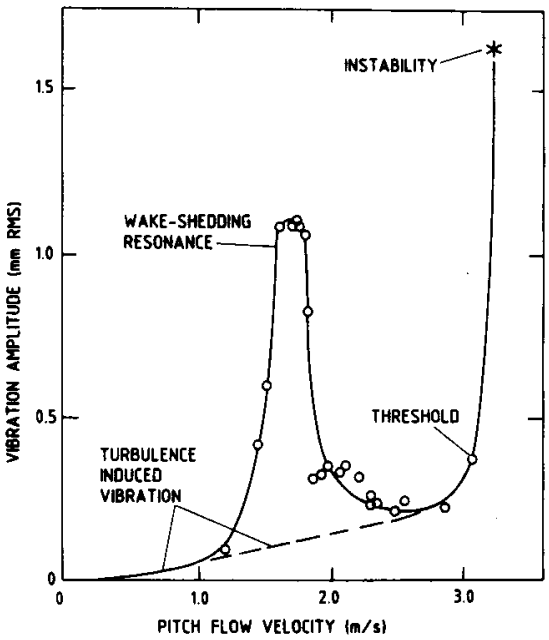

Figure 2.2 Amplitude RMS des vibrations dans un échangeur de chaleur, Gorman (1978).

côté, en un sillage caractéristique. Les fluctuations de pression qui en découlent sont à l'origine de vibrations du cylindre. On parle alors de vibrations induites par les vortex (VIV). Le phénomène est caractérisé par le nombre de Strouhal donné par :

$$S = \frac{fD}{U} \tag{2.1}$$

où f est la fréquence de détachement des vortex, D le diamètre du tube et U la vitesse du fluide. La fréquence des vortex augmente avec la vitesse du fluide. Si on atteint la fréquence naturelle des cylindres, on observe un pic de résonance. Si on augmente encore U, on voit que le phénomène se tarit. Il convient de noter qu'en écoulement diphasique, les bulles ont tendance à casser la formation des vortex, donc ce phénomène a moins d'importance et est absent pour des taux de vide entre 15% et 85%. Par ailleurs, dans le cas de l'écoulement transverse, le *pitch* (écart entre les tubes) est généralement trop petit pour avoir un sillage de vortex pleinement développé. Cependant, des forces fluctuantes dites "quasi-périodiques" apparaissent, mais leur nature n'est pas encore parfaitement comprise aujourd'hui (Perrot, 2011).

On remarque aussi une composante de vibrations qui semble augmenter linéairement avec la vitesse. Il s'agit des vibrations dues à la turbulence de l'écoulement liées aux fluctuations aléatoires de pression dans le fluide. L'effet est d'autant plus important que l'écoulement

est diphasique (Pettigrew et Taylor, 1994). Il convient de noter que les deux phénomènes de vibrations présentés sont à l'origine d'usure par frottement des tubes au niveau de leurs supports, et l'apparition de fuites par fatigue. Les tubes défectueux sont bouchés. Lorsque 15% des tubes sont condamnés, le générateur de vapeur est remplacé. L'usure est accélérée dans des conditions d'instabilité fluidélastique qui est largement reconnue comme le phénomène le plus critique et difficile à caractériser.

Le phénomène d'IFE est prépondérant dans les faisceaux de tubes avec écoulement transverse, où l'instabilité peut se produire aussi bien dans la direction de la traînée que de la portance (Violette *et al.*, 2006). Elle peut survenir lorsque les cylindres prennent plus d'énergie au fluide qu'ils ne peuvent en restituer, d'où des oscillations d'amplitude croissante. Contrairement aux VIV et aux vibrations dues à la turbulence, l'instabilité entraîne une collision généralisée des tubes menant à la destruction de l'échangeur sur plusieurs années. De nombreux travaux expérimentaux présentent des vitesses critiques d'instabilité. On peut citer entre autres Weaver et Fitzpatrick (1988) et Pettigrew et Taylor (1991) qui ont le mérite de proposer des recommandations pour la conception des échangeurs de chaleur. Il apparaît que la vitesse critique d'instabilité dépend autant de la géométrie (*pitch*, configuration du faisceau, diamètre des tubes...) que du fluide (mono/diphasique, vitesse, amortissement...). Ceci complique considérablement l'étude et nécessite le développement de modèles pour tenter de cerner le mécanisme.

2.2 Instabilité fluidélastique

De nombreux modèles d'IFE ont été développés au cours des quarante dernières années et reposent souvent sur des considérations physiques différentes. Bien que nous nous intéresserons surtout au modèle quasi-stationnaire, il semble judicieux de présenter les autres par souci d'exhaustivité et pour voir le mécanisme sous plusieurs approches. Les modèles les plus usités sont rassemblés dans la très bonne revue de Price (1995). Les dernières années ont été surtout marquées par des modèles non linéaires, et donnent généralement des meilleurs résultats. Ils sont généralement dérivés des modèles proposés ci-après, qui ont l'avantage d'expliquer physiquement l'IFE de manière simple. Certains modèles non linéaires sont néanmoins cités dans le chapitre 3.

2.2.1 Modèles monophasiques

Jet-switch

Il s'agit d'un modèle semi-analytique développé par Roberts (1966). Il considère que le fluide entre deux cylindres constitue un jet orienté par leurs sillages respectifs. Ce jet a

tendance à alimenter les deux zones de recirculation derrière les cylindres, affectant ainsi leur distribution de pression. En oscillant, les tubes ont tendance à changer la direction du jet, d'où une variation des forces de traînée pouvant mener à une instabilité. Ce modèle ne prévoit l'instabilité que dans la direction de l'écoulement. Cette approche fondée sur l'observation du comportement du fluide introduit des notions inhérentes à l'instabilité fluidélastique comme l'hystérésis du coefficient de pression.

Quasi-statiques

Les modèles quasi-statiques utilisent l'hypothèse que les conditions de l'écoulement sont les mêmes pour des cylindres oscillants que pour des cylindres statiques à une position correspondant à un instant donné. Les forces sont mesurées expérimentalement et reliées ensuite à la vitesse critique d'instabilité. Connors (1970) propose une équation de prédiction pour la vitesse critique exprimée comme suit :

$$\frac{U_c}{f_n D} = K \left(\frac{m\delta}{\rho D^2} \right)^n \tag{2.2}$$

où U_c [1] est la vitesse critique, f_n la fréquence naturelle d'un tube, D son diamètre, $m/\rho D^2$ la masse réduite et δ le décrément logarithmique du tube. On mesure δ en étudiant les vibrations libres du cylindre sous écoulement. Il caractérise l'enveloppe de la décroissance après un déplacement initial ou un impact. Les paramètres K et n ont été déterminés expérimentalement. La simplicité de cette équation a séduit les industriels et elle constitue un critère de design, bien que son utilisation fasse l'objet de controverse (Price, 2001). En effet, la valeur $K = 9.9$ proposée par Connors n'est valable que pour une seule rangée de tubes. Blevins (1974) a étendu la validité du modèle aux faisceaux de tubes et a trouvé des valeurs différentes selon les configurations. C'est finalement Pettigrew *et al.* (1978) qui ont proposé la valeur de 3.3 qui représente correctement la majorité des cas et qui a constitué un critère de conception largement utilisé dans l'industrie nucléaire. Cela dit, cette constante empirique K trahit un manque d'information du phénomène physique en jeu.

Instationnaires

Le principe de ces modèles consiste à mesurer directement les forces instationnaires sur les cylindres oscillants. Ces travaux ont été effectués par Tanaka et Takahara (1980), Tanaka et Takahara (1981) et Tanaka *et al.* (1983) pour plusieurs ratios P/D et démontrent dans chaque cas une excellente corroboration des modèles avec les expériences. C'est ensuite Chen (1983) qui dériva des expressions analytiques des coefficients de forces. Il identifia alors deux mécanismes d'instabilité dynamique, un troisième étant de nature statique :

1. Généralement, la vitesse de référence est la vitesse de *pitch* définie par $U = U_\infty P/(P-D)$ où U_∞ est la vitesse d'écoulement libre, et P le *pitch*.

(i) Instabilité contrôlée par l'amortissement : pour ce mécanisme, les forces fluides sont en phase avec la vitesse du cylindre, contrairement au cas d'un amortissement visqueux "classique" où le cylindre a tendance à s'opposer au mouvement. La particularité de ce mécanisme est qu'un tube à un degré de liberté peut devenir instable même si les tubes avoisinant sont fixes. Nous détaillerons ce mécanisme à titre d'illustration dans la Sec. 2.2.2.

(ii) Instabilité contrôlée par la rigidité : il faut au moins deux cylindres flexibles pour que cette instabilité apparaisse. Ce sont alors les termes couplés (extra-diagonaux) de la matrice de rigidité qui peuvent avoir un effet déstabilisant. Il est fréquent qu'une "instabilité soit due à une combinaison de ces deux mécanismes" (Païdoussis *et al.*, 2011). Les paramètres des faisceaux de tubes donnent cependant plus d'importance au mécanisme (ii).

(iii) Instabilité statique : alors que les deux instabilités précédentes sont dynamiques, un autre mécanisme statique peut survenir. Il s'agit de l'instabilité statique contrôlée par la raideur. Elle apparait lorsque la raideur équivalente du cylindre devient négative. Cependant, comme les cylindres sont généralement soumis à un mouvement oscillatoire, ce mécanisme n'a été que très rarement observé (Païdoussis *et al.*, 1989).

Bien que cette théorie colle bien à la réalité, elle nécessite un très grand nombre de données expérimentales, à tel point que Price et Païdoussis (1984) suggèrent que les modèles fondés sur une hypothèse quasi-statique méritent d'être approfondis, toujours dans un but de compréhension du phénomène. C'est de là que naissent les modèles quasi-stationnaires.

Quasi-stationnaires

On compte deux grandes améliorations qui constituent le modèle quasi-stationnaire de Price et Païdoussis (1984). La première provient de la prise en compte du temps que le fluide met à parcourir l'espacement (*pitch*) entre deux cylindres. Ceci les conduit à définir le déplacement "apparent" des cylindres, sorte de déplacement relatif qui tient compte du retard du fluide. Le second effet avait déjà été mis en évidence par Simpson et Flower (1977) et correspond au ralentissement du fluide à l'approche d'un tube. Le retard τ qui en découle signifie que le fluide en contact avec le cylindre à un instant t aurait impacté à un instant $t - \tau$ dans des conditions purement stationnaires. La prise en compte de ces phénomènes fait apparaître des dérivées de stabilité, soit les dérivées spatiales des coefficients de forces dans les directions de la traînée et de la portance. Ces dérivées de stabilité sont d'autant plus importantes que les forces sont très sensibles à de petits déplacement des cylindres. Elles doivent être déterminées expérimentalement. Les modèles quasi-stationnaires montrent aussi une bonne concordance avec les résultats expérimentaux et sont populaires car ils nécessitent un nombre modéré de données expérimentales. Quelques grands thèmes de recherche au labo-

ratoire d'Interaction Fluide-Structure de Polytechnique Montréal sont d'ailleurs l'extension de ce modèle en diphasique ainsi que la mesure des coefficients de force et des retards.

2.2.2 Instabilité d'un cylindre avec le modèle quasi-stationnaire

Bien que le modèle quasi-stationnaire ait été généralisé pour N cylindres flexibles constituant un faisceau, on se propose de présenter le cas d'un cylindre flexible dans un faisceau rigide. C'est en effet un exemple souvent utilisé pour illustrer de manière simple l'instabilité fluidélastique, notamment dans le livre de Païdoussis *et al.* (2011). On rappelle qu'un cylindre flexible dans un faisceau rigide peut devenir instable de deux façons : instabilité **dynamique** contrôlée par l'amortissement, ou instabilité **statique** contrôlée par la raideur. On peut rajouter que les vitesses critiques d'instabilité sont similaires dans un faisceau de tubes flexibles dans certains cas (voir le chapitre 3 pour plus de détails).

Considérons un noyau de tubes au centre duquel se trouve un cylindre libre d'osciller. Si on ne considère pas de couplage dans les directions x et y, on peut écrire l'équation du mouvement dans la direction de la portance :

$$(ml\ddot{y} + c\dot{y} + ky)D = F_y \tag{2.3}$$

où $m = \rho_s \pi D^2/4$ est la masse linéique du cylindre, l sa longueur et D son diamètre, c l'amortissement du système et k la rigidité, F_y la force fluide et y le déplacement adimensionnel du cylindre (cela simplifie le développement par la suite). Il nous faut donc exprimer F_y en fonction de la géométrie du système. Le diagramme suivant (Fig. 2.3) schématise la situation.

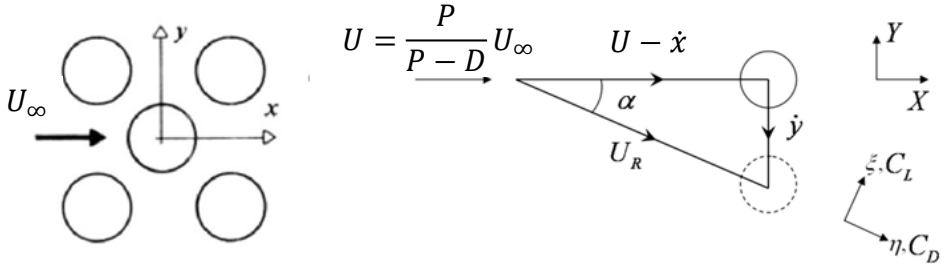

Figure 2.3 Diagramme de vitesses lors du mouvement d'un cylindre, Païdoussis *et al.* (2011).

Lorsque le cylindre se déplace, on constate un changement de l'angle d'attaque du fluide qui cause une variation des efforts de traînée et de portance. La projection fait apparaître

une composante liée à la traînée dans la force F_y :

$$F_y = \frac{1}{2}\rho U_r^2 lD \left[C_L \cos(-\alpha) - C_D \sin(-\alpha)\right] - m_a lD\ddot{y} \tag{2.4}$$

On fait donc l'hypothèse que $dU/dt = 0$; m_a est la masse ajoutée linéique. La masse ajoutée correspond à la résistance à l'accélération d'un corps dans un fluide. Elle vaut $\rho\pi D^2/4C_M$ pour un cylindre et C_M est le coefficient de masse ajoutée du cylindre. Celui-ci vaut 1 dans un milieu infini mais l'effet du confinement des tubes voisins a tendance à faire augmenter sa valeur. Pettigrew *et al.* (1989) proposent une corrélation qui tient compte du confinement et du taux de vide. Pour un écoulement monophasique, elle vaut :

$$C_M = \left[\frac{(D_e/D)^2 + 1}{(D_e/D)^2 - 1}\right] \tag{2.5}$$

Cette expression correspond à la masse ajoutée d'un cylindre confiné dans un tube. Ici, les valeurs de D_e/D ont été calculées par Pettigrew *et al.* (1989) de telle sorte que cette expression puisse être utilisée pour différentes configurations de faisceaux (l'idée vient du fait qu'un. La vitesse relative peut s'écrire :

$$U_r^2 = \left[(U - D\dot{x})^2 + (D\dot{y})^2\right]^{1/2} \tag{2.6}$$

Pour de grandes vitesses réduites, on a $\cos(-\alpha) \simeq 1$ et $\sin(-\alpha) = D\dot{y}/U_r \simeq D\dot{y}/U$. De plus, en considérant de petits déplacements, un développement en série de Taylor à l'ordre un nous donne :

$$C_L = C_{L_0} + (\partial C_L/\partial x)x + (\partial C_L/\partial y)y \tag{2.7}$$

et de même pour C_D. On note $(\partial C_X/\partial i) = C_{X,i}$. La réinjection de ces résultats permet de linéariser l'expression de la force sous la forme :

$$F_y = \frac{1}{2}\rho U^2 lD \left[C_{L_0} - 2C_{L_0}\left(\frac{\dot{x}D}{U}\right) + C_{L,x}x + C_{L,y}y - C_{D_0}\left(\frac{\dot{y}D}{U}\right)\right] - m_a lD\ddot{y} \tag{2.8}$$

C_{L_0} correspond au coefficient de portance à la position centrale du cylindre. Pour des raisons de symétrie, on a $C_{L_0} = 0$ et $\partial C_L/\partial x = 0$ d'où une simplification :

$$F_y = \frac{1}{2}\rho U^2 lD \left[C_{L,y}y - C_{D_0}\left(\frac{\dot{y}D}{U}\right)\right] - m_a lD\ddot{y} \tag{2.9}$$

On introduit alors le délai dû au déplacement du cylindre dont nous avons parlé précédem-

ment, et qui s'exprime :

$$\tau = \mu D/U \tag{2.10}$$

et correspond au temps que met le fluide pour parcourir un diamètre de cylindre, pondéré par le paramètre de retard adimensionnel $\mu \sim \mathcal{O}(1)$ (ordre de grandeur 10^0). Pour des mouvements harmoniques $y = y_0 e^{i\omega t}$, la prise en compte de ce retard fait apparaître un déphasage pour le terme en $\partial C_L/\partial y$ dans la force fluide :

$$F_y = \frac{1}{2}\rho U^2 l D \left[e^{-i\omega\tau} \left(\frac{\partial C_L}{\partial y} \right) y - C_{D_0} \left(\frac{\dot{y} D}{U_p} \right) \right] - m_a l \ddot{y} \tag{2.11}$$

L'équation du mouvement prend alors la forme :

$$\ddot{y} + \left[\left(\frac{\delta}{\pi} \right) \omega_n + \frac{1}{2} \left(\frac{\rho U D}{m + m_a} \right) C_{D_0} \right] \dot{y} + \left[\omega_n^2 - \frac{1}{2} \left(\frac{\rho U^2}{m + m_a} \right) C_{L,y} \cos(\omega\tau) + \frac{1}{2} \left(\frac{\rho U^2}{m + m_a} \right) C_{L,y} i \sin(\omega\tau) \right] y = 0 \tag{2.12}$$

où ω_n est la fréquence naturelle du cylindre sans écoulement et δ le décrément logarithmique. L'amortissement total du système correspond à la partie imaginaire de l'équation différentielle :

$$2\zeta_t \omega = \left[\left(\frac{\delta}{\pi} \right) \omega \omega_n + \frac{1}{2} \left(\frac{\rho U D}{m + m_a} \right) \omega C_{D_0} + \frac{1}{2} \left(\frac{\rho U^2}{m + m_a} \right) \left(\frac{\partial C_L}{\partial y} \right) \sin(\mu\omega D/U) \right] \tag{2.13}$$

L'amortissement étant faible, la fréquence du cylindre dans le fluide avec écoulement est :

$$\omega^2 = \omega_n^2 - \frac{1}{2} \left(\frac{\rho U^2}{m + m_a} \right) \left(\frac{\partial C_L}{\partial y} \right) \cos(\omega\tau) \tag{2.14}$$

On comprend que la fréquence du cylindre est peu affectée par de l'air, ce qui n'est plus le cas dans de l'eau par exemple, en raison de sa plus forte densité.

Le système peut alors devenir instable par amortissement négatif. Si on considère que $\mu\omega D/U$ est suffisamment petit, alors $\sin(\mu\omega D/U) \approx \mu\omega D/U$. La condition d'amortissement nul permet alors de trouver une équation de prédiction de la vitesse critique d'instabilité :

$$\frac{U_c}{f_n D} = \left[\frac{4}{-C_{D_0} - \mu(\partial C_L/\partial y)} \right] m^* \delta \tag{2.15}$$

où $m^* = (m + ma)/\rho D^2$ est le paramètre de masse.

Pour que l'instabilité existe, il faut que $-C_{D_0} - \mu(\partial C_L/\partial y) > 0$, soit $(\partial C_L/\partial y)$ (aussi noté $C_{L,y}$)< 0 et suffisamment grand en valeur absolue. Cela prouve l'importance des dérivées

de stabilité pour prédire l'instabilité. On rappelle que ces dérivées sont mesurées sur des boucles contenant un cylindre flexible au milieu d'un faisceau rigide et que l'on déplace successivement à différentes positions pour pouvoir calculer la dérivée spatiale. Ce principe repose sur l'hypothèse quasi-statique stipulant que les efforts du fluide sont les mêmes sur un tube statique et un tube oscillant. Pour l'instabilité selon y, seule la dérivée de la portance dans la direction de la portance est requise. Elle dépend du nombre de Reynolds, et les valeurs de la littérature n'existent qu'à Re de l'ordre de 10^4, correspondant au régime d'opération des échangeurs. $C_{L,y}$ est positif et vaut environ 5 si la force est adimensionnalisée par U_∞ (soit 0.56 si la force est adimensionnalisée par U_p) pour la configuration triangulaire tourné (Sawadogo et Mureithi, 2014). En revanche, Watteaux (2008) a mesuré des valeurs négatives à bas Reynolds. Aucune étude n'a été réalisée à des nombres de Reynolds modérés.

Puisqu'un des mécanisme d'instabilité est par amortissement négatif, il est crucial que l'amortissement total du système soit parfaitement modélisé. Comme nous allons le voir, l'amortissement induit par les écoulements diphasiques (non mentionné précédemment car le modèle quasi-stationnaire a été développé pour le monophasique) est prédominant et ne peut donc pas être négligé afin de bien prédire l'instabilité fluidélastique.

2.3 Amortissement dû aux écoulements diphasiques

2.3.1 Introduction aux écoulements diphasiques

Les écoulements diphasiques se retrouvent sous plusieurs formes (liquide/gaz, liquide/liquide, solide/gaz...). Nous nous intéressons aux écoulements liquide/gaz. Ils sont caractérisés principalement par le taux de vide, qui représente la proportion entre le volume de gaz et le volume total dans une section ΔL donnée :

$$\varepsilon = \frac{V_g}{V_g + V_l} = \frac{A_g \Delta L}{A_g \Delta L + A_l \Delta L} = \frac{A_g}{A_g + A_l} \tag{2.16}$$

où A_k correspond à la surface occupée par la phase k ($k = l, g$). Le taux de vide moyen est une information difficile à obtenir et requiert une instrumentation spécifique comme des sondes à capacité ou à fibres optiques. En revanche, le fraction volumétrique ne nécessite que les débits volumiques de chacune des phases :

$$\beta = \frac{Q_g}{Q_g + Q_l} = \frac{A_g \langle u_g \rangle}{A_g \langle u_g \rangle + A_l \langle u_l \rangle} = \frac{A_g}{A_g + A_l / s} \tag{2.17}$$

où s est le rapport de glissement entre les phases : $s = \langle u_g \rangle / \langle u_l \rangle$. Dans le cas où l'écoulement est parfaitement homogène ($s = 1$), on a alors $\varepsilon = \beta$. Il faut noter que le modèle d'écoule-

ment homogène est largement utilisé. Dans les graphes de la littérature présentés ci-après, la variable notée ε correspond en fait à un β "camouflé". Les différences entre ces deux variables seront largement discutées au cours du chapitre 4.

Lorsque le taux de vide augmente, le mélange diphasique va adopter différentes structures. Elles correspondent à des régimes (ou configurations) d'écoulement bien connus, comme l'atteste la Fig 2.4. Les régimes d'écoulements ont des propriétés très différentes au niveau de

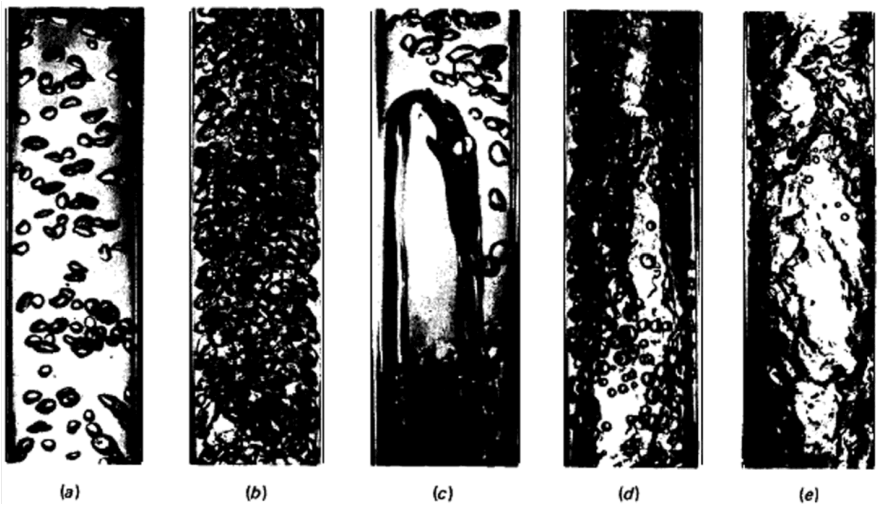

Figure 2.4 Régimes d'écoulement diphasique pour un écoulement interne ascendant. Les écoulements sont dénotés : (a) : à bulles, (b) : à bulles dispersées, (c) : à bouchons, (d) : agité, (e) : annulaire (Roumy, 1969).

l'amortissement qu'ils induisent ou du transfert thermique notamment. Les transitions entre chaque régime sont bien documentées. De nombreuses cartes existent dans la littérature.

2.3.2 Amortissement total d'une structure dans un écoulement

Le fait de plonger une structure dans un fluide va affecter le mouvement de la structure. On se place dans le cas de l'aéroélasticité où la vitesse du fluide est beaucoup plus importante que celle du solide. Cela se traduit par une condition pour la vitesse réduite : $U/fD >> 1$ (de Langre, 2002). Dans ce cas, on tient compte de l'influence du fluide sur la structure, mais pas l'inverse. On peut citer les effets de masse ajoutée, qui sont responsables d'une résistance à l'accélération d'un solide. En ce qui concerne l'amortissement, Carlucci et Brown (1983) suggèrent que l'amortissement total d'une structure est la somme de plusieurs composantes (pour un écoulement axial externe). Ils ont proposé :

$$\zeta_t = \zeta_s + \zeta_f + \zeta_v + \zeta_{2\varphi} \tag{2.18}$$

(i) ζ_s : L'amortissement **structural** dépend évidemment de la structure considérée et de ses supports. Par exemple, dans le cas d'un tube en U d'un générateur de chaleur, le taux d'amortissement tient compte des AVB. En termes de design, le jeu AVB/tubes détermine l'amortissement structural et surtout le taux d'usure, de l'ordre du mW, qui prescrit la durée de vie du générateur (Nowlan *et al.*, 2009). Généralement, ζ_s est la principale source de dissipation d'énergie. Pettigrew *et al.* (2011) identifient toutes les sources d'amortissement dans un générateur de vapeur, causées par les tubes ainsi que les supports. Il apparaît que dans certains échangeurs, 75% de l'amortissement est dû à l'amortissement par film mince (*squeeze-film damping*). Son étude est hors-sujet pour le présent travail mais il faut avoir conscience de son importance. Néanmoins, le *squeeze-film damping* n'opère qu'aux supports, alors que l'amortissement diphasique est présent tout le long des tubes et est donc vraisemblablement responsable de la majeure partie de l'énergie dissipée.

(ii) ζ_v : Le ratio d'amortissement **visqueux** représente l'effet des forces de frottement du fluide sur les parois. Il dépend principalement des propriétés du fluide, de sa vitesse et de la géométrie. Pour un tube dans un liquide stagnant, ζ_v est fonction du nombre de Stokes et du confinement :

$$\zeta_v \propto \left(\frac{\pi f D^2}{2\nu}\right)^{-0.5} \tag{2.19}$$

Des corrélations sont proposées notamment pour différents types de faisceaux mais force est de constater que les valeurs sont relativement faibles. Pour faire le lien avec l'instabilité fluidélastique d'un cylindre dans un faisceau, on peut préciser que les deux premiers termes de l'Eq. (2.13) (amortissement total du système) correspondent respectivement aux coefficients d'amortissements structural et visqueux (en effet, C_{D_0} dépend du nombre de Reynolds et donc de la viscosité).

(iii) ζ_f : Lorsqu'un tuyau est soumis à un écoulement, il peut se déformer et osciller sous les efforts fluides. Ces derniers ont alors un effet amortissant au niveau des courbures formées par la structure. C'est le mécanisme d'amortissement **fluide**. Il résulte d'un transfert d'énergie cinétique du tube vers le fluide qui dépend de l'angle du tube. De manière générale, ζ_f augmente avec la vitesse du fluide (de Langre, 2002).

(iii) $\zeta_{2\varphi}$: La composante $\zeta_{2\varphi}$ a été introduite pour compenser la différence d'amortissement total entre les écoulements mono et diphasique, ζ_t étant toujours plus important en présence de deux phases. La Fig. 2.5 illustre ce résultat pour un écoulement axial externe. Carlucci et Brown (1983) ont mesuré un amortissement maximal d'environ 2.5% entre 30 et 70% de taux de vide ε. Il faut aussi noter l'augmentation linéaire de ζ en fonction de ε.

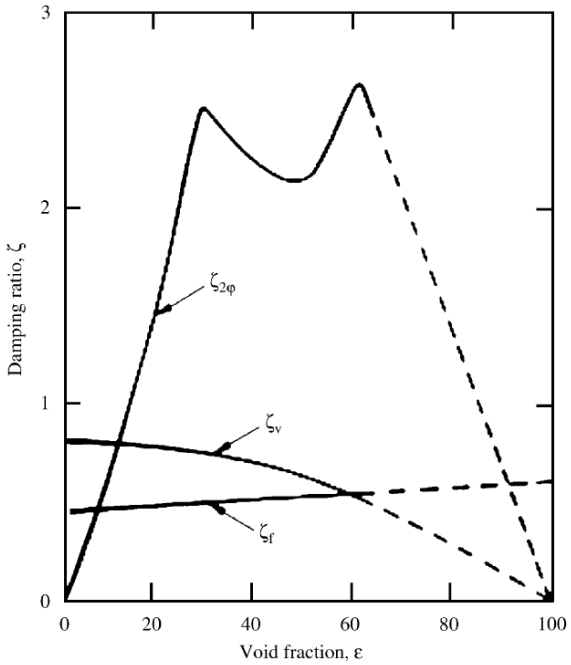

Figure 2.5 Composantes de l'amortissement en écoulement diphasique axial externe (écoulement confiné autour d'un cylindre oscillant), Carlucci et Brown (1983).

Pour le cas d'un échangeur de chaleur réel, d'autres sources d'amortissement interviennent. Nous verrons plus tard que les amortissements fluide et visqueux sont généralement négligés. L'amortissement diphasique dépend de nombreux paramètres ce qui complique sa caractérisation.

2.3.3 Amortissement diphasique et catégorie d'écoulement

On retrouve trois catégories d'écoulement dans les générateurs de vapeur : écoulement transverse, écoulement axial externe et interne. L'étude de l'amortissement diphasique est pertinente pour chacune d'entre elles.

(i) **Axial externe** : Il s'agit de l'écoulement le long de l'axe d'un cylindre, confiné dans un tube de diamètre plus grand. On retrouve cette catégorie le long de la partie verticale des tubes en U dans les générateurs de vapeur. Carlucci et Brown (1983) furent parmi les premiers à rapporter des valeurs d'amortissement diphasique pour cette catégorie d'écoulement (cf. Fig. 2.5). Le cylindre est déplacé de sa position initiale à mi-longueur avec un système mécanique ou un électroaimant. Il est ensuite relâché ; les oscillations libres du système permettent de remonter à l'amortissement grâce au décrément logarithmique. Le système permet en outre de mesurer le coefficient de masse ajoutée C_M.

En effet, la fréquence naturelle du système s'exprime par :

$$f_0 = \frac{1}{2\pi}\sqrt{\frac{k_s}{m_s + C_M * m_{2\varphi}}} \tag{2.20}$$

où k_s est la rigidité du cylindre, m_s sa masse et $m_{2\varphi}$ est la masse de fluide déplacée par le cylindre. Plus récemment, Uchiyama (2003) propose une simulation numérique de l'écoulement diphasique autour d'un cylindre et trouve des valeurs d'amortissement maximal et de masse ajoutée du même ordre de grandeur que les expériences. Il se place dans le cas d'un écoulement à bulles dont il contrôle le diamètre. L'amortissement diphasique retombe à zéro à partir de $\beta = 60\%$, alors que ce n'est absolument pas le cas expérimentalement (il est toujours de l'ordre de 1 à 2%). Ceci montre les limites de la formulation ALE (*Arbitrary Lagrangian Eulerian*) pour les hauts taux de vide car elle ne tient pas compte de la transition d'écoulement. Cela étant, la source du mécanisme d'amortissement est attribuée au déphasage entre la force de traînée agissant sur le cylindre et son déplacement. Ce déphasage est donc dû à un déplacement intrinsèque au mélange.

(ii) **Transverse** : Cet écoulement est localisé à l'apex des tubes en U. La mesure d'amortissement dans un faisceau de tubes est plus difficile. On peut utiliser la méthode du décrément logarithmique mais cela nécessite un tube instrumenté, mobile et soumis à une excitation externe. Une autre solution est l'étude des vibrations d'un cylindre sous écoulement pendant un temps relativement long. On extrait l'amortissement via l'évasement à -3 dB dans le pic de la FFT (*Fast-Fourier Transform*) du signal de déplacement du tube. Cependant, cette méthode suppose que l'excitation est aléatoire, stationnaire et d'amplitude uniforme sur une large bande de fréquences. Ceci est discutable étant donnée la nature quasi-périodique des forces fluides (Perrot, 2011).

Une autre difficulté lorsque l'on mesure l'amortissement en écoulement transverse est justement l'influence des forces fluidélastiques. On voudrait idéalement mesurer l'amortissement à la vitesse critique d'instabilité. Malheureusement, un des mécanismes d'instabilité fluidélastique est par amortissement négatif ; on trouverait donc des valeurs proches de 0 à l'orée du seuil d'instabilité. Les mesures sont donc effectuées à la moitié de U_C car en deçà, ζ varie peu (Pettigrew *et al.*, 1989). Ces valeurs sont utilisées pour les cartes de stabilité et pour nourrir les modèles théoriques. Bien que l'amortissement en écoulement transverse soit le plus crucial d'un point de vue pratique, on comprend que les montages expérimentaux se prêtent mal à la compréhension du phénomène.

Néanmoins, Pettigrew et Taylor (2004) ont compilé une base de données sur l'amortissement dans les échangeurs, et en déduisent une relation empirique que peuvent

utiliser les constructeurs de générateurs de vapeur. On remarque sur la Fig. 2.6 que l'amortissement est maximal entre 30 et 70% de taux de vide et vaut environ 5% après normalisation en fonction de la géométrie du faisceau. Là aussi, des hypothèses sont

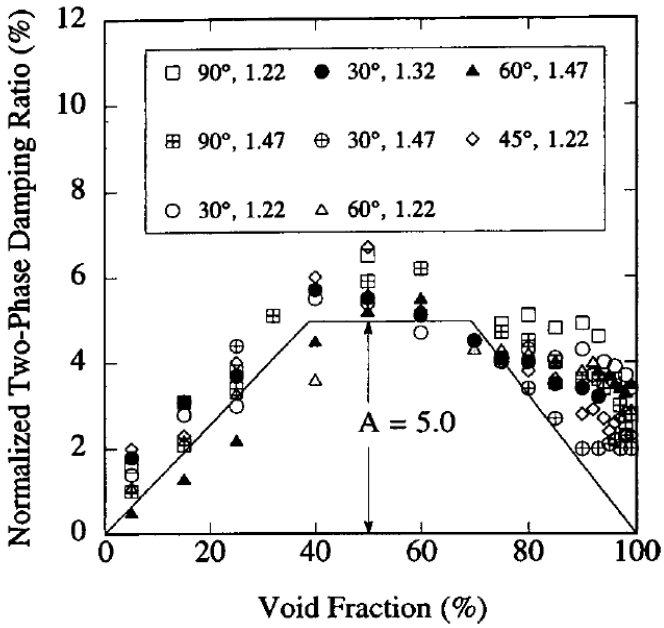

Figure 2.6 Amortissement diphasique en transverse, Pettigrew et Taylor (2004).

énoncées quant à l'origine de l'amortissement. La tension de surface joue visiblement un rôle important, c'est pourquoi la structure de l'écoulement, le mouvement relatif de la phase gazeuse dans la phase liquide, la coalescence et l'éclatement de bulles, sont suspectés.

(iii) **Interne** : L'écoulement interne est la catégorie la plus facile à étudier d'un point de vue du design du banc d'essai, c'est pourquoi elle a été sélectionnée pour étudier l'amortissement à l'École Polytechnique de Montréal. Gravelle *et al.* (2007) ont mesuré l'amortissement diphasique dans des tubes de diamètres de l'ordre de 20 mm (cf. Fig. 2.7). On retrouve une courbe semblable aux figures précédentes. Le lien entre la rupture de pente et la transition d'écoulement est explicité. En utilisant un modèle d'écoulement à bulles considérées comme des sphères rigides, ils ont mis en lumière la relation entre l'amortissement et la surface d'interface entre les deux phases. Ceci explique la rupture de la courbe d'amortissement à la transition entre les écoulements à bulles et à bouchons, la formation des bouchons diminuant l'augmentation de la surface d'interface. Ce travail a été poursuivi par Béguin *et al.* (2009) qui ont mesuré l'amortissement diphasique avec des sphères rigides en sédimentation dans un tuyau empli d'eau stagnante. Ils retrouvent la proportionnalité de l'amortissement pour l'écoulement à

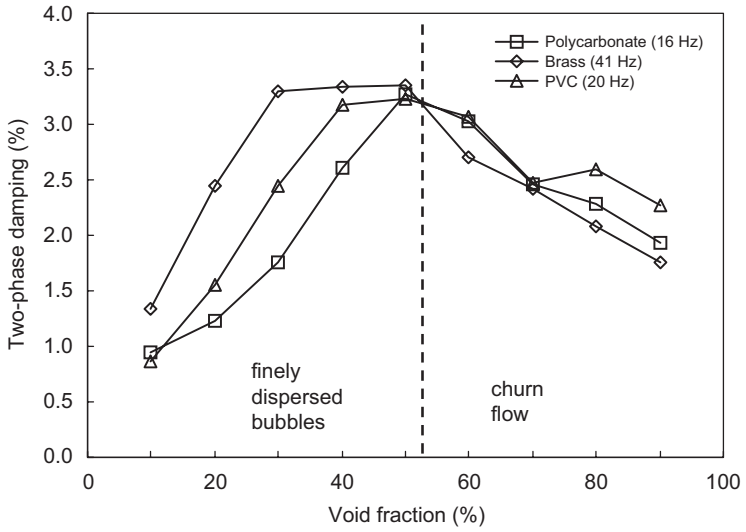

Figure 2.7 Amortissement diphasique en écoulement interne, Gravelle *et al.* (2007).

bulle, avec un changement de pente lorsque les bulles commencent à s'entrechoquer (*i.e.* début de la coalescence dans le cas d'une phase gazeuse). Par ailleurs, ils proposent un modèle analytique d'une bulle dans un cylindre, en résolvant les équations de Navier-Stokes de manière analytique autour d'une bulle, dans un tube oscillant. Ils montrent ainsi que la dissipation d'énergie s'accompagne d'un mouvement relatif entre les phases. De plus, cette dissipation serait de type visqueuse (proportionnelle à la vitesse), ce qui correspond aux observations des études précédentes.

Force est de constater que d'une catégorie d'écoulement à l'autre, les courbes de $\zeta_{2\varphi}$ vs β sont semblables. Le mécanisme semble donc être similaire, et plus particulièrement pour l'écoulement à bulles. Les observations visent le "déphasage des forces de traînée" et les "déplacements relatifs entre les phases" comme étant la cause de l'amortissement, auxquels s'ajoute la dépendance avec la surface d'interface.

2.3.4 Dépendance paramétrique

Dans leur revue de l'amortissement dans les échangeurs de chaleur, Pettigrew et Taylor (2004) réalisent une étude paramétrique de l'amortissement diphasique. Les conclusions sont les suivantes :

Vitesse du liquide : Il apparaît que l'effet de la vitesse du fluide n'est pas très importante. Elle a une influence sur la transition d'écoulement, mais assez peu sur les valeurs d'amortissement en tant que telles. Cette faible dépendance renforce l'hypothèse que l'amortissement est liée à un phénomène dans la direction de la vibration (transverse à l'écoule-

ment) ;

Taux de vide : C'est assurément le plus important, l'amortissement étant généralement maximal entre 30 et 70% de taux de vide. Les transitions d'écoulement se ressentent directement dans les courbes d'amortissement.

Fréquence du tube : Pour toutes les catégories d'écoulements confondues, les essais ont été réalisés avec des cylindres (ou tubes) de fréquence naturelle variant de 20 à 300 Hz. Malgré la dispersion des résultats à haute fréquence, les valeurs sont similaires quelle que soit f_n.

Confinement : Il a un effet, mais des fonctions de confinement existent pour les écoulements transverses et axiaux externes (Pettigrew et Taylor, 2004; Carlucci, 1980; Chen *et al.*, 1976). Elles permettent de comparer les résultats indépendamment des paramètres géométriques.

Propriétés des fluides : Pour ce qui est des écoulements transverses, l'effet de la tension de surface σ a été testé. Il apparaît que $\zeta_{2\varphi}$ augmente avec σ (Pettigrew et Knowles, 1997). L'explication donnée est que de plus grosses bulles seraient plus aptes à dissiper de l'énergie. Cependant, pour un même taux de vide, la surface d'interface serait plus importante avec des bulles plus petites. Il y a donc une dualité entre amplitude du mouvement des bulles et leur géométrie, ce qui nous incitera à étudier la grandeur qui réunit ces deux notions, c'est-à-dire le travail des forces dissipées par les bulles. Par ailleurs, Béguin *et al.* (2009) ont étudié l'influence de la viscosité et de la densité, en testant différents fluides pour les écoulements internes. Pour le cas de l'écoulement à bulles, il semble que la viscosité ait peu d'influence, contrairement à la différence de densité entre les phases (ζ augmente avec $\Delta\rho$).

Paramètres d'excitation : La majorité des expériences sur l'amortissement diphasique révèlent un amortissement de type visqueux (proportionnel à la vitesse), à cause de la décroissance exponentielle de l'enveloppe de la réponse libre du système. Le terme "dissipation visqueuse" doit sont nom à la force d'amortissement dite linéaire de type $c\dot{x}$, où c est le coefficient d'amortissement, souvent proportionnel à la viscosité du milieu (*e.g.* cylindre ou sphère en régime laminaire, $Re < 100$ environ). L'amortissement n'est évalué qu'à la fréquence naturelle du système, et bien que la faible dépendance en fréquence naturelle ait été soulignée, la fonction de réponse en fréquence d'une structure soumise à un écoulement diphasique permettrait de confirmer la nature "visqueuse" de l'amortissement. En outre, cette classification prête d'autant plus à confusion que l'amortissement diphasique ne semble pas dépendre de la viscosité du mélange !

Par ailleurs, la force d'excitation serait aussi un paramètre d'intérêt afin de déterminer jusqu'à quel niveau d'excitation l'amortissement diphasique en est indépendant.

2.4 Objectifs spécifiques

Cette revue de littérature a permis de mettre en lumière deux paramètres cruciaux pour l'étude de l'instabilité fluidélastique.

D'une part la dérivée du coefficient de portance conditionne l'instabilité par amortissement négatif d'un cylindre dans un faisceau. Cependant, l'influence du nombre de Reynolds est encore méconnue. De plus, la dispersion des résultats de la littérature suggère une forte sensibilité de ce paramètre vis-à-vis de la géométrie du faisceau. Les objectifs spécifiques de l'étude sont les suivants :

- Mesurer la dérivée spatiale du coefficient de portance pour des nombres de Reynolds modérés dans un faisceau de tubes ;
- Utiliser des méthodes numériques afin de tester l'influence des paramètres géométriques du faisceau de tube ;
- Étudier l'effet du nombre de Reynolds sur la stabilité d'un tube avec le modèle quasi-stationnaire.

Cette étude fait l'objet d'un premier article. L'auteur a utilisé une section d'essai et un protocole expérimental conçus auparavant par un ancien étudiant de la chaire (Watteaux, 2008). L'auteur a ensuite adapté un code d'écoulement potentiel de la chaire pour calculer la force et la dérivée du coefficient de portance. Ce sont les coauteurs de l'article qui étaient en charge des calculs avec la DNS. Enfin, l'auteur était en charge de l'analyse théorique de stabilité et de la rédaction de l'article.

D'autre part, les enjeux et incertitudes liés à l'amortissement diphasique ont été dégagés. Malgré les séries de tests extensives des précédentes études, son origine physique reste un mystère. Ceci justifie la conception d'un banc d'essais spécifique axé sur la mesure du mouvement relatif de la phase gazeuse, qui est le principal suspect. Les objectifs spécifiques de cette seconde étude sont les suivants :

- Mesurer l'amortissement diphasique pour différents taux de vide et confirmer la dépendance avec la configuration d'écoulement diphasique ;
- Faire varier des paramètres d'excitation (fréquence, force d'excitation...) afin de qualifier la nature de l'amortissement ;
- Caractériser le mouvement de la phase gazeuse sous oscillations de la structure ;
- Relier le mouvement relatif des bulles à l'amortissement par un modèle de forces sur les bulles.

Cette partie fait l'objet d'un second article. L'auteur était en charge de la finition et de la mise en fonctionnement d'une section d'essai conçue par le premier coauteur de l'article. Le premier auteur est à l'origine de l'intégralité du contenu de l'article, sous la supervision et

les conseils des coauteurs.

Les deux articles ont été soumis au *Journal of Fluids and Structures*. Ils ont chacun été précédés d'un article de conférence. Certains résultats ont donc été présentés lors de conférences dont les publications sont soumises à un comité de lecture.

Puisqu'il s'agit d'un mémoire par articles, le lecteur doit s'attendre à des répétitions avec la présente revue de littérature. En effet, les articles doivent pouvoir être lus en dehors du mémoire, d'où une remise en contexte dans leurs introductions qui reflète ce qui vient d'être énoncé.

CHAPITRE 3

ARTICLE 1 : EFFECT OF REYNOLDS NUMBER ON THE STABILITY OF A SINGLE FLEXIBLE TUBE PREDICTED BY THE QUASI-STEADY MODEL IN TUBE BUNDLES

Cet article a été soumis au *Journal of Fluids and Structures*.

C. Charreton, C. Béguin, K. R. Yu & S. Étienne
BWC/AECL/NSERC Chair of Fluid-Structure Interaction
Department of Mechanical Engineering, École Polytechnique,
P.O.Box 6079, succ. Centre-Ville, Montréal (Québec), Canada, H3C 3A7

Abstract

Fluidelastic instability is the most destructive phenomenon in steam generators and boilers. This phenomenon can be reproduced in laboratories by considering cylinder arrays subjected to cross-flow. For parallel triangular arrays, instability threshold of a single flexible tube is equal to that of a fully flexible bundle and thus this configuration gives useful insights at reduced costs and calculations. We use the quasi-steady model to study the stability of the central tube in a parallel triangular tube bundle. The model relies strongly on the derivative of the lift coefficient to predict the onset of the negative damping mechanism and static divergence. In this work, we study the effect of the Reynolds number on the lift coefficient derivative on the central tube, for a parallel triangular array with $P/D = 1.5$*. It was found that the lift coefficient derivative is strongly dependent on the Reynolds number when it is small. Meanwhile, numerical methods (DNS and potential) allow to investigate the effect of pitch ratio and orientation of the array. The sensitivity of the lift coefficient derivative on these parameters provides some perspective on the scatter in the data found in the literature. As a result of this study, the effect of Reynolds number on the stability of a single flexible tube is discussed. It appears that the quasi-steady model does not stand the comparison with experiments for high values of the Reynolds number.*

Keywords: Fluidelastic instability, quasi-steady, lift coefficient, tube bundle, stability derivative, Reynolds number

3.1 Introduction

Flow-induced vibration in steam generators is a major concern for the nuclear industry. As outlined by Connors (1970), three main excitation mechanisms are responsible for the vibrational response of the tubes: turbulent buffeting, vortex-induced vibrations and fluidelastic instability. Anti-vibration bars (AVB) are installed to prevent out-of-plane vibrations. However, clearances between tubes and AVBs are inevitable for design purposes. Therefore, tube-to-support and tube-to-AVB interactions in cross-flow cause fretting wear and fatigue, eventually leading to failure. A better understanding of flow-induced vibrations in tube bundles leads to power plant reliability and efficiency improvements.

The last forty years showcased most of the research on flow-induced vibrations in steam generators and heat exchangers, as reviewed by Pettigrew and Taylor (1991), Weaver and Fitzpatrick (1988), and Au-Yang *et al.* (2000). It is well accepted that fluidelastic instability (FEI) is the most critical phenomenon. It leads to very high wear rates on the tubes and sometimes more spectacularly in the destruction of several steam generator tubes (Païdoussis, 2006). The U-bend region of the tubes is subjected to cross-flow and therefore more prone to vibrations. For this reason, FEI was studied for several tube bundle configurations.

Two instability mechanisms were first identified by Chen (1983): instability controlled by damping and by stiffness.

Damping controlled instability occurs when the fluid forces are in phase with the tube velocity. This may result in total damping being negative, leading to dynamic instability. A single flexible tube in a rigid bundle can become unstable with this mechanism.

Instability controlled by stiffness requires at least two flexible tubes coupled through the fluid and is in fact a coupled mode flutter mechanism. The instability relies on the coupling terms in the stiffness matrix.

It was shown that the first mechanism is predominant for low mass-damping parameter, whereas the second occurs for higher values. A combination of both mechanisms can occur. The limit between the two is approximately at a mass-damping parameter $m^*\delta$ of approximately 300 (Price and Païdoussis, 1986); m^* is the mass ratio and δ is the logarithmic decrement.

Several models were derived for single-phase flow. Interested readers are referred to a thorough review by Price (1995). The industry has been using Connors' quasi-static model (Connors, 1970), which relates the critical velocity to the mass-damping parameter via a proportionality constant K. Despite the convenience of the formulation, it lacks physical interpretation of the phenomenon, as critically discussed by Price (2001).

On the other hand, Tanaka and Takahara (1980), Tanaka and Takahara (1981) and Tanaka

et al. (1983) developed the unsteady model. Unsteady forces were directly measured in tube bundles for various pitch-to-diameter ratios. A stability analysis is performed and excellent agreement between the model and the experiments was found. However, this method requires a tremendous amount of experimental data.

A more reasonable approach is theoretical modeling which requires only a few input parameters based on experiments. Lever and Weaver's (1982) channel flow model, and Price and Païdoussis's (1984) quasi-steady model are such examples.

Lastly, full models requiring no experimental input can be considered. Such models are based on the potential flow assumption or on the direct resolution of the Navier-Stokes equations (DNS) in tube arrays (*e.g.* Païdoussis *et al.*, 1984; Étienne and Pelletier, 2011; Plagnard *et al.*, 2014). Despite their attractiveness, they are not viable tools at this stage because of computational time, dependence of FEI on array configuration (*e.g.* pitch ratio, number of tubes...) and flow parameters.

Price and Païdoussis's (1984) quasi-steady model was selected for the present study. The fluid force on a tube is assumed to be position-dependent but is applied with a time lag. Therefore, the model requires the fluid force coefficients on the tube. It also needs the time delay which represents the time for the fluid to effectively exert its force on the tube due to its own displacement. The quasi-steady model was later generalized by Granger and Païdoussis (1996). They associated the phase lag with a memory function, which arises from diffusion-convection of the vorticity induced by the velocity of the cylinder. Several aspects support the choice of the quasi-steady model as a viable tool for the future. First, the agreement with experimental FEI values is good at the cost of reasonable amount of input data. Secondly, it has recently been extended to two-phase flows (Sawadogo and Mureithi, 2014a,b)). It was shown that theoretical results with the quasi-steady model are in good agreement with experiments and the more accurate unsteady model, provided that the time delay is adequately extracted. The quasi-steady model is thus attractive for two-phase flow, where the amount of experimental data required as input is considerably less important than for the unsteady model. Hence, some results on the fundamentals of the quasi-steady model in the present study may apply to two-phase flow.

The effect of Reynolds on FEI tresholds was studied by Chen and Srikantiah (2001) and Austermann and Popp (1995). It has a major effect for low values. Therefore, it is relevant to study the influence of the Reynolds number on the stability derivatives as input for a quasi-steady analysis.

In this paper, the effect of the Reynolds number on $C_{L,y}$ is investigated. This parameter is most important for the quasi-steady model, as demonstrated in Sec. 3.2. In Sec. 3.3, the different methods that we used to retrieve $C_{L,y}$ are presented. The results for the effect

of Reynolds number on experimental values of $C_{L,y}$ are discussed in Sec. 3.4.1. Also, the numerical methods are used to assess the influence of some geometrical parameters such as pitch ratio or the angle of configuration in Sec. 3.4.2 and Sec. 3.4.3. Finally, based on the experimental values for $C_{L,y}$, the stability of a single flexible tube predicted by the quasi-steady model in a parallel triangular array is discussed in Sec. 3.5.

3.2 Theory

Although the quasi-steady model was developped for fully flexible arrays, the particular case of a single flexible tube in a rigid array is precisely used as an example for the damping controlled instability. The development can be found in Païdoussis *et al.* (2011) and is summarized hereafter.

Consider a flexible tube in a given array on Fig. 3.1. Coupling between x and y is not accounted for, therefore the equation of motion of the cylinder in the transverse direction can be written as:

$$(ml\ddot{y} + c\dot{y} + ky)D = F_y \tag{3.1}$$

where m is the mass per unit length of the cylinder, l its length, c its damping coefficient

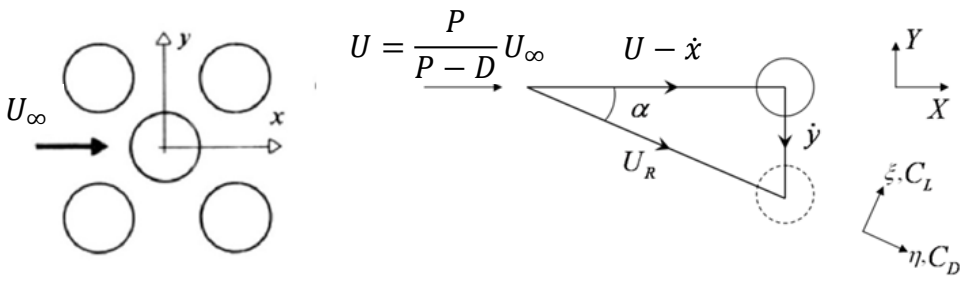

Figure 3.1 Velocity diagram of the moving cylinder.

and k its stiffness. F_y is the force of the fluid impinging on the cylinder and y is the dimensionless displacement Y/D. The displacement of the tube in Fig. 3.1 causes the drag force to contribute to the force in the transverse direction, so that:

$$F_y = \frac{1}{2}\rho U_r^2 lD\left[C_L\cos(-\alpha) - C_D\sin(-\alpha)\right] - m_a lD\ddot{y} \tag{3.2}$$

where the last term is the added mass component and m_a is the added mass per unit length.

The relative velocity of the cylinder is written as:

$$U_r^2 = (U - D\dot{x})^2 + (D\dot{y})^2 \tag{3.3}$$

For high reduced velocities, we have $\cos(-\alpha) = (U - D\dot{x})/U_r \simeq 1$ and $\sin(-\alpha) = D\dot{y}/U_r \simeq D\dot{y}/U$. Furthermore, assuming small displacements, a first-order Taylor expansion used to linearize the fluid force coefficients yields:

$$C_L = C_{L_0} + (\partial C_L/\partial x)x + (\partial C_L/\partial y)y \tag{3.4}$$

and similarly for the drag coefficient C_D. Noting that $(\partial C_X/\partial i) = C_{X,i}$, Eq. (3.2) yields:

$$F_y = \frac{1}{2}\rho U^2 lD \left[C_{L_0} - 2C_{L_0}\left(\frac{\dot{x}D}{U}\right) + C_{L,x}x + C_{L,y}y - C_{D_0}\left(\frac{\dot{y}D}{U}\right)\right] - m_a lD\ddot{y} \tag{3.5}$$

Because of symmetry, the lift coefficient C_{L_0} at the central position is equal to zero. For the same reason, $\partial C_L/\partial x = 0$. Hence:

$$F_y = \frac{1}{2}\rho U^2 lD \left[C_{L,y}y - C_{D_0}\left(\frac{\dot{y}D}{U}\right)\right] - m_a lD\ddot{y} \tag{3.6}$$

The time delay is expressed as:

$$\tau = \mu D/U \tag{3.7}$$

and is proportional to the time taken by the fluid to travel one tube diameter. It was proven that $\mu \sim \mathcal{O}(1)$ for single-phase flow (Price and Païdoussis (1984)). Assuming that the cylinder exhibits a harmonic motion $y = y_0 e^{i\omega t}$, the time delay can be artificially inserted in the fluid force equation:

$$F_y = \frac{1}{2}\rho U^2 lD \left[e^{-i\omega\tau}C_{L,y}y - C_{D_0}\left(\frac{\dot{y}D}{U}\right)\right] - m_a lD\ddot{y} \tag{3.8}$$

Since the damping is very small, the equation of motion Eq. (3.1) can be simplified as:

$$\ddot{y} + 2\zeta_t\omega\dot{y} + \omega^2 y = 0 \tag{3.9}$$

where the damping term is:

$$2\zeta_t\omega = \left[\left(\frac{\delta}{\pi}\right)\omega\omega_n + \frac{1}{2}\left(\frac{\rho U D}{m+m_a}\right)\omega C_{D_0} + \frac{1}{2}\left(\frac{\rho U^2}{m+m_a}\right)C_{L,y}\sin\left(\frac{\mu\omega D}{U}\right)\right] \tag{3.10}$$

In Eq. (3.10), ω_n is the natural frequency of the cylinder measured for no flow conditions ($\omega_n = \sqrt{k/[(m+m_a)l]}$) and δ its logarithmic decrement. Note that for high density fluids such as water, m_a has a significant influence and the change in frequency cannot be neglected. The evaluation of the added mass in tube arrays is described in Pettigrew *et al.* (1989).

As the damping is relatively small, the natural frequency in the fluid may be expressed as:

$$\omega^2 = \omega_n^2 - \frac{1}{2}\left(\frac{\rho U^2}{m+m_a}\right)C_{L,y}\cos\left(\frac{\mu\omega D}{U}\right) \tag{3.11}$$

The first term of Eq. (3.10) is a structural damping term and the second is the dissipation due to the fluid. Both are positive, but the third term, which exists because of the inserted time delay, can become negative. Therefore, negative damping instability is triggered. The condition $\zeta_t = 0$ prescribes the instability threshold. For high reduced velocities, $\sin(\mu\omega D/U)$ can be approximated by $\mu\omega D/U$. This leads to:

$$\frac{U_c}{f_n D} = \left[\frac{4}{-C_{D_0} - \mu C_{L,y}}\right] m^*\delta \tag{3.12}$$

where U_c is defined as the critical pitch fluid velocity for the onset of FEI, and m^* is the mass ratio $(m+m_a)/(\rho D^2)$. Assuming that $\mu = 1$ for single-phase flow, $C_{L,y}$ should be negative and large for FEI to occur. The derivative of the lift coefficient is usually determined experimentally by statically displacing the cylinder in the lift direction and measuring the induced lift force. This is based on the quasi-steady assumption which stipulates that forces on a static cylinder and on an oscillating cylinder are the same. Eq. (3.12) shows the importance of $C_{L,y}$ to predict FEI due to the negative damping mechanism. It depends on many parameters such as Reynolds number, array configuration, pitch ratio or tube position.

Note that stiffness-controlled instability may also occur for a single flexible tube. It is a static divergence instability that can happen when the equivalent stiffness ($\omega = 0$) of Eq. (3.9) is equal to 0. It leads to:

$$\frac{U_c}{f_n D} = \left[\frac{8\pi^2}{C_{L,y}}\right]^{1/2}[m^*]^{1/2} \tag{3.13}$$

The study of tube bundle with a single flexible cylinder has proven to be relevant not

only for academical purposes, but also for design. Price and Païdoussis (1986) showed that adjacent tubes have a major effect on the stability of the flexible tube, even though they are rigid. Moreover, based on experimental evidence and their theoretical model, Weaver and Lever (1977), Lever and Weaver (1986a), Lever and Weaver (1986b) showed that a single flexible tube becomes unstable at fairly the same velocity as in a fully flexible array. More recently, Khalifa *et al.* (2012) reviewed in the literature the work related to the study of single flexible tubes in an array. In their comprehensive review, they showed that this observation seems to be consistent especially for the parallel triangular array configuration. They also emphasized the importance of the position of the tube, the middle one in the third row being the most prone to instability. In the present study, we are precisely investigating the lift coefficient derivative of this particular cylinder for the same array configuration. Moreover, the parallel triangular array becomes unstable for lower reduced velocities than other arrays (Pettigrew *et al.*, 2002). Hence, its stability threshold is a conservative value for all the other bundles.

As underlined by Chen and Srikantiah (2001), the effect of Reynolds number on force coefficients has often been neglected since it is not predominant for high values of the Reynolds number. However, for lower values, the effect cannot be neglected. Even at high values of the Reynolds number, studies reporting values for $C_{L,y}$ in the literature are unfortunately very sparse, as shown in Tab. 3.1.

Table 3.1 Literature review on the lift coefficient derivative.

Bundle configuration	Reference	P/D	Fluid	Row	$Re \times 10^3$	$C_{L,y}$
Parallel triangular	Price and Païdoussis (1984)	1.375	Air	3	68	-243
	Mahon and Meskell (2012)	1.375	Air	6	$20-98$	$[-3.2,\ 0.2]$
	Sawadogo and Mureithi (2014a)[1]	1.5	Water	7	84	0.56
Normal triangular	Mahon and Meskell (2009)	1.32	Air	3	$22-112$	$[2,\ 2.3]$
		1.58	Air	3	$22-102$	$[1.1,\ 2.4]$
		1.97	Air	3	$22-98$	$[-0.1,\ 2.1]$
	Païdoussis *et al.* (1993)	1.375	Air	3	38	-180.6
	Gillen and Meskell (2009)[1]	1.32	NUM	3	$42-210$	$[-1.1,\ -0.2]$
Rotated square	Price and Païdoussis (1986)	2.12	Air	3	–	3.7
Normal square	Price and Païdoussis (1986)	1.5	Air	2	–	-73

[1] Results that were originally presented in terms of freestream velocity U_∞ were recalculated in terms of pitch velocity U in the present table, with $U = U_\infty \times P/(P-D)$.

3.3 Determination of the lift coefficient derivative

3.3.1 Experimental determination

Test section description

A small test section was designed to specifically retrieve $C_{L,y}$. It is an array of 7 tubes and 6 half-tubes on the sides in parallel triangular (rotated 30°) configuration (cf. Fig. 3.2). The

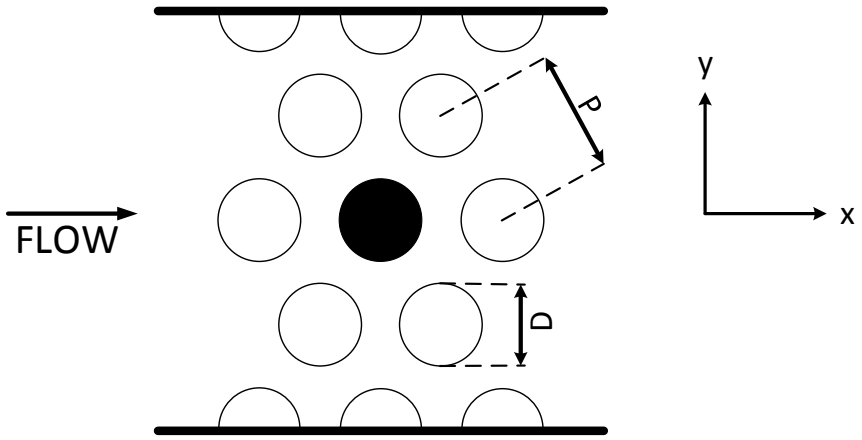

Figure 3.2 Schematic of the experimental tube bundle. It is a parallel triangular configuration of five rows. The black central tube (3^{rd} row) is instrumented. It can be statically displaced in the lift (y) and drag (x) directions from $-8\%D$ to $+8\%D$.

section is arranged horizontally. Its main characteristics are summarized in Tab. 3.2. The

Table 3.2 Characteristics of the array.

Property	Notation	Value
Tube diameter	D	25.4 mm (1")
Pitch ratio	P/D	1.5
Width/Height	$2L$	100 mm (3.9")
Aspect ratio	$-$	1 (for the test section)

central cantilevered tube is equipped with two pairs of strain gages. These strain gages are connected in half-bridge and measure moments of drag and lift. The central tube is mounted on two linear sliders. Therefore, it can be statically displaced in the x and y directions from $-8\%D$ to $+8\%D$.

This system was previously operated with pure glycerin to reach very low Reynolds numbers (below 30) by Watteaux *et al.* (2007). In the present study, glycerin was diluted twice (5 and 10% in volume) to allow for larger values of the Reynolds number. The viscosity μ_l of each glycerin solution was characterized with a rheometer as a function of temperature.

The hydraulic loop that contains the test section is represented on Fig. 3.3. Glycerin

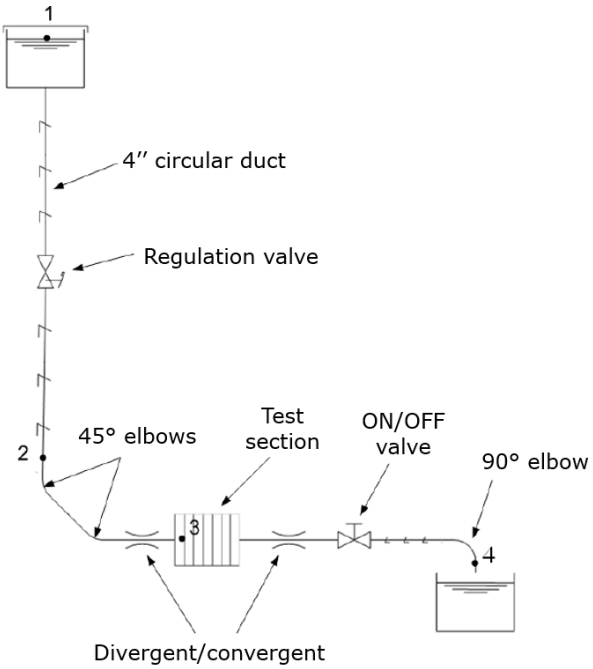

Figure 3.3 Hydraulic loop (Watteaux, 2008).

solution is pumped from bottom tank to upper tank at atmospheric pressure in a parallel derivation (not shown). Because of the glycerin's high viscosity, the flow is generated by gravity. The regulation valve is set at a particular position to define the flow rate. The solution is released via the ON/OFF valve through the test section and back to the bottom tank. The flow rate is determined *a posteriori* with image processing techniques. The top tank was back-lit and filmed during the experiments. The change in glycerin level in the tanks allows to retrieve the flow rate Q in the test section. It is expressed in terms of pitch velocity U:

$$U = \left(\frac{P}{P-D}\right)\frac{Q}{(2L)^2} \tag{3.14}$$

We also define the pitch Reynolds number Re, based on U and cylinder diameter D:

$$Re = \frac{\rho U D}{\mu_l} \tag{3.15}$$

where ρ and μ_l are the fluid density and dynamic viscosity, respectively. In the rest of the article, all the results (experiments, numerical and literature) are presented in terms of pitch Reynolds number Re, and the lift force is non-dimensionalized with the pitch velocity U.

Post-processing method

At the very low Reynolds numbers tested (starting at 10), a Poiseuille flow is established in the test section. The 3D velocity profile in a square duct on Fig. 3.4 was obtained through Taylor expansions of the Navier-Stokes equations, assuming incompressible and parallel flow (Watteaux, 2008). This fact complicates the extraction of the lift coefficients: the 3D velocity

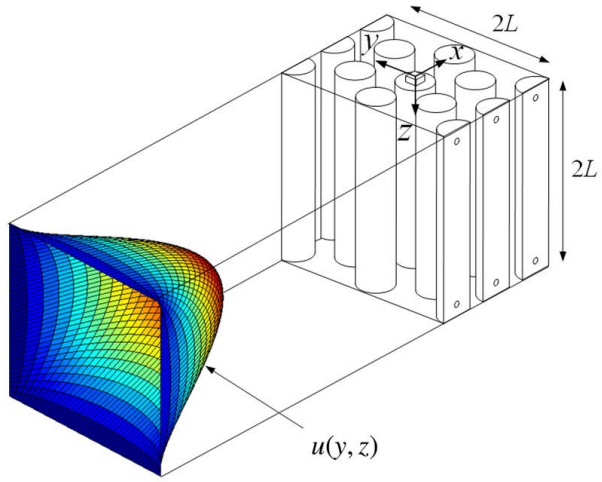

Figure 3.4 Velocity profile upstream to the test section (Watteaux, 2008).

profile induces a local variation of Reynolds numbers along the cylinder and thus local lift coefficients. Experimentally, strain gages were calibrated to measure the total moment of lift induced by the fluid forces along the tube. A more thorough description of experimental setup and techniques, including the extraction of the lift coefficient for low Reynolds numbers and for each position of the cylinder, is given by Charreton *et al.* (2013) and is summarized hereafter.

The experimental moment of lift $M_{L_{exp}}$ was measured. Each experiment corresponds to a flow rate Q, a density ρ and a viscosity μ_l defining an average Reynolds number. The velocity profile of Fig. 3.4 is calculated so that its mean value across the section is equal to $Q/(2L)^2$. The theoretical moment of lift M_L induced by the velocity profile along the cylinder

is expressed as:

$$\begin{aligned} M_{L_{th}} &= \int_{z_g}^{z_g+L_c} M_L(z)\,\mathrm{d}z \\ &= \frac{1}{2}\rho D \int_{z_g}^{z_g+L_c} U_{2D}^2(z) C_L(Re_{2D}) z\,\mathrm{d}z \end{aligned} \tag{3.16}$$

where z_g is the location of the strain gage and L_c is the length of the cylinder. $C_L(Re_{2D})$ are the local lift coefficients along the span of the cylinder. They are based on U_{2D} which is the y-averaged velocity for a given altitude z:

$$U_{2D}(z) = \frac{1}{2L}\int_0^{2L} u(y,z)\,\mathrm{d}y \tag{3.17}$$

C_L is looked under the form of a polynomial function of the Reynolds number for each position of the cylinder. The correlation that best fit experiments is:

$$C_L(Re_{2D}) = A_y + B_y Re_{2D}^{-1/2} + C_y Re_{2D}^{-1/4} \tag{3.18}$$

where $y = Y/D \in \{-8\%, -4\%,\ 0\%,\ 4\%,\ 8\%\}$. Based on Eq. (3.16), one can reconstruct the theoretical moment of lift, as a function of coefficients A_y, B_y and C_y. The least squares method is used to minimize the difference between $M_{L_{th}}$ and $M_{L_{exp}}$ for all the experiments simultaneously. Thus, a linear regression of C_L vs Y/D for a given value of the Reynolds number gives access to $C_{L,y}$. A few intermediate results are given in Annexe A.

At moderate Reynolds number (below 1000), the tube bundle tends to flatten the velocity profile, as attested by Charreton *et al.*'s (2013) 3D numerical computations. Hence, a flat profile was also used to post-process the experimental moments of lift in order to retrieve values of $C_{L,y}$. Indeed, the actual velocity profile is most likely in between a flat and parabolic profile in the range of Re tested.

For high Reynolds numbers $\mathcal{O}(10^4)$, very few experimental values of $C_{L,y}$ can be found in the literature for parallel triangular array with $P/D = 1.5$. As reported in Tab. 3.1, Sawadogo and Mureithi (2014b) measured one value of 5 (equivalent to a value of 0.56 in terms of pitch velocity). However, their array is larger and results were measured on the central cylinder in the 7^{th} row. This means that there are three upstream cylinders. Price and Païdoussis (1984) measured a value of -243 for a different pitch ratio (1.375) for the middle cylinder in the 5^{th} row. In a wind tunnel, Mahon and Meskell (2012) found values ranging from -3.2 to 0.2 for the pitch Reynolds numbers varying between 2×10^4 to 9.8×10^4. There is an obvious scatter in the data. A sensitivity study with numerical computations in Sec. 3.4 highlights

the difficulty to obtain comparable values from one study to the other.

3.3.2 Numerical determination

A pragmatic use of numerical methods is to determine only the force coefficients on the cylinders as the input for quasi-steady analysis for instance. Similar to experiments, the cylinders are statically displaced and the force is measured. This avoids long computation time and casualties inherent to fully coupled fluid-structure interaction simulations involving moving grids.

Direct Numerical Simulation (DNS)

DNS was used by Charreton *et al.* (2013) and Watteaux (2008) to measure $C_{L,y}$ for the exact array of Fig. 3.2 at moderate Reynolds numbers. In the present study, additional 3D simulations are presented in Sec. 3.4.1, along with 2D simulations in Sec. 3.4.3. All simulations were performed on the CADYF in-house code developed at Polytechnique Montreal.

The fluid is considered Newtonian and incompressible. The Navier-Stokes equations are solved with the finite-element method in an implicit manner. The accuracy of the finite-element approximation is directly related to the local mesh size (see Pelletier, 1999). An adaptive remeshing procedure is employed to improve the accuracy, by refining the mesh in regions of high error in the flow variables.

Regions targeted for refinement are identified by the so-called ZZ error estimator by Zhu and Zienkiewicz (1987), which evaluates estimates in elemental error norms. The ZZ error estimator belongs to the family of post-processing techniques (or least-squares-based recovery techniques). Error estimates are obtained by a local least-squares reconstruction of the solution derivatives for the velocity and pressure fields.

Once error estimates are obtained for all dependent variables, an optimal mesh size distribution is determined for each variable using the asymptotic convergence rate of the finite-element method and the principle of equidistribution of the error so that each element has the same contribution to the norm of the total error (Pelletier, 1999). The minimum element size predicted for all flow and sensitivity variables is selected to generate a new mesh by an advancing front method. This is performed in an iterative fashion, beginning with a coarse mesh and producing a sequence of meshes which reduce the error by a constant factor over that of the previous mesh. The minimum element size predicted by all the dependent variables is selected on a given element. The computational domain is then re-meshed using an advancing front technique.

To compute the stability derivative, 5 cycles of adaptive meshing is used starting with an

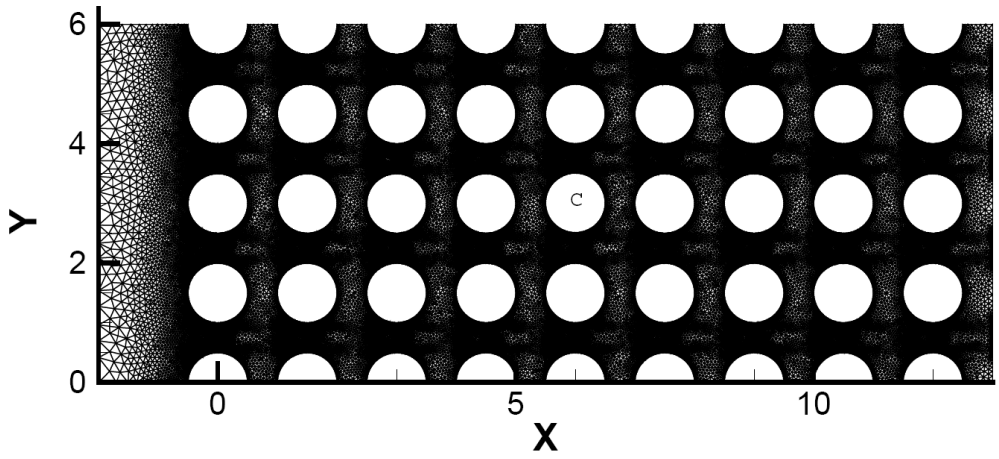

Figure 3.5 Final mesh for normal square array, $P/D = 1.5$, $Re = 80$. Number of nodes is 284 638.

initial mesh of typically 3000 nodes and a final mesh of approximately 300 000 nodes. For each case, two calculations are performed with the unperturbed tube bundle and one with the central cylinder displaced by 1%D. The final mesh and streamlines with the displaced central cylinder are shown in Fig. 3.5, 3.6, 3.7 and 3.8. The force coefficient obtained at fourth and fifth cycles have the same first three digits.

In the next section, results using this method will be labeled as "DNS".

Potential flow

An inviscid flow model was also employed for the same purposes. It relies on a complex number formulation to describe the velocity potential. Singularities are placed at the center of the tubes to prescribe the non-penetration condition. This approach is summarized in Étienne (1999) and was recently used by Senez and Étienne (2011). The potential, at location Z in the complex plane, is expressed by Laurent series as follows:

$$F(Z) = U_\infty Z + \sum_{j=1}^{N_c} \sum_{n=1}^{\infty} a_{jn} \left[\frac{Rc_j}{Z - C_j} \right]^n \tag{3.19}$$

where N_c is the number of cylinders in the flow, Rc_j is the radius of the cylinder j, C_j is the complex coordinate of the center of the cylinder j. $U_\infty Z$ is the complex potential of the flow without the cylinders. U_∞ is the velocity of the flow at infinity. In the vicinity of cylinder i,

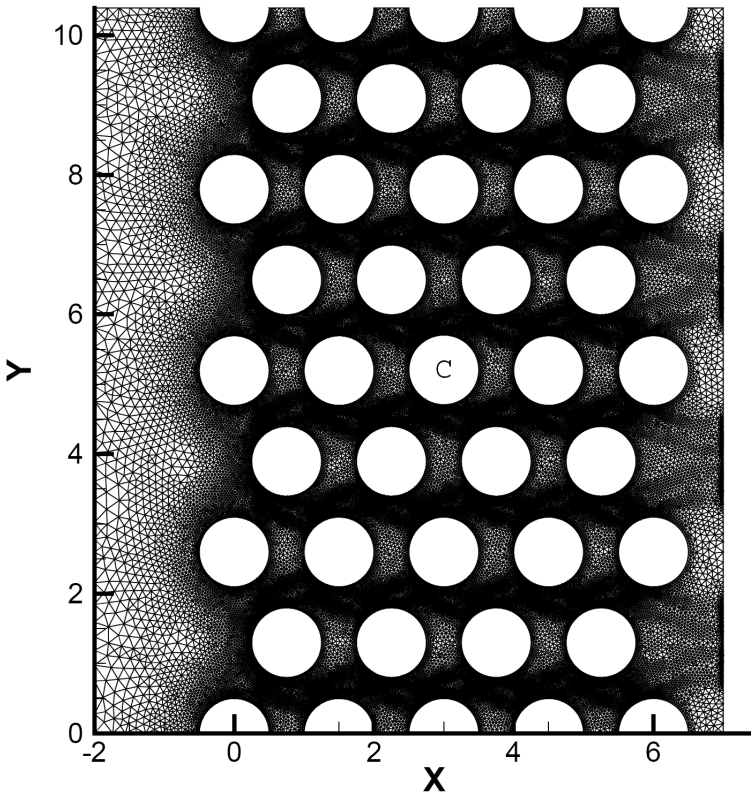

Figure 3.6 Final mesh for parallel triangular array, $P/D = 1.5$, $Re = 80$. Number of nodes is 306 057.

Eq. (3.19) can be re-written using the negative binomial theorem as:

$$F(Z) = U_\infty Z + \sum_{n=1}^{\infty} a_{in} \left[\frac{Rc_i}{Z - C_i}\right]^n + \sum_{p=0}^{\infty} \alpha_{ip} \left[\frac{Z - C_i}{Rc_i}\right]^p \tag{3.20}$$

where α_{ip} is the binomial coefficient, and a_{jn} are obtained from the non-penetration condition. Limiting the number of singularity up to N, the non-penetration condition leads to a linear system. It is solved in order to determine the complex potential. Finally, the lift force is calculated via the pressure integration ($\nabla F(Z)^2$) around the central cylinder, deduced from the Bernouilli equation. A convergence study on the number of singularity N was performed to ensure good numerical accuracy of $C_{L,y}$. All the viscous effects are neglected with the potential flow hypothesis. Therefore, results correspond to the condition at infinite Reynolds number. The advantage of the potential flow model is that the computation cost is very low. Hence, it is a cost-effective model to examine the effect of geometric parameters. Results will be referred to as "potential flow".

Unfortunately, very few values of $C_{L,y}$ based on numerical codes can be found in the

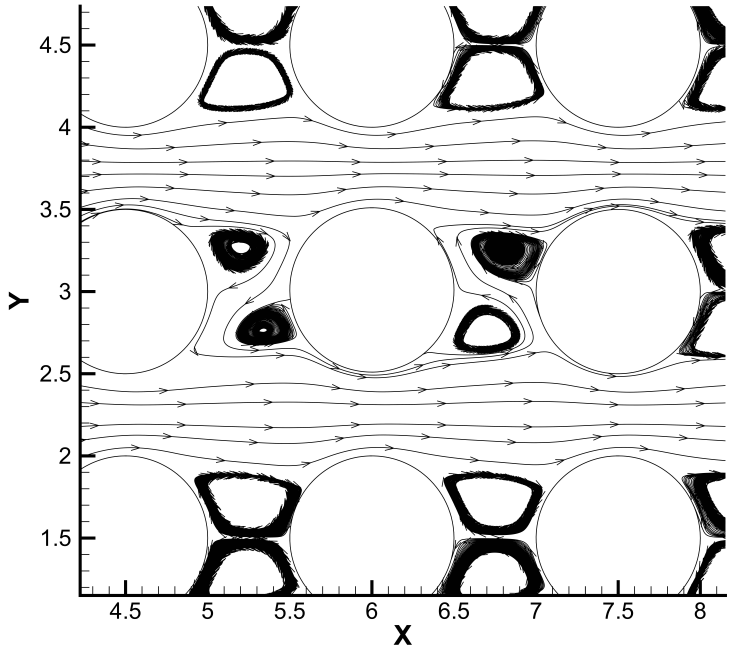

Figure 3.7 Streamlines (DNS) for normal square array, $P/D = 1.5$, $Re = 80$. Central tube was displaced by $1\%D$ upward.

literature, for parallel triangular arrays. Many researchers attempted to predict instability directly, or extracted the unsteady force coefficients in order to perform unsteady analysis. Very few extracted the steady force coefficient for quasi-steady analysis. We can mention the work of Gillen and Meskell (2009) in which a RANS simulation is used to find the steady force coefficients for a normal triangular array. However, the values found with potential hypothesis in the present study, for the same array, compare better with Mahon and Meskell's (2009) experiments than Gillen and Meskell's Gillen and Meskell (2009) RANS simulations (see Sec. 3.4). This contributes to the attractiveness of inviscid flow models to compute $C_{L,y}$, as computation times are much smaller. Note that potential flow theory is also able to predict very accurately the added mass (Plagnard *et al.*, 2014).

3.4 Parametric study of the lift coefficient derivative

3.4.1 Effect of Reynolds number (experiments and simulations)

We investigate the effect of Reynolds number on the lift coefficient derivative. Results by Charreton *et al.* (2013) are shown on Fig. 3.9 at moderate values of the Reynolds number. Note that Re_{2D} is the pitch Reynolds number based on the y-averaged velocity for a given altitude z. This allows to take into account the effect of a Poiseuille flow generating local lift

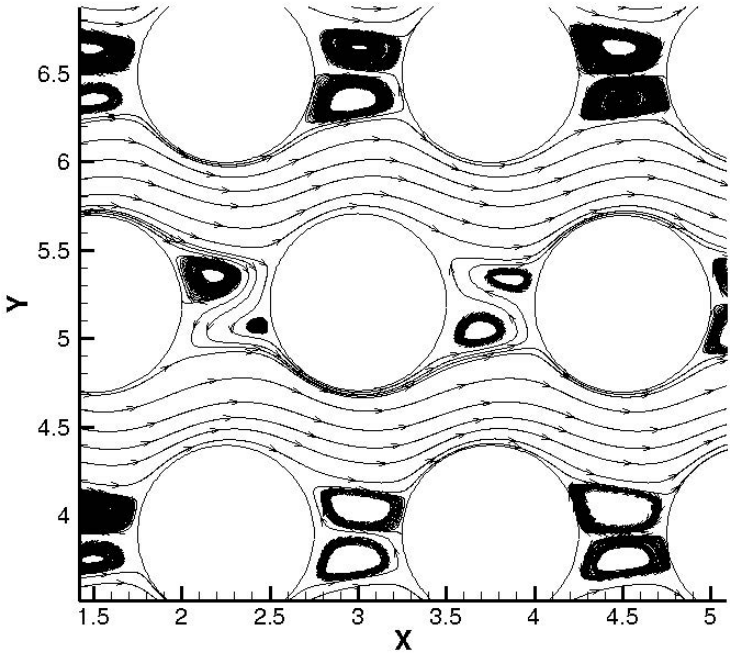

Figure 3.8 Streamlines (DNS) for parallel triangular array, $P/D = 1.5$, $Re = 80$. Central tube was displaced by $1\%D$ upward.

coefficients along the cylinder in the z-direction, discussed in Sec. 3.3.1.

Experimentally, $C_{L,y}$ seems to diverge towards $-\infty$ for low Reynolds numbers. Then as Re_{2D} is increased, so does $C_{L,y}$, which seems to converge towards an asymptote. A change of sign occurs around $Re_{2D} = 200$ for experimental values. A critical value for which $C_{L,y} = 0$ was found. The consequences of this result regarding the stability of a single flexible tube will be discussed in Sec. 3.5.

Numerical results obtained with 2D DNS are in very good agreement with experiments up to $Re_{2D} = 150$. After this point, $C_{L,y}$ suddenly decreases, and never turns positive in the range of velocities tested. The main reason was that three-dimensional effects cannot be neglected at this regime. Then, 3D DNS simulations were performed. Details on the procedure are given by Charreton *et al.* (2013). Results are presented here and were calculated with a flat inlet profile. As we can see, the trend is better respected than that obtained with 2D simulations. However, the in-house finite-element code CADYF that was used to perform the simulations does not allow to perform 3D DNS past $Re = 400$. Therefore, the change in sign of $C_{L,y}$ could not be observed. A possible cause for this limitation is that the flow may become turbulent locally. Without the consideration of any turbulent model nor any stabilization, the DNS is not able to converge.

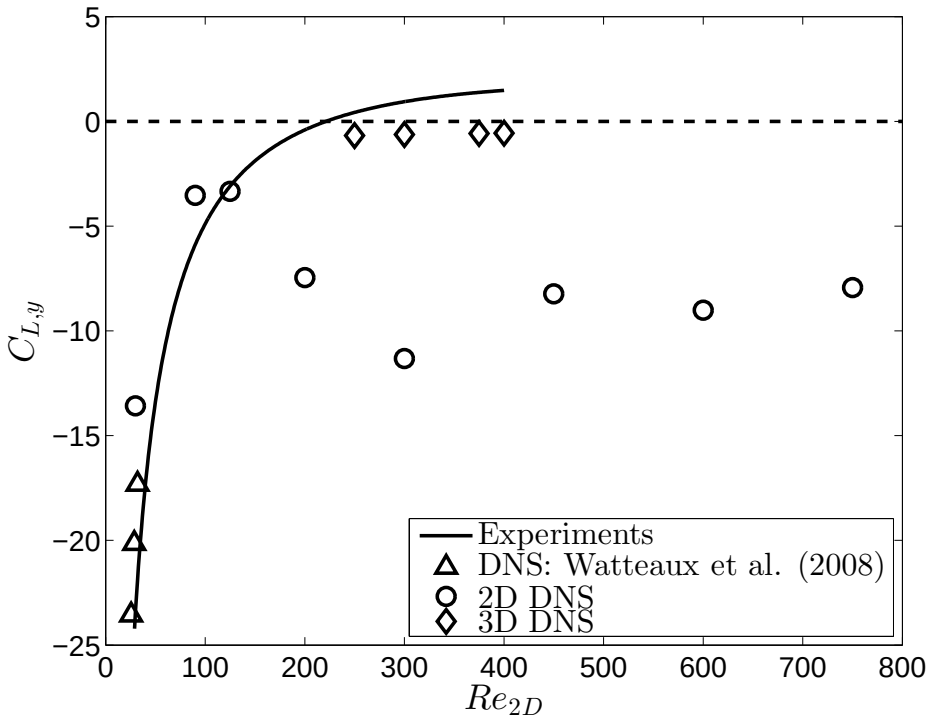

Figure 3.9 Influence of Reynolds number on $C_{L,y}$ at moderate Reynolds.

3.4.2 Effect of the angle of the configuration

Although four bundle configurations are commonly studied (normal square, rotated square, normal triangular and parallel triangular), it is interesting to test the angle of the configuration. Sensitivity of force coefficients on the regularity of the array is a useful piece of information. Similar experiments were performed by Yeung and Weaver (1983) who could vary the angle of incidence of the flow by rotating the array. They found a jump in FEI thresholds when going from a normal triangular array to a parallel triangular.

First, the potential flow model is employed to examine the effect of the angle of the configuration on $C_{L,y}$. We use a different approach from the experiments of Yeung and Weaver (1983). Instead of changing the angle of incidence of the flow, we deform the angle of the array. The angle of the bundle α is defined in Fig. 3.10. Changing α allows going from one configuration to the other in a continuous manner.

To ensure the regularity of the array, the following conditions should be respected:

$$\begin{cases} T1 = \max(P, 2P\sin\alpha) \\ T2 = \max(P, P\sqrt{2-2\sin\alpha}) \end{cases} \tag{3.21}$$

The center tube of a large array of 85 tubes (7 rows and 13 columns) is considered. It

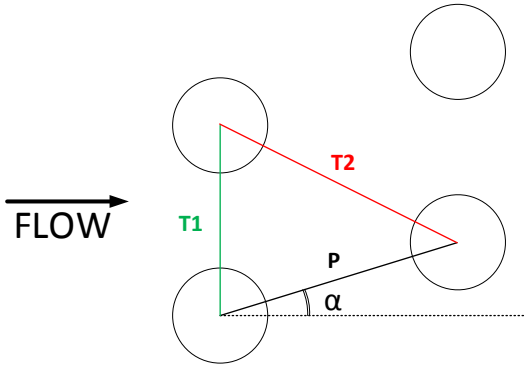

Figure 3.10 Definition of the angle of the tube bundle configuration.

is displaced by $1\%D$ in the y direction to measure $C_{L,y}$. The linearity of the lift coefficient in the range $[-8\%D,\ +8\%D]$ was verified. Fig. 3.11 shows the streamlines and the pressure distribution around the cylinder. Note on Fig. 3.11(c) that the rotated square is the only configuration for which $C_{L,y} < 0$. Indeed, the confinement in the y direction is minimal compared to the other configurations. The flow below the displaced cylinder is almost unaffected. This results in higher pressure below the cylinder and thus a resultant force upward in the y direction.

Results of the $C_{L,y}$ by continuously varying the angle α are shown on Fig. 3.12. The discontinuity at $\alpha = 30°$ is explained by Eq. (3.21). In the triangle of Fig. 3.10, at least two of the sides should have a length equal to P to ensure the regularity of the array. The angle for which T1 becomes larger than P and T2 is blocked at a length of P is exactly $\alpha = 30°$.

Depending on the bundle, $C_{L,y}$ can be either positive (static instability may occur) or negative (damping controlled instability may occur). For $\alpha = 60°$ (parallel triangular array), the sensitivity is very high, and $C_{L,y}$ can even turn negative within a few degrees. This is consistent with the work of Khalifa *et al.* (2012) who observed that very small irregularities in the array had major effects on stability. Still, the value of 0.13 for the parallel triangular array is reasonably close to the value of 0.56 measured by Sawadogo and Mureithi (2014b) (they actually measured a value of 5 based on the freestream velocity) at $Re = 8.4 \times 10^4$. It supports the asymptotic trend of $C_{L,y}$.

3.4.3 Effect of pitch ratio

Fig. 3.13 shows the influence of pitch ratio for all the tube bundle angles tested. Ratios of 1.2, 1.375, 1.5 and 1.58 were tested since these values can be commonly found in the literature and are representative of real configurations in tube bundles of steam generators. The potential flow theory does not predict a strong effect of pitch ratio on $C_{L,y}$. Indeed, the

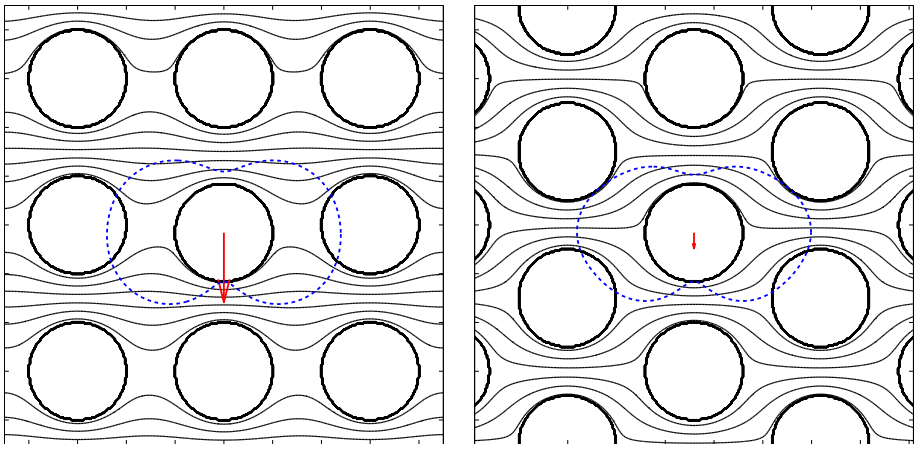

(a) Normal square ($\alpha = 0°$). (b) Normal triangular ($\alpha = 30°$).

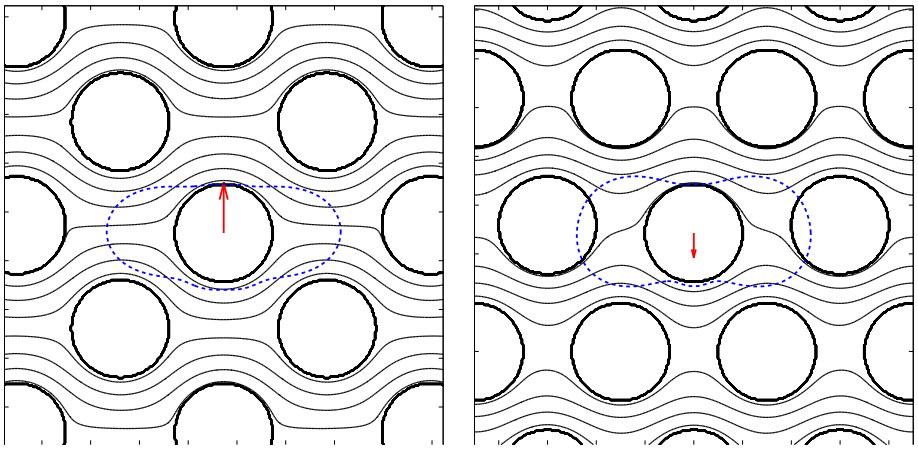

(c) Rotated square ($\alpha = 45°$). (d) Parallel triangular ($\alpha = 60°$).

Figure 3.11 Potential flow streamlines and pressure distribution (−−) around the central cylinder for the four typical configurations. Central tube was displaced by 8%D downward while the fluid flows from left to right. The red arrow depicts the resultant lift force.

lift force was non-dimensionalized with the pitch velocity. For the same reason, the freestream velocity U_∞ does not have any effect.

Previous results emphasize the effects of Reynolds number, angle and pitch ratio. Same results were obtained with DNS, summarized by Fig. 3.14. These simulations were performed in arrays of 9 columns and 5 rows, with an inlet flat profile. Symmetry conditions were applied between half-tube, up and down on the calculation domain of Fig. 3.5. Reynolds numbers tested vary from 20 to 80. Therefore, 2D DNS was employed, as we showed that three-dimensional effects appear at around $Re = 150$.

It appears that $C_{L,y}$ increases its magnitude dramatically when the pitch ratio decreases. Indeed, a closely packed array is more likely to affect the fluid, and therefore the force on

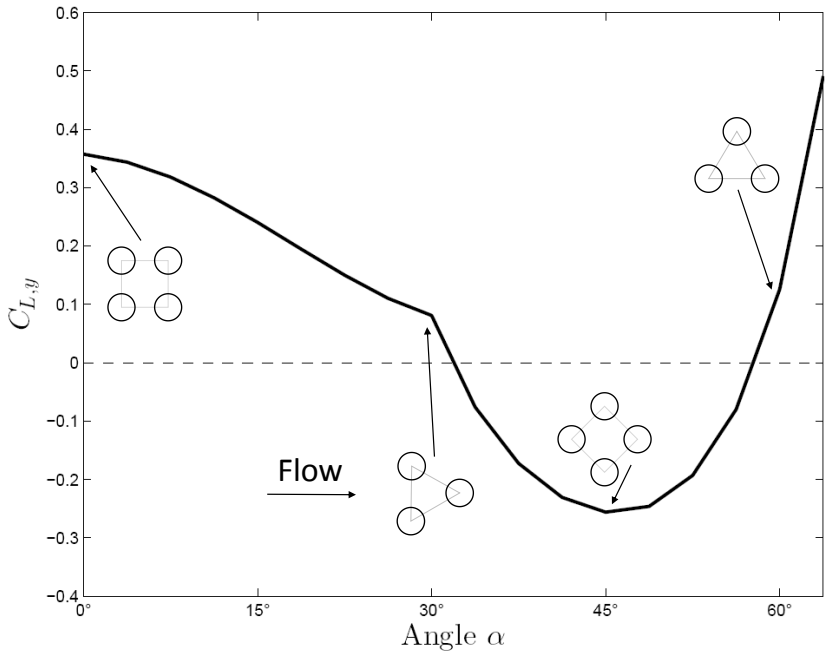

Figure 3.12 Effect of the angle of the bundle on the lift coefficient derivative predicted by potential flow, for $P/D = 1.5$.

a tube. This explains why sensitivity with respect to the tube displacement is much more important for packed arrays.

As expected in this range of Reynolds number (below 80), $C_{L,y}$ is negative and growing with Re. Besides the shift point at $\alpha = 30°$, the trend with respect to the configuration angle is similar to that obtained with the potential theory. Approaching the critical Reynolds number, the curve seems to flatten towards zero. This suggests that $C_{L,y}$ crossing zero might also occur in the three other arrays. Although $C_{L,y} = 0$ was verified experimentally for a parallel triangular array, the critical Reynolds number value could be similar for each angle. Further work is needed to clarify this point, as the study is complicated by 3D effects at high regime.

3.4.4 Comparison with the literature

Values reported in the literature were presented in Tab. 3.1 and are compared to the present results. There is a considerable amount of scatter in the data. For instance, despite the differences in pitch ratio and tube location, studies report completely opposite values. On the other hand, Mahon and Meskell's (2009) results are particularly close to potential results for normal triangular array. In both studies, $C_{L,y}$ decreases with increasing pitch ratio, while staying positive.

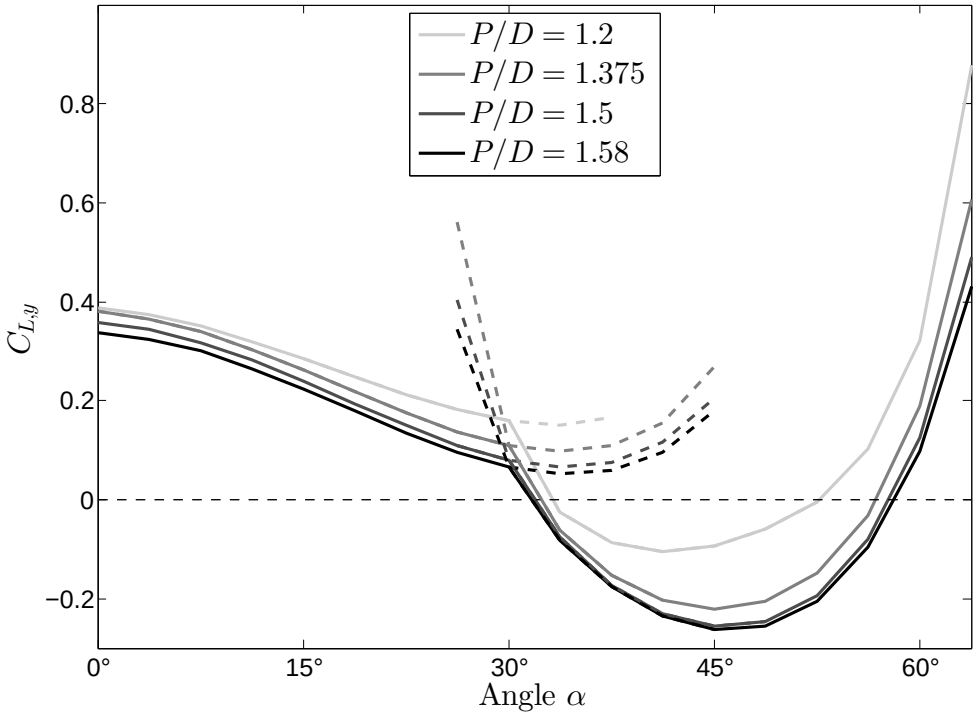

Figure 3.13 Effect of pitch ratio on the lift coefficient derivative predicted by potential flow. −−: Effect of breaking the regularity of the array (α is continuously varied regardless of Eq. (3.21).

It should be emphasized that measurements in air lead to fairly high uncertainty compared to water as the relative magnitude of the force is much smaller. Averaging the noise or using other techniques (*e.g.* pseudo-modal decomposition for bi-stable flow in Mahon and Meskell (2012)) can lead to different results. Then again, measurement technique can have an impact. In our case, the cantilevered instrumented tube is subjected to vortex shedding as we try to measure the steady force. Thus, the force signal is averaged over time. On the other hand, a pressure measurement over the circumference of a stiff tube is less invasive as it does not influence the flow. However, it does not allow to measure the viscous drag.

Furthermore, the attractiveness of the quasi-steady model stems in its linearity. Thus, it only requires a first-order derivative of the lift coefficient. Although this linearity was verified by Charreton *et al.* (2013) at low Reynolds numbers, several studies showed a non-linear trend (*e.g.* Païdoussis *et al.*, 1993; Sawadogo and Mureithi, 2014a). The lift gradient tends to decrease past 1 or 2%D. Note that this non-linear behavior was taken into account by Sawadogo *et al.* (2014). Similarly, Meskell and Fitzpatrick (2003) present a model based on non-linear curve fitting techniques of fluidelastic forces. In both cases (among other similar

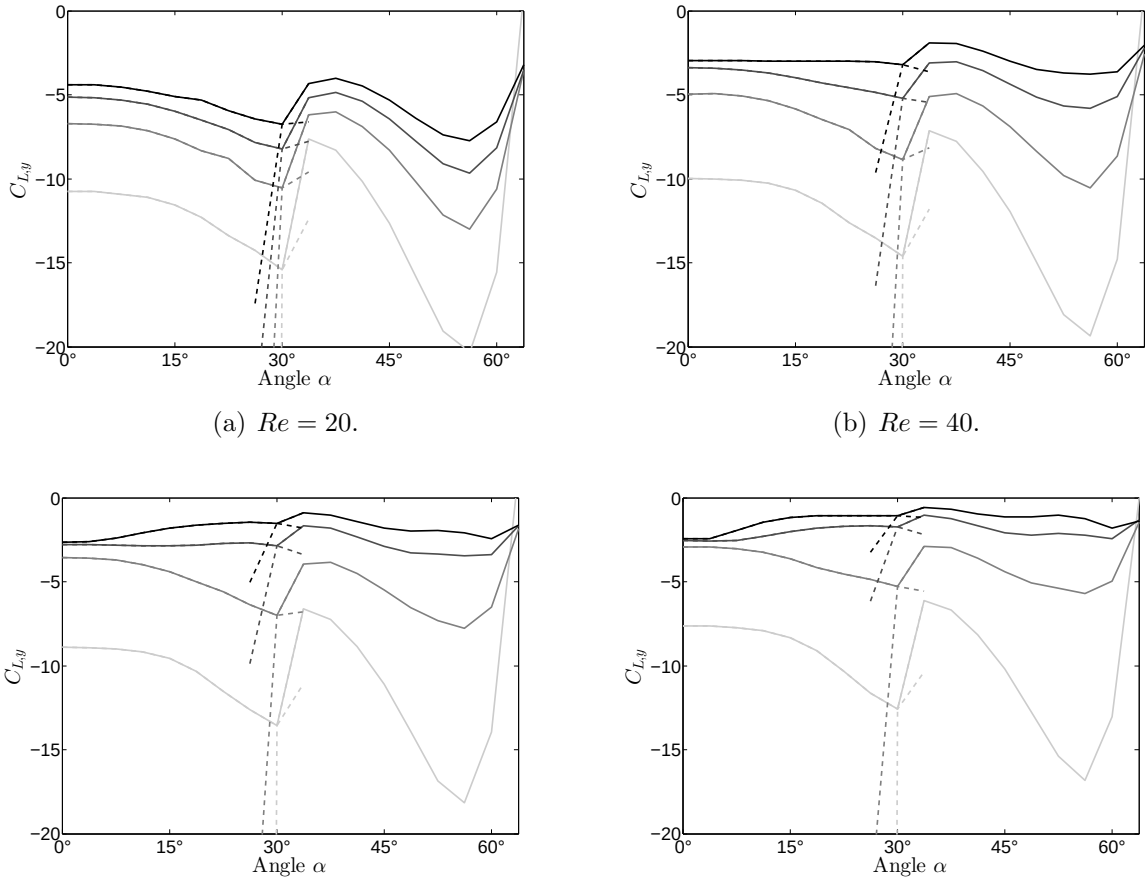

(a) $Re = 20$. (b) $Re = 40$.

(c) $Re = 60$. (d) $Re = 80$.

Figure 3.14 Influence of Reynolds number, pitch ratio and angle of the configuration obtained with 2D DNS. Legend is the same as that of Fig. 3.13: $P/D = 1.2$, 1.375, 1.5, 1.58 from the lightest to the darkest line.

studies), the agreement is significantly improved. Notably, the reduction of the lift coefficient derivative at high amplitude leads to limit cycle regimes of the tube displacement. These models are however more complicated than the quasi-steady model.

3.5 Stability of a single tube with the quasi-steady model

Besides the time delay which was found to be $\mu \sim \mathcal{O}(1)$ for single-phase flow and the lift coefficient derivative, the quasi-steady model also needs values for the steady drag C_{D_0} on the cylinder. It was measured experimentally using the same technique that presented in Sec. 3.3.1 for $C_{L,y}$. It was also verified that $\partial C_D/\partial y = 0$, therefore it was estimated only for the central position of the tube. Fig. 3.15(a) shows the reconstructed non-dimensional moment using Eq. (3.16) and Fig. 3.15(b) shows the extracted drag coefficient. Note that the

post-processing correlation also takes into account the Poiseuille profile along the cylinder.

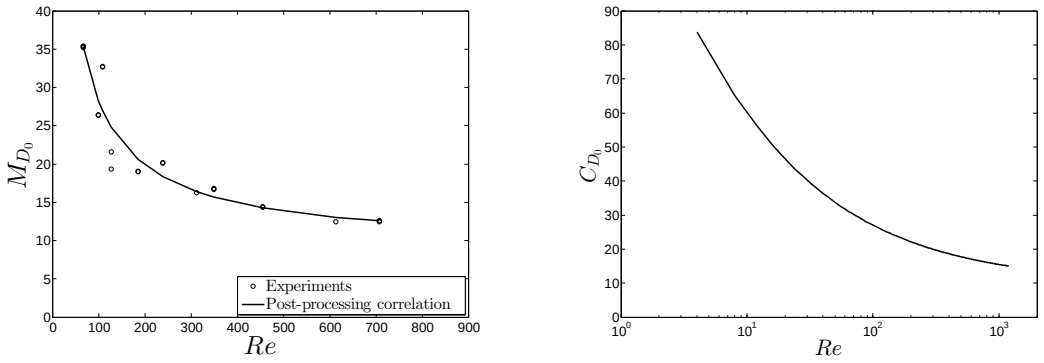

(a) Adimensional moment. (b) Steady drag coefficient.

Figure 3.15 Experimental results of the drag measurement for the central cylinder.

As expected, C_{D_0} decreases with the Reynolds Number. Because a trend stand out for both $C_{L,y}$ and C_{D_0}, we propose an interpolation between our measured values for C_{D_0} and $C_{L,y}$ and that of Sawadogo and Mureithi (2014b), since trends stand out in both cases. Indeed, the values they found seem more reasonable compared to other studies cited in 3.1. Furthermore, the value of 1.2 for $C_{L,y}$ found by potential theory in 3.12 seems to confirm the trend, as mentioned earlier. Fig. 3.16 shows the results. Based on these correlations,

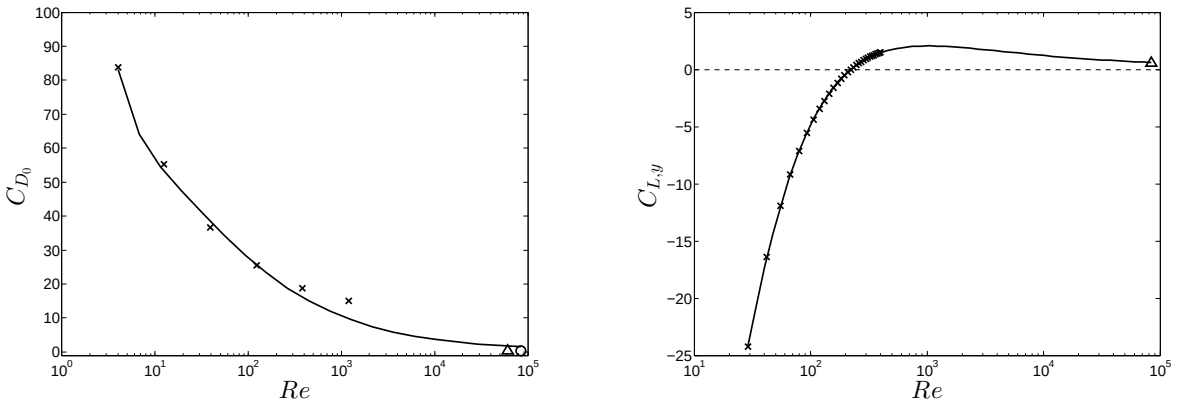

(a) Steady drag coefficient. (b) Lift coefficient derivative.

Figure 3.16 Reynolds number-wise interpolation of C_{D_0} and $C_{L,y}$. Legend: $\times$: present experiments; $\triangle$: Shahriary *et al.* (2007), $\circ$: Sawadogo and Mureithi (2014b), $-$: fitting

the effect of Reynolds number on the stability of a tube using the quasi-steady model (cf. Fig. 3.17) was investigated. Using the quasi-steady model requires to solve the so-called transcendental Eq. (3.10).

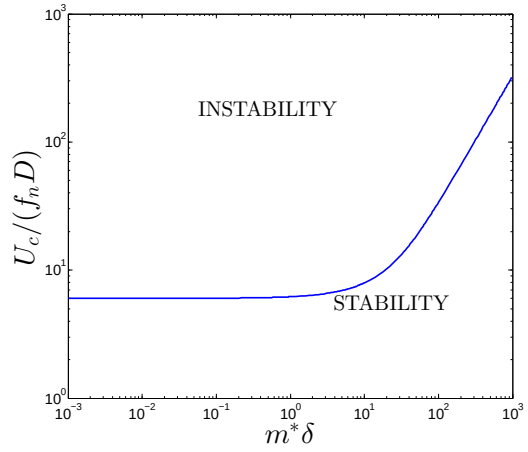

(a) $Re = 10$.

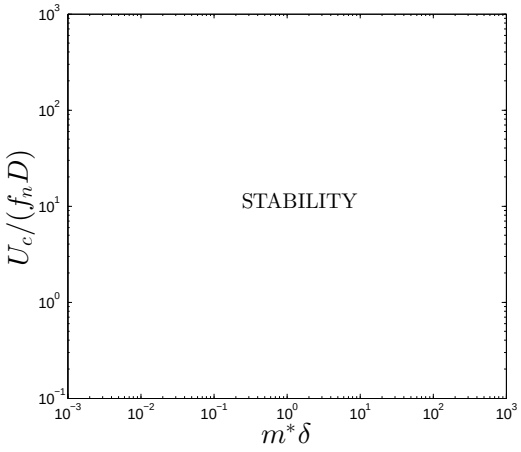

(b) $Re = Re_c(\approx 210)$.

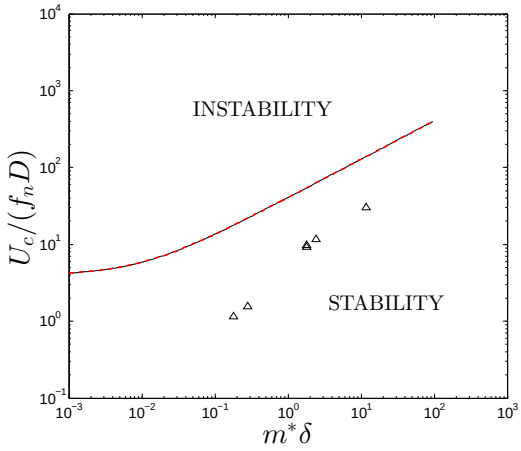

(c) $Re = 10^4(\approx \infty)$

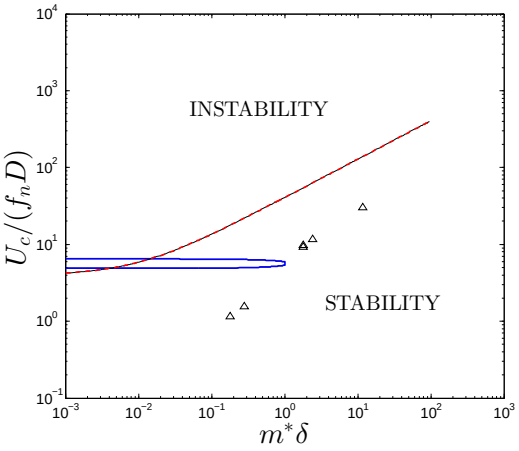

(d) $Re = 10^4(\approx \infty)$, with $\mu = 4$.

Figure 3.17 Influence of the Reynolds number on the stability of a single flexible tube in a parallel triangular array with $P/D = 1.5$, $\mu = 1$ and $\delta = 0.01$. ⎯: Damping-controlled instability boundary; - -: Stiffness-controlled (static divergence) instability boundary; △: Single-flexible tube experiments for P/D from 1.375 to 1.73 (Lever and Weaver, 1986b; Weaver and Grover, 1978; Austermann and Popp, 1995; Scott, 1987; Little, 2003).

Damping-controlled instability can occur when the condition $|C_{L,y}| > C_{D_0}$ is met. Fig. 3.17(a) shows that it can occur at very low values of the Reynolds number. Rapidly, as can be seen on Fig. 3.16, $|C_{L,y}|$ becomes smaller than C_{D_0} so the stability boundary diverges and damping controlled instability cannot exist anymore.

Note on Eq. (3.10) that because of the presence of U in the sine function, sub-harmonic regions of instability may occur. These subregions have been addressed by Païdoussis *et al.* (1996) who highlighted the difficulty to obtain them experimentally. They are thus non-

existent from a practical point-of-view.

For the critical Reynolds number Re_c, the fact that $C_{L,y}$ becomes equal to 0 only implies that instability is independent of the time delay for the corresponding Reynolds number, even though it is unconditionally stable as attested by Fig. 3.17(b). Very little attention has been given to the static instability since cylinders are in most cases subject to oscillatory motion due to the fluid. Therefore, it has rarely been observed (Païdoussis *et al.*, 1989).

The prediction of the model for high Reynolds numbers is contradictory with Khalifa *et al.*'s (2012) experiments who reported instability by negative damping, as well as several other studies for various pitch ratios. On the logarithmic scale, the trend established by these experiments is a straight line of coefficient 1, which is typical of the damping-controlled mechanism (it is 1/2 for stiffness-controlled instability). However, the curve of Fig. 3.17(c) was obtained with a time delay parameter $\mu = 1$. Note on Fig. 3.17(d) that using a time delay parameter of 4, a subregion of instability by negative damping can be obtained. Still, this does not explain the discrepancy between the model and experiments. It shows that FEI is highly dependent on this time delay parameter which can reach 2.7 in two-phase flow, as measured by Sawadogo and Mureithi (2014a).

Nevertheless, the reader should remember that the dynamic instability controlled by stiffness (wake-flutter mechanism, not to be confused with static divergence instability) would be predominant at high Re and $m\delta/\rho D^2$ for fully flexible arrays.

It should also be emphasized that $C_{L,y}$ crossing zero has also been observed by Mahon and Meskell (2012) at high Reynolds for $P/D = 1.375$, and in two-phase flow by Sawadogo and Mureithi (2014b) at around 5% void fraction. They addressed this point, emphasizing that FEI has been observed at this point experimentally. The delay mechanism mode with a simple time delay fails to predict FEI in this case.

3.6 Conclusion

This work summarizes our investigation of the effect of the Reynolds number on the force coefficients on a single flexible tube in tube bundles. It was steered towards the study of the lift coefficient derivative in the transverse (lift) direction. The existence of FEI relies on this parameter. Based on experimental results in two different loops, a trend for $C_{L,y}$ with respect to the Reynolds number was established for a parallel triangular array with $P/D = 1.5$. It is negative for low Re, reaches an asymptote for higher values and crosses zero around $Re = 200$. DNS and potential codes were used in parallel to confirm this trend. The DNS showed that 2D simulations do not stand the comparison with experiments for values of the pitch Reynolds number higher than 150. Therefore, 3D simulations are necessary to

capture the effects responsible for the lift force along a cylinder. The codes were also used to perform a sensitivity analysis on geometric parameters of the array, such as bundle angle and pitch ratio. It was found that $C_{L,y}$ is highly sensitive to those parameters. This gives some perspective on the scattered data found in the literature. Because of confinement, the pitch-to-diameter ratio has a major effect on the lift coefficient derivative, for moderate Reynolds number (below 100). This behavior is attributed to the appearance of vortices in the lee of the cylinders which is highly dependent on confinement. On the other hand, the potential flow theory does not predict a strong dependence on pitch ratio.

Based on the experimental data for a parallel triangular array with $P/D = 1.5$, the stability of a single flexible tube was analyzed with the quasi-steady model. FEI can theoretically occur at very low Re but the cylinder becomes quickly unconditionally stable (with respect to damping controlled instability). This does not match experimental evidence of other studies. These experimental studies aimed at determining the fluidelastic instability threshold for a single flexible tube, and report damping-controlled FEI for high Reynolds numbers. The quasi-steady model fails to predict damping-controlled instability for high values of the Reynolds number. On the other hand, static divergence instability may be possible, provided that the tube is not subject to an oscillatory motion.

The present study raises questions about the applicability of the quasi-steady model. For similar arrays, some studies report completely different results for the lift coefficient derivative. Therefore, it is still not perfectly clear as to what values should be used. The idea of a non-linear time delay is also something that could be investigated for further improvement of the quasi-steady model. Lastly, note that the time delay is only applied to the position-dependent term of the fluid force on the cylinder. Different time delays could also be applied to velocity and acceleration-dependent terms.

Acknowledgments

This work was sponsored by the Natural Sciences and Engineering Research Council, Babcock & Wilcox Canada and Atomic Energy of Canada Ltd., through the BWC/AECL/NSERC research chair in fluid-structure interactions.

References

AU-YANG, M. K., CHEN, S. S., PAÏDOUSSIS, M. P., PETTIGREW, M. J., WEAVER, D. S. and ZIADA, S. (2000). Flow-induced vibrations in power and process plant components - progress and prospects. *Journal of Pressure Vessel Technology*, 122, 339–348.

AUSTERMANN, R. and POPP, K. (1995). Stability behaviour of a single flexible cylinder in rigid tube arrays of different geometry subjected to cross-flow. *Journal of Fluids and Structures*, 9, 303–322.

CHARRETON, C., BÉGUIN, C., YU, R. and ETIENNE, S. (2013). Stability derivatives in a parallel triangular tube bundle subject to cross-flow at moderated reynolds number. *ASME 2013 Pressure Vessels and Piping Conference*. American Society of Mechanical Engineers.

CHEN, S. S. (1983). Instability mechanisms and stability criteria of a group of circular cylinders subjected to cross-flow. Part i : theory. *Journal of Vibration, Acoustics, Stress, and Reliability in Design*, 105, 463–518.

CHEN, S. S. and SRIKANTIAH, G. S. (2001). Motion-dependent fluid force coefficients for tube arrays in crossflow. *Journal of pressure vessel technology*, 123, 429–436.

CONNORS, H. J. (1970). Fluidelastic vibration of tube arrays excited by cross flow. *Flow induced vibration in Heat Exchangers*. New York : ASME, 42–56.

ÉTIENNE, S. (1999). *Contribution à la Modélisation de l'Écoulement de Fluide Visqueux Autour de Faisceaux de Cylindres Circulaires*. PhD thesis, École Supérieure de Mécanique de Marseille.

ÉTIENNE, S. and PELLETIER, D. (2011). Tube arrays flow-induced vibrations simulations with ale finite element method. *ASME 2011 Pressure Vessels and Piping Conference*. American Society of Mechanical Engineers, 329–336.

GILLEN, S. and MESKELL, C. (2009). Numerical analysis of fluidelastic instability in a normal triangular tube array. *ASME 2009 Pressure Vessels and Piping Conference*. American Society of Mechanical Engineers, 447–455.

GRANGER, S. and PAÏDOUSSIS, M. P. (1996). An improvement to the quasi-steady model with application to cross-flow-induced vibration of tube arrays. *Journal of Fluid Mechanics*, 320, 163–184.

KHALIFA, A., WEAVER, D. S. and ZIADA, S. (2012). A single flexible tube in a rigid array as a model for fluidelastic instability in tube bundles. *Journal of Fluids and Structures*, 34, 14–32.

LEVER, J. H. and WEAVER, D. S. (1982). A theoretical model for fluid-elastic instability in heat exchanger tube bundles. *Journal of Pressure Vessel Technology*, 104, 147–158.

LEVER, J. H. and WEAVER, D. S. (1986a). On the stability of heat exchanger tube bundles, part i: Modified theoretical model. *Journal of Sound and Vibration*, 107, 375–392.

LEVER, J. H. and WEAVER, D. S. (1986b). On the stability of heat exchanger tube bundles, part ii: Numerical results and comparison with experiments. *Journal of Sound and vibration*, 107, 393–410.

LITTLE, J. (2003). *The Effect of Damping on Fluidelastic Instability in Heat Exchanger Tube Array*. Master's thesis, McMaster University, Hamilton, Ontario, Canada.

MAHON, J. and MESKELL, C. (2009). Investigation of the underlying cause of the interaction between acoustic resonance and fluidelastic instability in normal triangular tube arrays. *Journal of Sound and Vibration*, 324, 91–106.

MAHON, J. and MESKELL, C. (2012). Surface pressure survey in a parallel triangular tube array. *Journal of Fluids and Structures*, 34, 123–137.

MESKELL, C. and FITZPATRICK, J. A. (2003). Investigation of the nonlinear behaviour of damping controlled fluidelastic instability in a normal triangular tube array. *Journal of Fluids and Structures*, 18, 573–593.

PAÏDOUSSIS, M. P. (2006). Real-life experiences with flow-induced vibration. *Journal of Fluids and Structures*, 22, 741 – 755.

PAÏDOUSSIS, M. P., MAVRIPLIS, D. and PRICE, S. J. (1984). A potential-flow theory for the dynamics of cylinder arrays in cross-flow. *Journal of Fluid Mechanics*, 146, 227–252.

PAÏDOUSSIS, M. P., PRICE, S. J. and DE LANGRE, E. (2011). *Fluid-structure interactions : cross-flow induced instabilities*. Cambridge University Press, Cambridge.

PAÏDOUSSIS, M. P., PRICE, S. J. and MUREITHI, N. W. (1993). Nonlinear and chaotic dynamics of a two-degree-of-freedom analytical model for a rotated triangular array in cross-flow. *Journal of fluids and structures*, 7, 497–520.

PAÏDOUSSIS, M. P., PRICE, S. J. and MUREITHI, N. W. (1996). On the virtual nonexistence of multiple instability regions for some heat-exchanger arrays in crossflow. *Journal of fluids engineering*, 118, 103–109.

PAÏDOUSSIS, M. P., PRICE, S. J., NAKAMURA, T., MARK, B. and MUREITHI, N. W. (1989). Flow-induced vibrations and instabilities in a rotated-square cylinder array in cross-flow. *Journal of Fluids and Structures*, 3, 229–254.

PELLETIER, D. (1999). Adaptive finite element computations of complex flows. *Int. J. Numer. Meth. Fluids*, 31, 189–202.

PETTIGREW, M. J. and TAYLOR, C. E. (1991). Fluidelastic instability of heat exchanger tube bundles; review and design recommendations. *Journal of Pressure Vessel Technology*, 113, 242–256.

PETTIGREW, M. J., TAYLOR, C. E., JANZEN, V. P. and WHAN, T. (2002). Vibration behavior of rotated triangular tube bundles in two-phase cross flows. *Journal of pressure vessel technology*, 124, 144–153.

PETTIGREW, M. J., TAYLOR, C. E. and KIM, B. S. (1989). Vibration of tube bundles in two-phase cross-flow: Part 1—hydrodynamic mass and damping. *Journal of Pressure Vessel Technology*, 111, 466–477.

PLAGNARD, T., BÉGUIN, C. and ÉTIENNE, S. (2014). Predicting fluidelastic instability in tube array with potential theory. *ASME 2014 Pressure Vessels and Piping Conference*. American Society of Mechanical Engineers.

PRICE, S. J. (1995). A review of theoretical models for fluidelastic instability of cylinder arrays in cross-flow. *Journal of Fluids and Structures*, 9, 463–518.

PRICE, S. J. (2001). An investigation on the use of connors' equation to predict fluidelastic instability in cylinder arrays. *Journal of pressure vessel technology*, 123, 448–453.

PRICE, S. J. and PAÏDOUSSIS, M. P. (1984). An improved mathematical model for the stability of cylinder rows subject to cross-flow. *Journal of Sound and Vibrations*, 97, 615–640.

PRICE, S. J. and PAÏDOUSSIS, M. P. (1986). A single-flexible-cylinder analysis for the fluidelastic instability of an array of flexible cylinders in cross-flow. *Journal of fluids engineering*, 108, 193–199.

SAWADOGO, T., HAN, Y. and MUREITHI, N. W. (2014). Implementation in vibic of an improved time-domain simulation model for fluidelastic instability in tube arrays. *ASME 2014 Pressure Vessels and Piping Conference*. American Society of Mechanical Engineers.

SAWADOGO, T. and MUREITHI, N. W. (2014a). Fluidelastic instability study in a rotated triangular tube array subject to two-phase cross-flow. part i: Fluid force measurements and time delay extraction. *Journal of Fluids and Structures*, 49, 1–15.

SAWADOGO, T. and MUREITHI, N. W. (2014b). Fluidelastic instability study on a rotated triangular tube array subject to two-phase cross-flow. part ii: Experimental tests and comparison with theoretical results. *Journal of Fluids and Structures*, 49, 16–28.

SCOTT, P. (1987). *Flow Visualization of Cross-flow Induced Vibrations in Tube Arrays*. Master's thesis, McMaster University, Hamilton, Ontario, Canada.

SENEZ, H. and ÉTIENNE, S. (2011). Development of a numerical model to represent two-phase flow configurations in a tube bundle. *ASME 2011 Pressure Vessels and Piping Conference*. American Society of Mechanical Engineers, 195–209.

SHAHRIARY, S., MUREITHI, N. W. and PETTIGREW, M. J. (2007). Quasi-static forces and stability analysis in a triangular tube bundle subjected to two-phase cross-flow. *ASME 2007 Pressure Vessels and Piping Conference*. American Society of Mechanical Engineers, 245–252.

TANAKA, H. and TAKAHARA, S. (1980). Unsteady fluid dynamic force on tube bundle and its dynamic effect on vibration. *Flow-Induced Vibration of Power Plant Components - PVP New York ASME*, 41, 77–92.

TANAKA, H. and TAKAHARA, S. (1981). Fluidelastic vibration of tube array in cross-flow. *Journal of Sound and Vibration*, 77, 19–37.

TANAKA, H., TAKAHARA, S. and OHTA, K. (1983). Flow-induced vibration of tube arrays with various pitch-to-diameter ratios. *ASME Journal of Pressure Vessel Technology*, 104, 168–174.

WATTEAUX, R. (2008). *Étude des facteurs d'influence d'un faisceau de cylindres dans un écoulement transverse à bas régime*. Master's thesis, École Polytechnique de Montréal.

WATTEAUX, R., MUREITHI, N. and PELLETIER, D. (2007). Determination of Coupling Force Derivatives in Tube Bundles Using the Shape Sensitivity Equation Method. *ASME 2004 Pressure Vessels and Piping Conference*. American Society of Mechanical Engineers, San Antonio, TX, United states, 263–270.

WEAVER, D. S. and FITZPATRICK, J. A. (1988). A review of cross-flow induced vibrations in heat exchanger tube arrays. *Journal of Fluids and Structures*, 2, 73 – 93.

WEAVER, D. S. and GROVER, L. K. (1978). Cross-flow induced vibrations in a tube bank—turbulent buffeting and fluid elastic instability. *Journal of Sound and Vibration*, 59, 277–294.

WEAVER, D. S. and LEVER, J. H. (1977). Tube frequency effects on cross flow induced vibrations in tube arrays. *Proceedings of the Fifth Biennial Symposium on Turbulence*. vol. 1, 323–331.

YEUNG, H. C. and WEAVER, D. S. (1983). The effect of approach flow direction on the flow-induced vibrations of a triangular tube array. *Journal of Vibration and Acoustics*, 105, 76–81.

ZHU, J. Z. and ZIENKIEWICZ, O. C. (1987). A simple error estimator and adaptive procedure for pratical engineering analysis. *Int. J. Numer. Meth. Eng.*, 24, 337–357.

CHAPITRE 4

ARTICLE 2 : TWO-PHASE DAMPING FOR INTERNAL FLOW : PHYSICAL MECHANISM AND EFFECT OF EXCITATION PARAMETERS

Cet article a été soumis au *Journal of Fluids and Structures*.

C. Charreton, C. Béguin, A. Ross, S. Étienne & M. J. Pettigrew
BWC/AECL/NSERC Chair of Fluid-Structure Interaction
Department of Mechanical Engineering, École Polytechnique,
P.O.Box 6079, succ. Centre-Ville, Montréal (Québec), Canada, H3C 3A7

Abstract

Two-phase flow induced-vibration is a major concern for the nuclear industry. This paper provides experimental data on two-phase damping that is crucial to predict vibration effects in steam generators. An original test section consisting of a tube subjected to internal two-phase flow was built. The tube is supported by linear bearings and compression springs allowing it to slide in the direction transverse to the flow. An excitation system provides external sinusoidal force. The frequency and magnitude of the force are controlled through extension springs. Damping is extracted from the frequency response function of the system. It is found that two-phase damping depends on flow pattern and is fairly proportional to volumetric fraction for bubbly flow. Measurements are completed by the processing of high-speed videos which allow to characterize the transverse relative motion of the gas phase with respect to the tube for bubbly flow. It is shown that the bubble drag forces play a significant role in the dissipation mechanism of two-phase damping.

Keywords: Two-phase, damping, flow pattern, bubble motion

4.1 Introduction

Two-phase flow induced vibration in steam generators is well documented in the literature (Pettigrew and Taylor, 1991; Weaver and Fitzpatrick, 1988; Au-Yang *et al.*, 2000). Extensive experimentations have been carried out over the last forty years to get a better hand on the several excitation mechanisms involved, such as quasi-periodic forces or fluidelastic instability. Review and design guidelines for heat exchangers constructors have been proposed, improving nuclear power plant safety and reliability. The duality of two-phase flows from a vibration point-of-view lies in the fact that they bring about destructive phenomena

while causing significant damping on the structure. Damping is a crucial input parameter to predict vibration effects in steam generators. However, the nature of the damping is not well understood. A better knowledge of the physical mechanism involved would lead to improved modeling of vibration effects in the near future.

The first experimental studies on two-phase damping were performed by Carlucci (1980) and Carlucci and Brown (1983). For a cylinder confined in axial two-phase flow, they found that total damping is strongly dependent on void fraction. Moreover, the two-phase damping component is much higher than the damping due to fluid viscosity for single-phase flow. It can reach up to 3%. Hara and Kohgo (1985) derived an analytical model for a cylinder confined in axial-two-phase flow. They modeled the gas phase as columns having no mass nor stiffness. Cylinder and gas motions were described by beam equations, coupled by the fluid forces. Coupling coefficients were extracted from potential flow theory. The eigenvalue problem was solved to find the damping coefficients which compared well with the experiments. However, this approach does not provide a physical explanation for the mechanism. More recently, Uchiyama (2003) proposed a numerical simulation, also for a cylinder confined in two-phase flow, assuming a bubbly flow. Damping values of the same order of magnitude as in Carlucci and Brown (1983) were observed. However, the damping ratio goes down to zero for void fractions higher than 60%, which is not verified experimentally. This fact raises questions about the applicability of numerical codes for high void fraction. Indeed, these codes assume bubbly flow but usually do not take flow pattern transitions into account. Nevertheless, Uchiyama (2003) explains damping by "the phase lag of the drag force acting on the cylinder behind the cylinder displacement". This introduces a notion of relative displacement inherent to the two-phase mixture.

Two-phase damping has also been measured for cross-flow. It is undoubtedly the most important flow configuration since most vibration mechanisms are critical in the U-bend region of the steam generator. Semi-empirical relations for design purposes are given by Pettigrew and Taylor (2004). They compiled a considerable amount of data to identify the most influent parameters. It was shown that flow velocity and tube frequency have minor influence, contrary to confinement and surface tension. Therefore, several phenomena are potential dissipative mechanisms that could be responsible for two-phase damping. Mainly, flow structure, relative motion of gas phase and liquid phase and coalescence/breakup of bubbles are suspected.

Other studies were steered towards the influence of fluid properties on two-phase damping at Ecole Polytechnique of Montreal. These were performed for internal axial flow on clamped-clamped tubes. This configuration is less interesting from a practical point-of-view since in CANDU nuclear plants, pressurized heavy water is supposed to be almost liquid inside steam

generator tubes. Still, it is interesting to notice that two-phase damping *vs* void fraction curves are oddly the same for the three flow configurations reported : annular, internal axial and cross-flow (see Carlucci and Brown (1983), Gravelle *et al.* (2007), and Pettigrew and Taylor (2004) respectively). This suggests that the mechanism involved is the same for each case. From a design point-of-view, internal axial flow configuration is the simplest. Gravelle *et al.* (2007) reported damping measurements in 20 mm tubes. The decrease of two-phase damping at the transition between bubbly and slug flow is explained by the decrease of interface surface area when slugs appear. This is somehow contradictory with Pettigrew and Knowles' (1997) observations: ζ was found to increase with surface tension σ. A possible explanation given was that bigger bubbles are more prompt to dissipate energy. This work was pursued by Béguin *et al.* (2009b) who tested several air-liquid mixtures, in order to assess the effect of viscosity and density on two-phase damping. Béguin *et al.* (2009a) also performed two-phase damping experiments with rigid spheres in sedimentation in stagnant liquids. It appeared that density difference between phases has a major effect, contrary to the viscosity. Damping values with rigid spheres were somehow smaller than in air-liquid mixtures by a factor 2, but proportionality with respect to interface surface area was confirmed. For large number of spheres, interaction occurring between spheres (*e.g.* onset of coalescence in case of a gas phase) seems to modify this trend. Béguin *et al.* (2009a) also presented a 2D model of a bubble in an oscillating tube filled with liquid, and solved the Navier-Stokes equations analytically. They showed that viscous dissipation due to the presence of a bubble can be related to the relative motion of the bubble with respect to the structure.

These conclusions motivated the design of a new test section which would not only allow damping measurements but also let us observe the gas phase behavior. Also, damping values have only been extracted at the natural frequency of the considered system so far. Thus, the objective of this project is to measure two-phase damping accurately, so as to relate it to the relative motion of the gas phase that we also measured.

In the next section, a new test rig is presented. It allows to command excitation parameters, such as frequency, on a structure subjected to internal two-phase flow. This leads to interesting information on the nature of the two-phase flow energy dissipation. Then, the experimental parameters involved in the system are described. In Sec. 4.4, the technique to extract the two-phase damping component of the oscillating structure is presented. Results on damping and the relation with flow patterns are described afterwards. Then, in Sec. 4.6, the motion of the gas phase is characterized with the processing of high-speed videos. It is related to the two-phase values through an analytical model of the forces exerting on the bubbles in Sec. 4.7.

4.2 Experimental setup

The experimental setup is comprised of several features that will be described separately for the sake of clarity.

Sliding tube: The section itself is a stiff aluminum square tube. The hydraulic diameter D_h is 76.2 mm and the length L is 1 m. It is vertically mounted and supported by four linear bearings installed on two parallel shafts. This feature allows the tube assembly to slide in the y-direction only, transverse to the flow (cf. Fig. 4.1). The linear bearings are self-aligning to minimize friction in the system. Three panels of the tube are transparent, and the square section prevents refraction effects, allowing a good visualization of the flow.

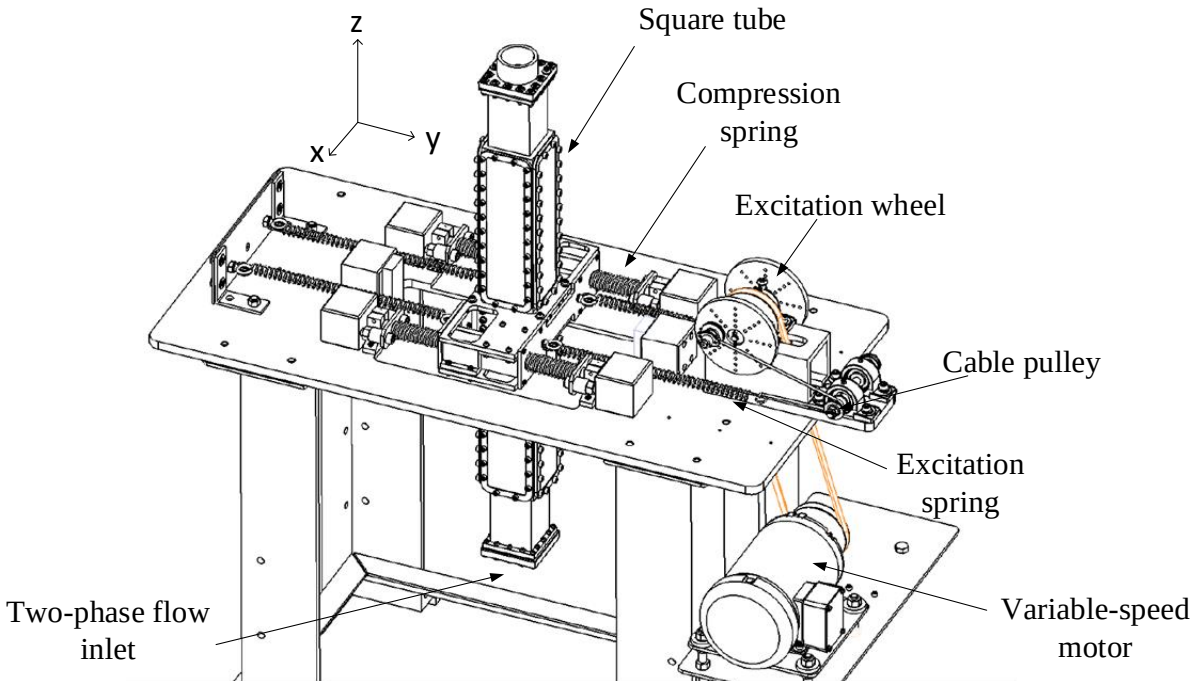

Figure 4.1 Test section (pipe system not shown).

Compression system: Four compression springs of stiffness k_c and concentric with the rods retain the test section in the y-direction. One of their ends is in contact with the tube assembly and the other with what we refer to as compression plates. These are bolted with the sturdy bench structure via threaded rods. They can be displaced along those threaded rods to set an initial compression to the springs. This is an important feature since it prevents the tube assembly from impacting the two sets of springs when oscillating. The four springs are always working. However, the maximum amplitude that the system can reach is equal to

the length of the initial compression. Beyond that point, the tube assembly would disconnect from a pair of springs. The compression springs used in the present study have a free length of 152 mm and the initial compression is 45 mm. The tube assembly behaves like a classic mass-spring system, from a structural point-of-view.

Excitation system: The "mass-spring system" is forced with a simulated sinusoidal excitation, provided through extension springs of stiffness k_e. A motor drives an excitation wheel (cf. Fig. 4.1) via a pulley. A cable is attached to a shoulder-bearing system screwed eccentrically on the excitation wheel. The rotary motion is converted via the cable-pulley system into a sinusoidal motion of the extremity of extension springs (cf. Fig. 4.1). Since the extension springs are always stretched, the tube undergoes a sinusoidal force. We can control its magnitude F_0 by changing the eccentricity e on the excitation wheel. The latter is drilled with multiple tapped holes at different positions. The excitation frequency ω can be changed using the variable-frequency drive that pilots the motor.

Notice the symmetry of the system with respect to the yz-plane: it is excited through two springs. Two additional extension springs are supporting the tube on the left side of the bench on Fig. 4.1, to ensure symmetry with respect xz-plane. All the springs, including compression springs, were tested on a traction-compression machine in order to verify their linearity over their range of operation. Dynamic stiffnesses have not been tested but are neglected since the excitation frequencies are very low (around 6Hz).

Hydraulic loop: In order to allow the transverse motion of the oscillating tube under internal flow, we use two flexible hoses that are fitted on both ends of the tube, and to the rest of the rigid pipe system on the other end. The flexible hoses are corrugated to ensure local pressure resistance and global flexibility, so as to not affect the tube motion. Also, their lengths were chosen so as to avoid an unbalancing mass effect at mid-section induced by water presence and make sure that they "follow" the tube smoothly.

The hydraulic loop works as follows: a centrifugal pump takes water from a reservoir. Air is injected just upstream the test section, as illustrated in Fig. 4.2. A mixer placed in the circular to square expansion homogenizes the air-water mixture. The mixture flows upward through the test section and then back to the tank at atmospheric pressure, where the phases separate.

Measurement system: The position of the tube is measured in time with laser sensors. They yield a resolution lower than 12 μm. The acquisitions are performed at a sampling rate of 2048 Hz. Key parameters of the system are highlighted in Tab. 4.1.

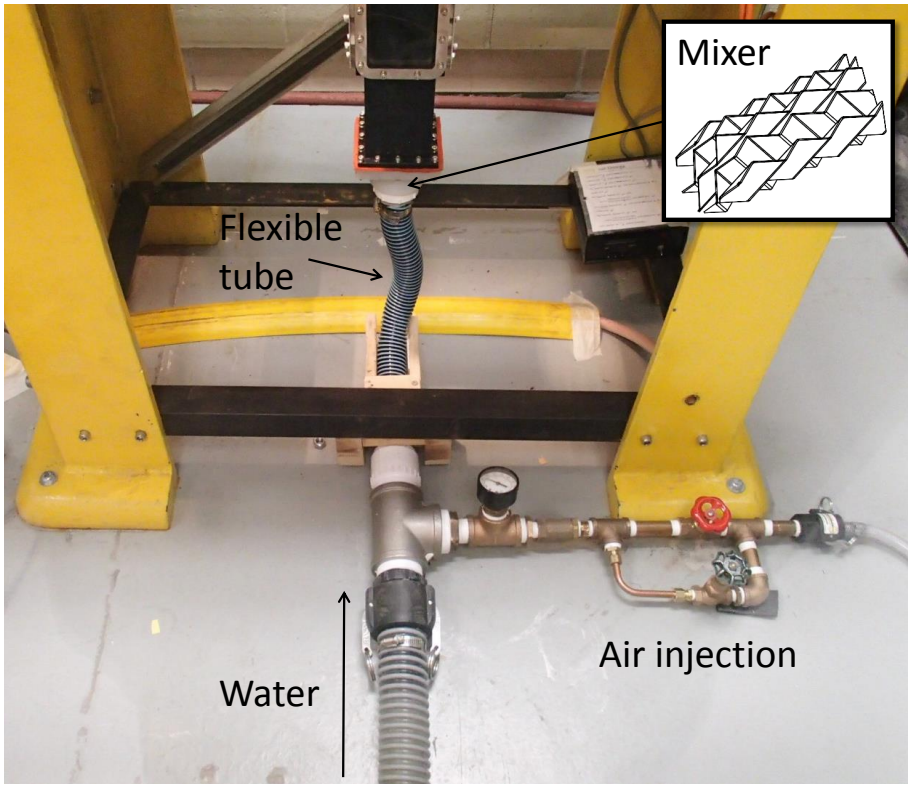

Figure 4.2 Air injection upstream to the test section.

4.3 Experimental parameters

4.3.1 Two-phase flow parameters

Two-phase flow in a tube can be defined either by the void fraction ε in a portion ΔL or by the volumetric fraction β (Collier and Thome, 1994). The void fraction represents the proportion of gas volume over the total volume:

$$\varepsilon = \frac{V_g}{V_g + V_l} = \frac{A_g \Delta L}{A_g \Delta L + A_l \Delta L} = \frac{A_g}{A_g + A_l} \tag{4.1}$$

where A_k is the area occupied by phase k in a given section of the tube. The void fraction would require specific instrumentation such as capacitance or fiber optic probes to be accurately determined. On the other hand, the volumetric fraction only requires the volume flow rates of each phase:

$$\beta = \frac{Q_g}{Q_g + Q_l} = \frac{A_g \langle u_g \rangle}{A_g \langle u_g \rangle + A_l \langle u_l \rangle} = \frac{A_g}{A_g + A_l / s} \tag{4.2}$$

Table 4.1 Characteristics of the system.

Property	Notation	Value/Range
Hydraulic diameter	D	76.2 mm
Length	L	1 m
Mass of tube assembly	m_s	16.4 kg
Compression spring constant[1]	k_c	6545 N/m
Extension spring constant[1]	k_e	474 N/m
Natural frequency[2]	f_n	6.4 Hz
Excitation force	F_0	23 - 69 N

[1] Average of measured values over the four springs.
[2] Theoretical value for the unconnected empty tube.

where s is the slip ratio between the average velocities of the phases: $s = \langle u_g \rangle / \langle u_l \rangle$. Note that $\varepsilon = \beta$ if $s = 1$, which is the definition of a homogeneous flow.

We characterize the mixture velocity using the definition of superficial velocity:

$$j = \frac{Q_g + Q_l}{A} \tag{4.3}$$

The experiments were performed at constant j, using the fact that $j_g = \beta j$ and $j_l = (1-\beta)j$. Volumetric flow rates are both measured with appropriate flow meters.

4.3.2 Sources of damping

The presence of fluid around a structure will affect its damping. Carlucci and Brown (1983) identified several sources of damping:

$$\zeta_t = \zeta_s + \zeta_f + \zeta_\nu + \zeta_{2\varphi} \tag{4.4}$$

(i) ζ_s : **Structural** damping is caused by the energy losses inherent to the motion of a structure. In our case, it is due to the friction in the linear bearings and inner losses in the springs. Its value is obtained by determining the oscillating characteristics of the system while no fluid is flowing through ($j = 0$).

(ii) ζ_f : When water is flowing through a slender pipe, the latter can warp and oscillate under fluid force. This force causes a damping effect at the elbows: it is the **fluid** damping mechanism. Since our structure is practically stiff, ζ_f can be neglected.

(iii) ζ_ν : Fluid friction on the sides of the test section induces **viscous** damping, which

depends on fluid properties, fluid velocity and channel geometry. As can be seen on Fig. 4.3, it is negligible at 100% void fraction, and is monotonic until 0% (water only). Even there, ζ_ν is small compared to $\zeta_{2\varphi}$. We determine ζ_ν at $\varepsilon = 0\%$. Then, it is assumed that ζ_ν decreases linearly with ε and is null at $\varepsilon = 100\%$ for a given superficial velocity of the mixture.

(iv) $\zeta_{2\varphi}$: The **two-phase** component is obtained by subtracting the aforementioned components from the measured total damping ζ_t.

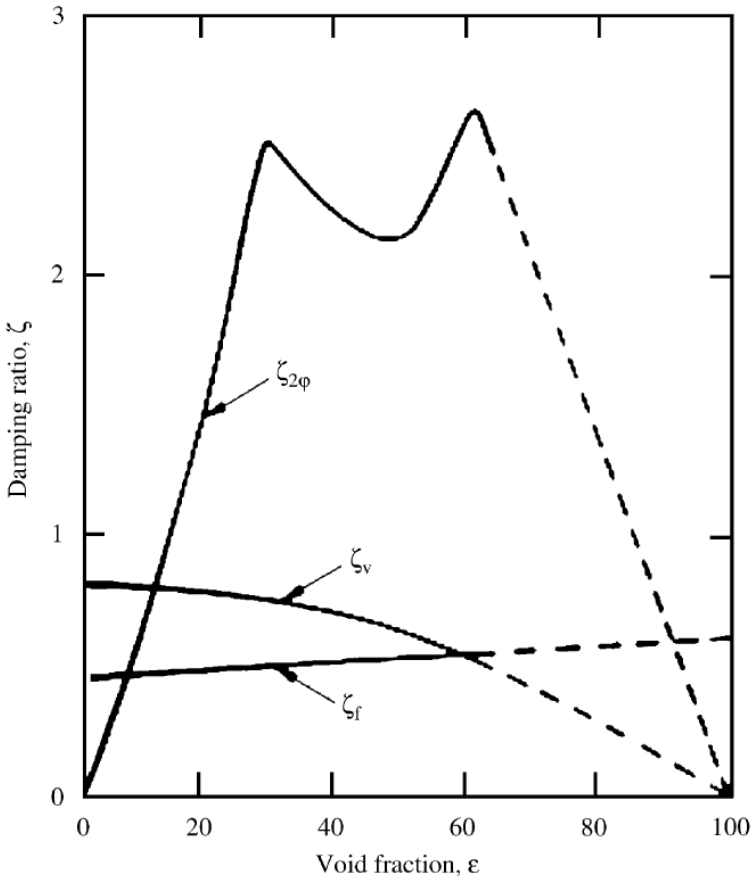

Figure 4.3 Components of total damping in two-phase flow, Carlucci (1980).

This formulation suggests that all the components are purely velocity dependent. This is not the case for this system, as dry friction occurs in the linear bearings. Sec. 4.4 aims at describing how the two-phase component is therefore extracted.

4.4 Experimental technique

4.4.1 Structural damping

Information on the nature of structural damping is determined by analyzing the free vibrations of the system. The empty tube was initially displaced by 20 mm and then released. The result is shown on Fig. 4.4. The linear envelope is typical of Coulomb friction, occurring

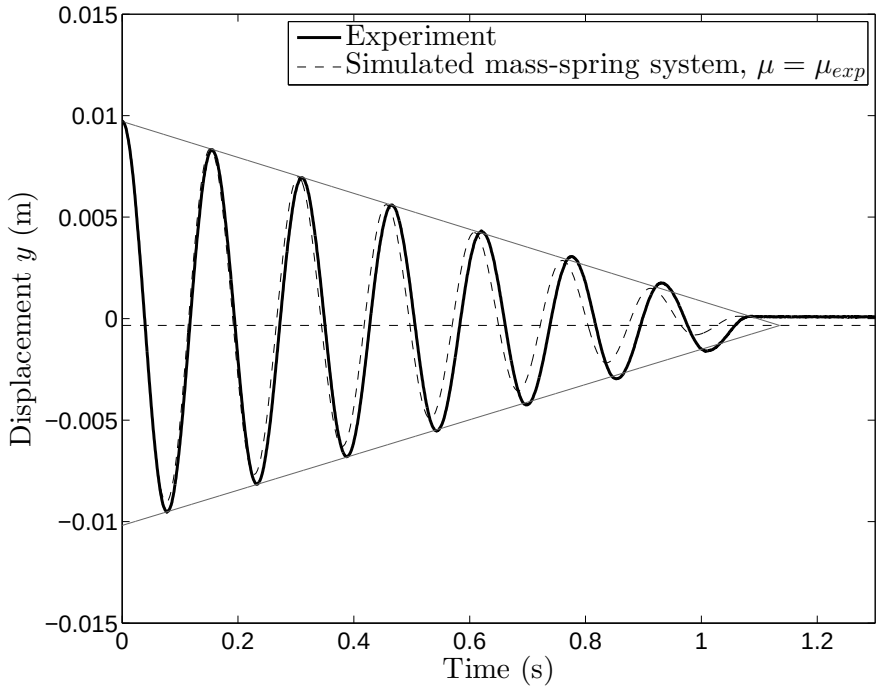

Figure 4.4 Free response of the empty tube after an initial displacement.

in the linear bearings. It is explained by the fact that a constant amount of energy is extracted from the system at each cycle, meaning that it is not velocity dependent. Since in this case, we know the weight of the tube assembly, we can calculate a friction coefficient μ of 0.06 per bearing. This value is inside the expected range [0.04, 0.07] for linear bearings (Van Beek, 2006), where friction is indubitably higher than in roller bearings. In order to test the effect of mass and frequency, the tube assembly was ballasted with several masses or stagnant water, and different springs were used. As a result, total mass m over structural mass m_s was varied within [1, 1.6] and natural frequency within [10, 30] rad/s. Coulomb friction coefficient was found to vary within [0.04, 0.08].

In theory, pure Coulomb friction allows an infinite response at resonance for a mass-spring system, for low values of μ such as in our case (Den Hartog, 1956). Therefore, a combination of Coulomb friction and viscous damping is commonly used. A more elaborate friction model

(Olsson *et al.*, 1998) did not prove to be necessary, as the tube is constantly sliding (no stick-slip phenomena, for instance, are involved). We then introduce ζ_s, the viscous component due to structural losses. The determination of μ and ζ_s, along with the other sources of damping, requires an appropriate modeling of the system for operating conditions.

4.4.2 System modeling

A top view of the test section is provided on Fig. 4.5(a). We can identify the four compression springs and the two pairs of extension springs, clamped on the right hand side and excited on the left hand side.

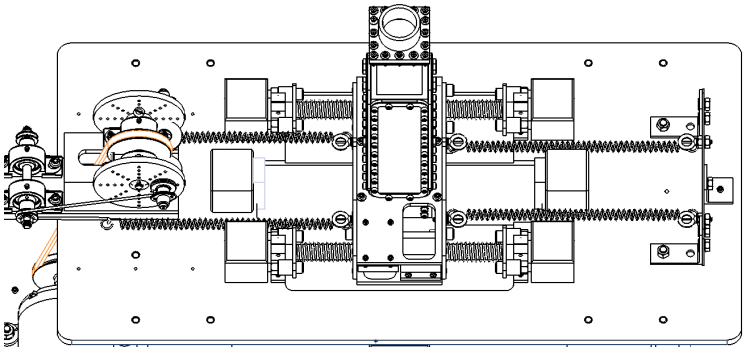

(a) Excitation system and sliding structure

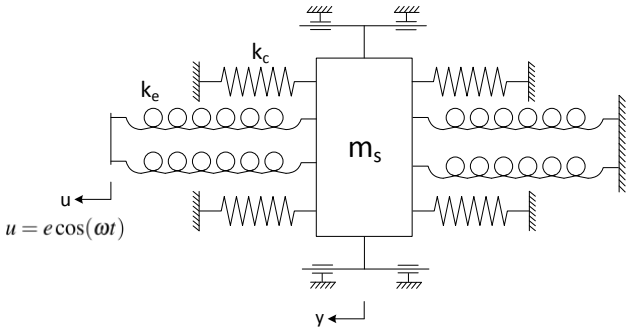

(b) Full system model

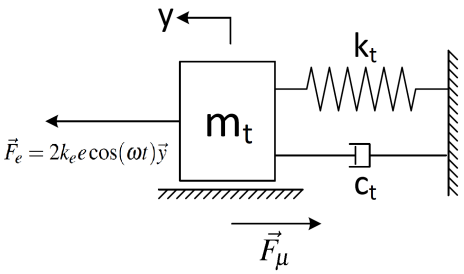

(c) Equivalent system

Figure 4.5 System modeling.

Fig. 4.5(b) shows the full system model from a structural point-of-view. The mass of the tube assembly is noted m_s. The springs are considered to be linear, based on the traction-compression tests mentionned earlier in this paper. The excitation springs are subject to a sinusoidal displacement. We isolate the forces (including the different sources of damping and friction) on the free body diagram of the tube assembly. Remembering that because of the initial compression, all the springs are always working, the equivalent variables of the

system under operating conditions (Fig. 4.5(c)) are:

$$\text{Force magnitude} \;:\; F_0 = 2k_e e \tag{4.5}$$

$$\text{Stiffness} \;:\; k_t = 4k_e + 4k_c \tag{4.6}$$

$$\text{Damping} \;:\; c_t = c_s + c_\nu + c_{2\varphi} \tag{4.7}$$

$$\text{Mass} \;:\; m_t = m_s + m_{2\varphi} + m_a \tag{4.8}$$

The total damping coefficient c_t is the sum of the three aforementioned components. $m_{2\varphi}$ is the mass of fluid vibrating with the structure and can be deduced from ε and tube geometry. m_a is the added mass, due to a relative motion between the liquid and the structure. The equation of motion of the structure in direction $\vec{y}$, for a given excitation frequency ω, is:

$$m_t\ddot{y} + c_t\dot{y} + k_t y = F_f(\dot{y}) + F_e(t) \tag{4.9}$$

$$= -\mu m_t g\,\mathrm{sgn}(\dot{y}) + 2k_e e\cos(\omega t) \tag{4.10}$$

It can be rewritten as:

$$\ddot{y} + 2\zeta_t\omega_n\dot{y} + \omega_n^2 y = -\mu g\,\mathrm{sgn}(\dot{y}) + \frac{2k_e e\omega_n}{k_t}\cos(\omega t) \tag{4.11}$$

with the damping ratio ζ_t and the natural frequency ω_n defined as usual as:

$$\zeta_t = \frac{c_t}{2\sqrt{k_t m_t}} \text{ and } \omega_n = \sqrt{\frac{k_t}{m_t}} \tag{4.12}$$

The total damping ratio is non-dimensionalized by the total mass, including the added mass. In this case, the added mass is negligible compared to m_s and $m_{2\varphi}$. The relative error is estimated to be lower than 3% on ζ_t.

Eq. (4.11) is non-linear because of the friction force. Thus, finding an analytical expression for ζ_t is far from straightforward. The next paragraph describes the method to retrieve variables of Eq. (4.12) from the frequency response function of the system.

4.4.3 Protocol

The position of the tube is acquired with the laser sensors. The time domain samples have a duration of 20 seconds. A typical tube response is shown on Fig. 4.6. The RMS amplitudes of tube Y_s^{rms} and excitation frequencies ω are extracted from these samples.

This operation is repeated by increasing ω with the variable frequency drive in order to cover the resonance peak of the structure in the frequency spectrum. The frequency

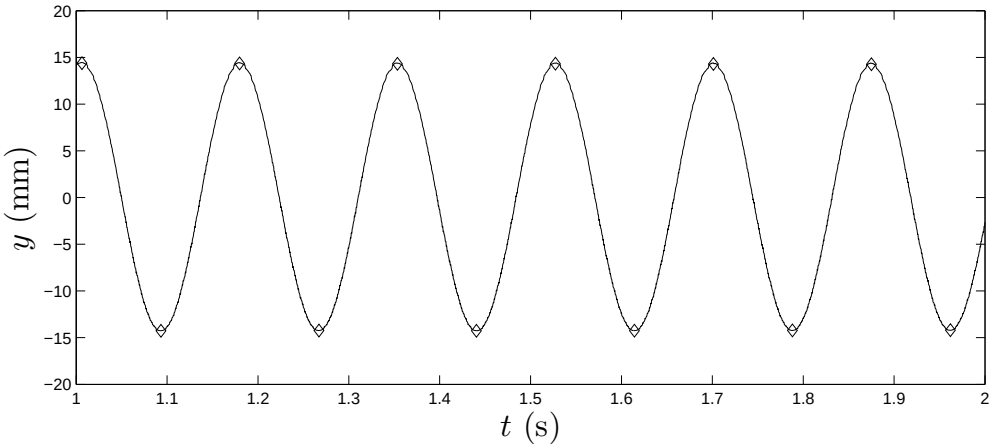

Figure 4.6 Measured position signal of the tube.

resolution that we get on the tube (including power transmission ratios) is 0.03 Hz. This frequency sweep allows to construct the frequency response function of the tube, as illustrated on Fig 4.7.

The black and gray curves calculated for a linear system ($\zeta = 2.2\%$ and $\zeta = 6.0\%$ respectively) have been overlaid to illustrate the slight non-linearity of the system. Around resonance, the experimental points are closer to the black curve whereas when excited farther away from the natural frequency, they are closer to the grey curve.

The natural frequency of the system is extracted from a polynomial fit around the resonance point. Then, we use the least-squares method to find values for μ and ζ_t of Eq. (4.11). Indeed, we do not know the weight supported by the bearings when there is flow. The bottom flexible tube may pull the tube assembly down whereas the flow going up might reduce the force on the bearings. Since the peak of resonance is well defined (ζ_t is expected to be smaller than 6%), only a narrow range of excitation frequency is required to accurately determine the damping. Therefore, we consider μ to be constant over a frequency response function for given conditions. So, Eq. (4.11) is solved for all the frequencies tested, the RMS amplitudes are calculated and compared with the experimental values. μ and ζ_t are found to best fit the experimental data in the frequency domain. The result is summarized by the dotted line on Fig 4.7.

Note on Eq. (4.10) that the model suggests that the total mass m_t is supported by the bearings. Since a smaller value for the mass is expected in reality (as explained in the previous paragraph), the compensation is done directly on the friction coefficient. The values of μ for the conditions tested lie within [0.025, 0.045], just below the range expected from the free vibration tests, where the total mass of the system was supported by the bearings in this case. This confirms that the non-linearity of the system can be explained by Coulomb

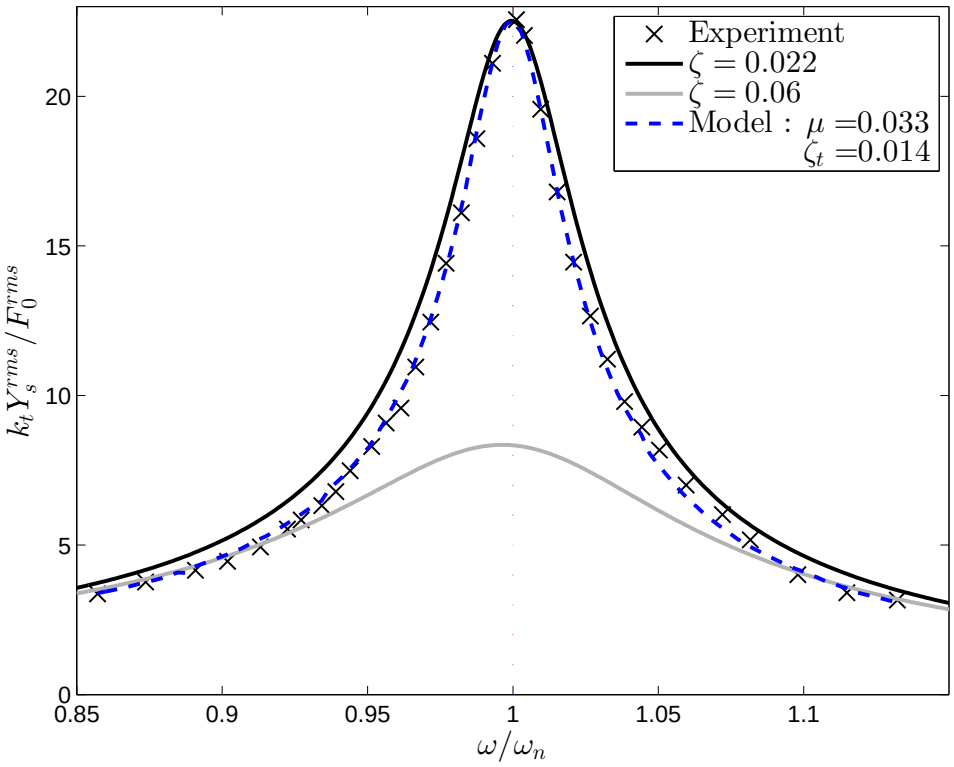

Figure 4.7 Frequency response function of the system ($F_0 = 23$ N, $j = 0.7$ m/s, $\beta = 30\%$).

friction induced by the bearings only. Furthermore, the good agreement between the model and experiments shows that two-phase damping can be modeled as a velocity dependent damping.

4.5 Results

4.5.1 Influence of fluid velocity

Total damping results are shown on Fig. 4.8 as function of volumetric fraction β, for the three superficial velocities of the mixture tested. Each point is the average over three measurements. First-of-all, we can see for $\beta = 0\%$ that $\zeta_s + \zeta_\nu$ is fairly small, of the order of 0.5 to 1%. Then, damping seems proportional to volumetric fraction until a change in slope occurs (vertical dashed line). This transition corresponds to the transition between bubbly and churn regimes, as will be discussed in Sec. 4.5.2. The breakdown in damping values was related to the change in interface surface area by Gravelle *et al.* (2007). As anticipated, the two-phase damping values are very high and reach 3%. However, damping is expected to go down for high volumetric fraction, since the flow becomes air single-phase. This behavior can be explained with Fig. 4.9.

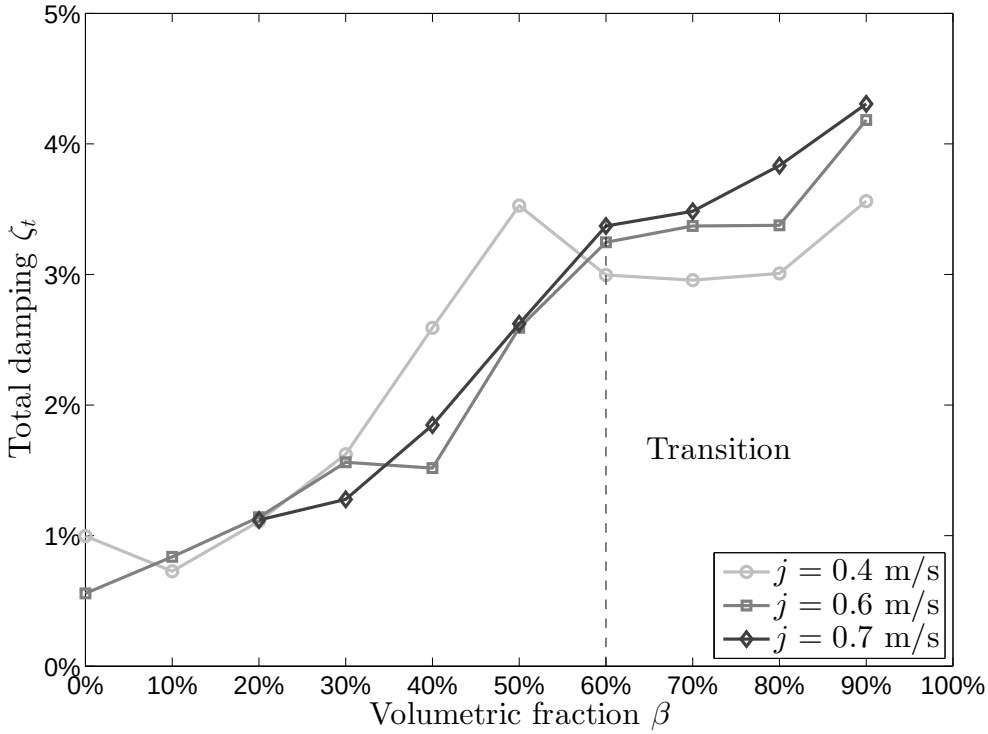

Figure 4.8 Influence of fluid velocity on total damping.

Fig. 4.9 shows the evolution of the natural frequency of the system. When β is increased, the mass of the vibrating fluid decreases. Thus, the natural frequency of the total system increases. The dotted line represents the expected natural frequency in the context of a perfectly homogeneous flow, neglecting pressure and added mass effects. It can be observed that when the volumetric fraction is increased in the experiments, the response gets farther away from the line. On the other hand, when superficial velocity is increased, results get closer to the line. This proves that the higher the velocity, the more homogeneous the flow (void fraction is closer to volumetric fraction). The relation between volumetric fraction and void fraction can be summarized by this equation:

$$s\left(\frac{1}{\beta}-1\right)=\frac{1}{\varepsilon}-1 \tag{4.13}$$

The existence of a slip ratio is inherent to vertical pipes conveying two-phase flow, since gas bubbles undergo buoyancy. For higher void fractions, flow is intermittent because there is no definite continuous phase. The large diameter of our tube amplifies this effect. Stagnant volumes of water are observed and are subject to sloshing which causes an increase in slip ratio. A superficial velocity of 0.7 m/s is the maximum velocity that can be reached with

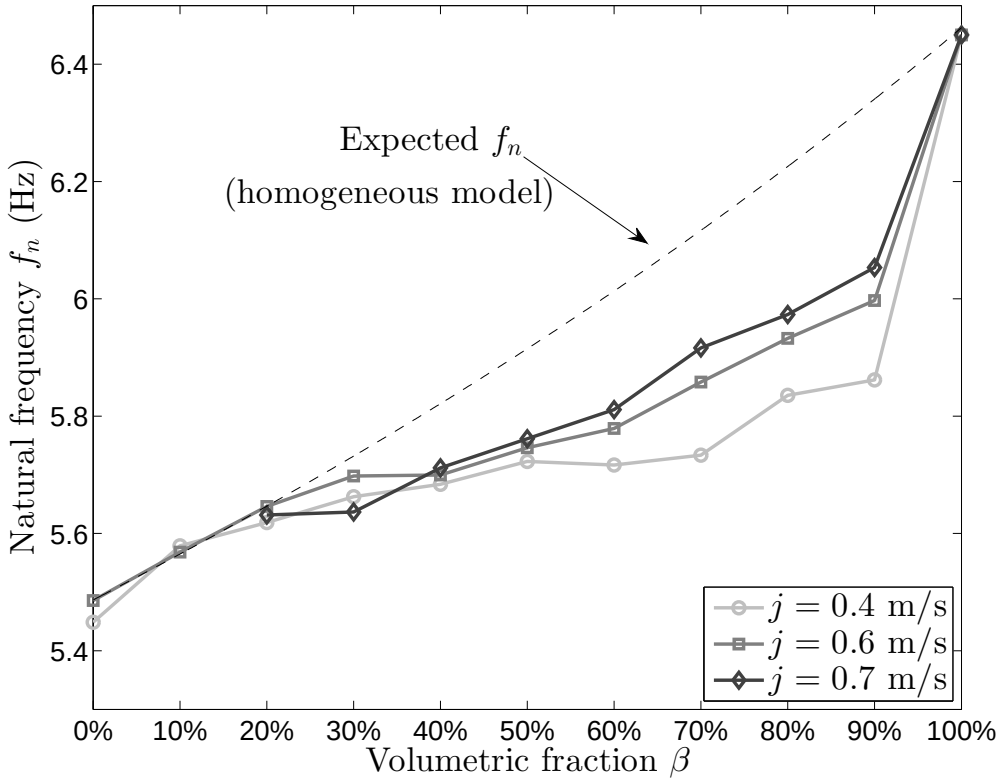

Figure 4.9 Natural frequency of the system for the flow conditions tested. The dotted line represents the expected natural frequency with the homogeneous model.

the current pump.

In the meantime, ω_n is a good qualitative indicator of the actual void fraction in the test section, as described in Sec. 4.5.3. The maximum void fraction that was reached in Fig. 4.8 is estimated to be approximately 60%.

4.5.2 Flow patterns

Videos of the flow were taken with a high-speed camera. Selected photographs of each volumetric fraction are shown on Fig. 4.10 for a superficial velocity of 0.7 m/s. Bubbly flow can clearly be observed up to $\beta = 40\%$. The breakdown in damping values occurs during the transition to churn regime. Perturbation due to larger bubbles can be made out for $\beta = 50\% - 60\%$.

We note that no slug flow regime is observed. That is because the length to diameter ratio is $L/D_h = 13$, whereas it should be higher than 20 for slugs to "develop". This had been observed by Ohnuki and Akimoto (2000) who performed void fraction measurements on a very large circular tube of 200 mm inner diameter, and flow conditions comparable to ours.

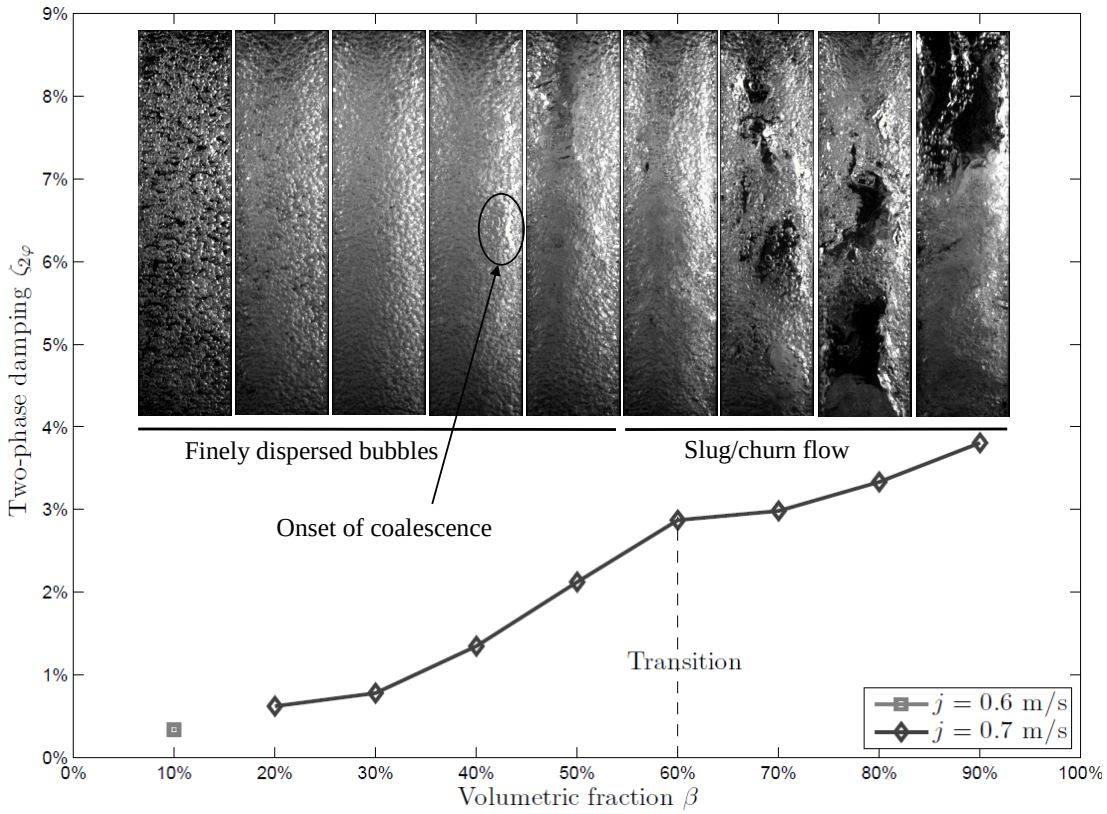

Figure 4.10 Flow patterns.

It was also concluded that churn flow was dominant in large pipes for conditions where slug flow exists in smaller pipes. They also reported a phenomenon that can be clearly observed at 80% volumetric fraction. Large Taylor bubbles intermittently perturb a liquid film still filled with many small bubbles. Prasser *et al.* (2005) note that those large bubbles can however freely move and deform in three dimensions in the large tube and are thus far from ideal Taylor bubbles.

As reviewed by Coleman and Garimella (1999), flow patterns in large circular tubes have been experimented over the years, mostly for horizontal ducts. Flow patterns maps (Mandhane *et al.*, 1974) were derived and compared reasonably well with theoretical ones (Taitel and Dukler, 1976). Rectangular microchannels and minichannels have also been studied and reviewed thoroughly by Cheng *et al.* (2008). Unfortunately, very little information exists on large rectangular channels. Aspect ratio, surface tension, hydraulic diameter and pressure have an effect on transitions in small (around 5 mm) to micro channels. However, these conclusions may not be verified for large vertical square ducts.

An extensive study of flow pattern transition determination would require additional instrumentation. It is beyond the scope of this study. Our observations of the flow are meant

to support damping results and give away the lack of studies in this range of diameter for vertical rectangular ducts.

4.5.3 Influence of excitation force

The magnitude of excitation force was doubled for $j = 0.7$ m/s. In order to ensure repeatability with respect to volumetric fraction, natural frequency is used to compare the results. Indeed, if we neglect added mass, ω_n is related to hydrodynamic mass $m_{2\varphi}$ which depends directly on void fraction ε:

$$\begin{cases} \omega_n = \sqrt{\dfrac{k_t}{m_s + m_{2\varphi}}} \\ m_{2\varphi} = AL(\varepsilon\rho_g + (1-\varepsilon)\rho_l) \end{cases} \tag{4.14}$$

where ρ_g depends on average pressure in the tube, but was found to be below 1.6 bar for all flow conditions. Therefore, it is negligible compared to ρ_l for the void fractions considered. The results are shown on Fig. 4.11.

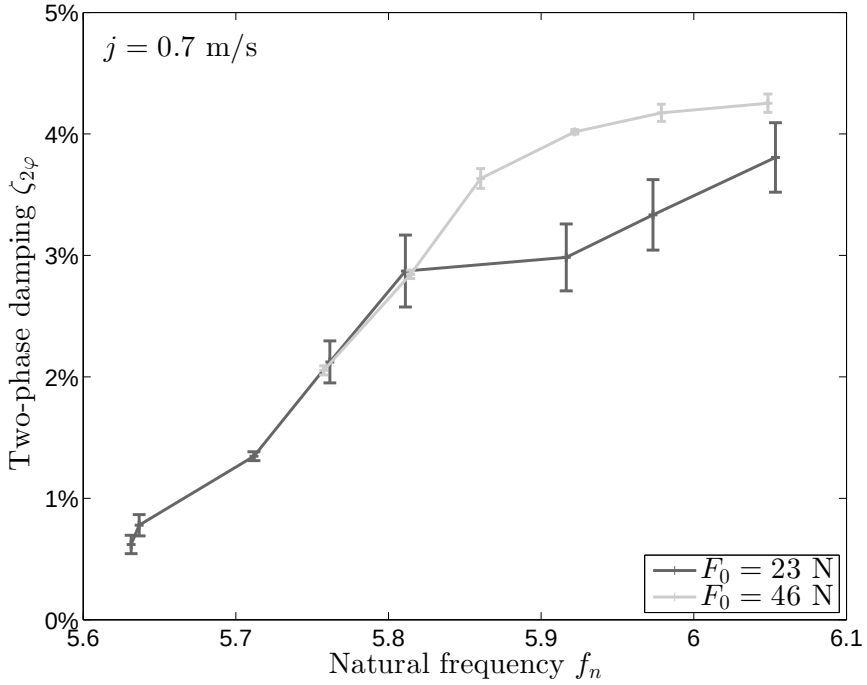

Figure 4.11 Influence of force magnitude. Natural frequency is taken as reference for comparison, since it represents the actual void fraction more accurately (cf. Fig. 4.9). Note that $\zeta_{2\varphi}$ is independent of F_0 for bubbly flow.

Clearly, the excitation force has an effect on transition since the two curves separate after

the transition. The higher the force, the higher the confinement which is likely to affect flow pattern and the damping values for moderately high void fraction. However, it is interesting to notice that the curves match perfectly before transition, for bubbly flow conditions. This independence of $\zeta_{2\varphi}$ with respect to F_0 suggests that the damping mechanism can be modeled as a purely velocity dependent mechanism for bubbly flow. In other words, $\zeta_{2\varphi}$ is independent of excitation amplitude and frequency for bubbly flow. Furthermore, we have depicted the direct dependence of two-phase damping with interface surface area, so we did not expect $\zeta_{2\varphi}$ to depend on force magnitude. This motivated us to steer the study towards the modeling of two-phase damping mechanism for bubbly flow in Sec. 4.7.

4.6 Gas phase behavior

4.6.1 Video processing

The direct relation between interface surface area and two-phase damping is not sufficient to explain the two-phase damping mechanism. We suspect that relative motion between the phases induces dissipation, through the work rate of the forces exerting on the bubbles.

We used a high-speed camera at 1000 fps to characterize the gas phase motion for bubbly flow within the oscillating structure. The objective is to correlate the gas phase motion to the damping values measured. To do so, β should be sufficiently high (for lower volumetric fraction, two-phase damping would be too small to be measured accurately). Unfortunately, the higher the void fraction, the harder the characterization. For instance, Lindken and Merzkirch (2002) presented an accurate measurement of the flow field with bubbles using a combined PIV/shadowgraphy technique. However, the local void fraction around the cluster of bubbles does not exceed 2.5%. The challenge in our case is that many inter-bubble motions were observed, including overlapping. For this reason, individual tracking of the bubbles with image segmentation techniques is laborious.

Therefore, we resorted to a global tracking of the gas phase motion. The method consists in selecting a thumbnail of an image at instant t, and looking for the same thumbnail in the next image at time $t + \Delta t$. We note $f(t)$ the full image matrices taken with the high speed camera, of constant size $(M,\ N)$ at instant t. The indices of the thumbnail position are noted $(i(t), j(t))$. The new coordinates indices $(i(t + \Delta t), j(t + \Delta t))$ are calculated in order to minimize the Mean Square Error (MSE), expressed as:

$$MSE = \sum_{\substack{M/2<I\leq M/2 \\ -N/2<J\leq N/2}} \left[f\left(i(t)+I, j(t)+J\right) - f\left(i(t+\Delta t)+I, j(t+\Delta t)+J\right)\right]^2 \qquad (4.15)$$

The high frame rate was set so that the minimization could be performed in a region of pixels close to the original thumbnail. The thumbnail should of course be initialized in the middle of the gas phase. At each time step, the new thumbnail is used to look for the next one. This evolution of $f\left(i(t), j(t)\right)$ tends to average the inter-bubble motion and gives a good representation of the bulk gas phase motion.

The resolution is around 1 pixel = 0.2 mm. While very simple and robust, the drawback of this technique is that its accuracy can only be appreciated qualitatively.

On Fig. 4.12, one can directly observe the gas phase relative motion with respect to the structure. The images are shown in the tube reference frame. On the first image, the test section is accelerating towards the left, and the gas column is already compressed on the left wall of the tube. This suggests that bubbles are in phase lead with respect to the structure. On the second frame, the tube reaches a zero velocity point, so the gas phase is uniformly dispersed, before being compressed on the right. Notice the white rectangle, standing for the tracked thumbnail. It has moved not only in the transverse direction but also upward. Indeed, upward co-current air-water mixtures are studied.

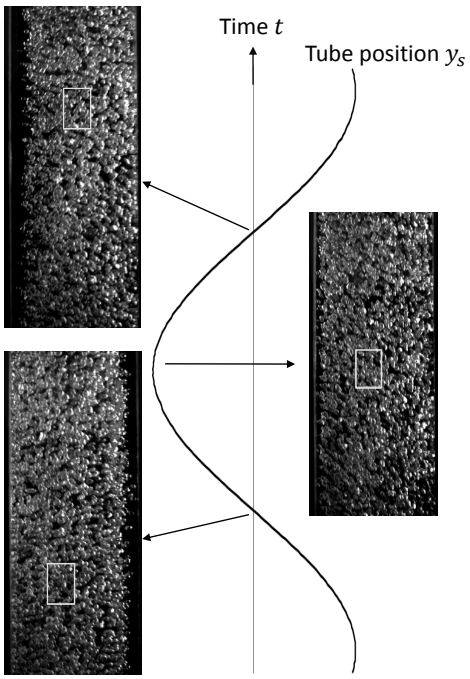

Figure 4.12 Relative motion of the gas phase.

4.6.2 Characterization of gas phase motion

Experiments for three volumetric fractions $\beta = 5,\ 10$ and 15%, at constant superficial velocity $j = 0.6$ m/s. Since the shape of the thumbnail does not change, only one point of its coordinates $(i(t), j(t))$ is required to track the bulk gas phase motion with respect to time. $i(t)$ and $j(t)$ correspond respectively to the vertical and transverse motions. Vertical relative velocity with respect to the liquid $u_{gz} - u_{lz}$, ranges from 0.22 to 0.28 m/s. This is around the expected value of 0.25 m/s (given by the difference between buoyancy and drag force on the bubbles). Those values give a slip ratio s of approximately 1.5. The three corresponding void fractions ε are thus roughly 3, 7 and 11%.

A typical graph of transverse relative motion of the bubbles is shown on Fig. 4.13. The

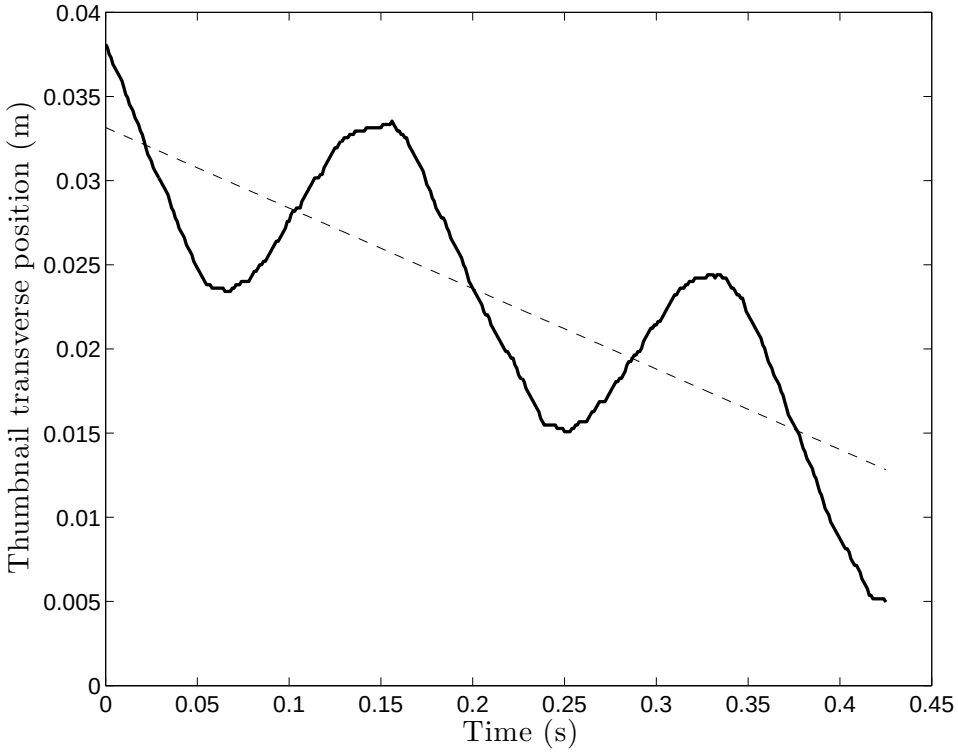

Figure 4.13 Typical unfiltered transverse position of the tracking rectangle in time. It represents the gas phase motion on the front tube wall. The linear deviation is attributed to a global swirling motion of the bubbles.

signal is the combination of a sine wave and a linear deviation, meaning the tracking rectangle is oscillating while drifting towards one side of the tube. Note that only bubbles close to the front window are observed. We attribute the drift behavior to a swirling motion of the bubbles. When the structure is oscillating, a radial instability is onset (the swirling motion was not observed for the tube at rest). When bubbles come into contact with the side

walls, they tend to slide in a preferential direction instead of simply bouncing back and most likely coalesce with other bubbles. This is attested by the photographs in Fig. 4.12 where structural oscillations do not seem to prematurely onset the formation of larger bubbles. A similar behavior had been reported by Béguin *et al.* (2009a). When their clamped-clamped tube was released to measure the free vibrations, they observed elliptical motion instead of oscillations in a plane. This phenomenon was attributed to the cylindrical shape of the tube causing swirling. Our observations suggest that swirling is generated by tube oscillations only, and not by tube geometry. The swirling velocities on the side wall were around 0.05 m/s (slope of the dashed line on Fig. 4.13), which is negligible compared to up to 1 m/s for structure peak velocity. Thus, the swirling motion is not dissipative. However, it prevents coalescence of the bubbles, keeping a constant interface surface area. It could explain why tube oscillations do not seem to affect flow pattern transitions.

Therefore, only the harmonic motion of the gas phase is extracted. The tube amplitude is noted Y_s and the relative motion of the gas phase with respect to the tube is $Y_{b|s}$. Fig. 4.14 shows the different movements of the system involved. Note that the gas phase is in phase lead with respect to the structure.

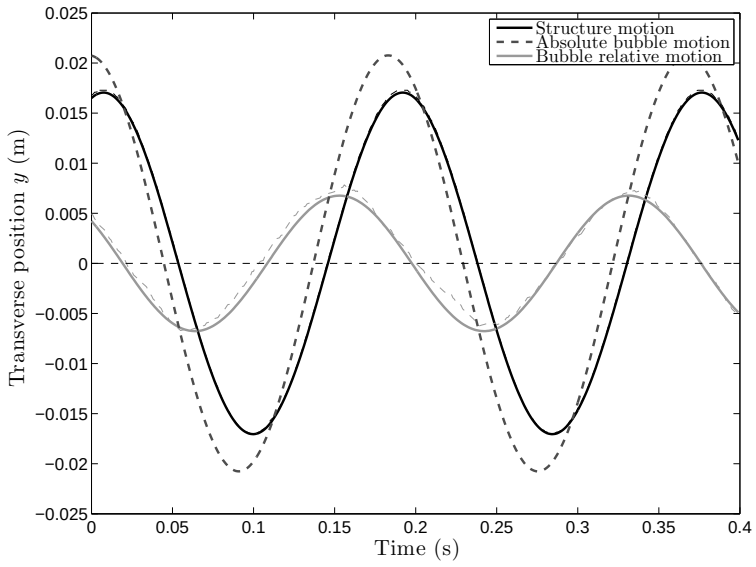

Figure 4.14 Different movements of the system involved. Light dashed lines are the the raw signals extracted from the videos, and solid lines are the corresponding sinusoidal fits.

4.6.3 Amplitude of motion of the gas phase

The relative amplitude $Y_{b|s}$ was extracted for several excitation amplitudes. Y_s was varied by changing the frequency close to the natural frequency of the system for a given void fraction. Since the peak of resonance is very well defined, the excitation frequency can be considered constant at 33.75 ± 1.5 rad/s (6 ± 0.23 Hz) over all our experiments. Results are shown on Fig. 4.15. $Y_{b|s}/Y_s$ represents the gain of the gas in terms of amplitude. For

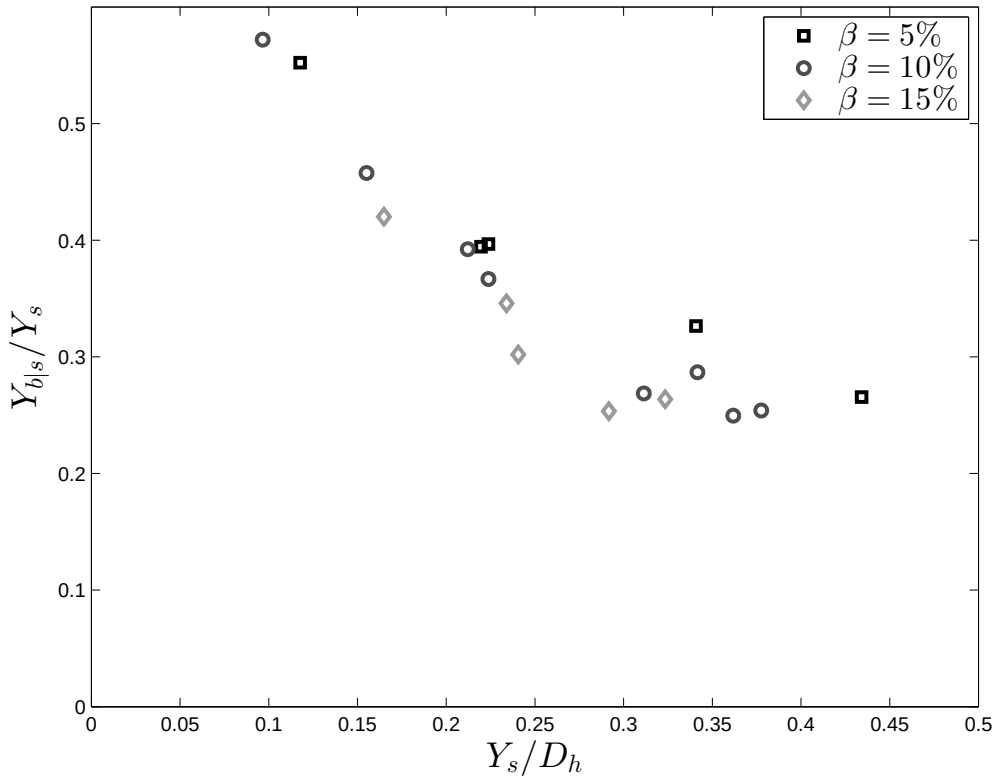

Figure 4.15 Relative amplitude of the gas phase with respect to the structure.

a constant excitation amplitude, the gain of the gas tends to decrease when void fraction increases. This is in accordance with the drag relations that take into account the effect of void fraction (*e.g.* Ishii and Zuber, 1979; Zuber and Hench, 1962). Indeed, it is well-established that C_D increases dramatically with ε through confinement, therefore limiting the transverse amplitude. For high Y_s, the gain seems to reach an asymptote. It is presumed that the tube motion is responsible for an important confinement effect which leads to this limit cycle.

The relative motion can not be related to two-phase damping values without the forces on the bubbles. Therefore, a simple model has to be analytically derived.

4.7 Analytical model

We propose a simple model of a bubble in an oscillating structure subjected to internal two-phase flow. This sections aims at testing existing correlations and implement them in the model under certain hypotheses, to assess the extent to which the two-phase damping can be reproduced. Based on our observations, the transverse relative motion of the gas phase will be the main output of the calculations to explain damping, through the work rate of the forces exerting on the bubbles.

4.7.1 Equation of motion

We consider a deformable bubble of equivalent diameter a. It is immersed in an oscillating structure filled with water, as illustrated by Fig. 4.16. The bubble has the properties of a confined bubble in two-phase flow, of given volumetric fraction and superficial velocity. Thus, its movement is representative of the gas phase motion.

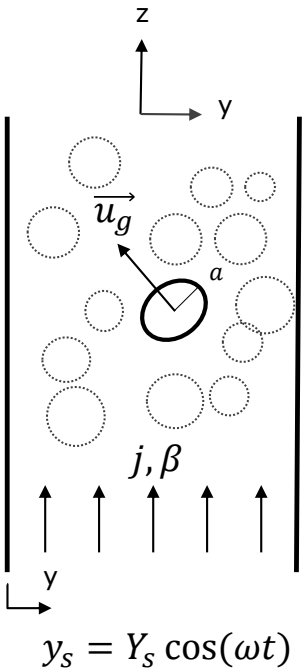

Figure 4.16 Schematic of the bubble model in an oscillating structure subjected to two-phase flow.

We note $\vec{u_b}$ the relative velocity of the bubble with respect to the fluid:

$$\vec{u}_b = \vec{u}_g - \vec{u}_l \tag{4.16}$$

We assume that bubbles do not have influence on the liquid. Thus, the liquid undergoes a solid body motion with the structure. Therefore:

$$\vec{u}_l = (-Y_s \omega \sin(\omega t),\ u_{lz}) \tag{4.17}$$

where u_{lz} is a function of j and ε, the void fraction still being calculated based on volumetric fraction and slip ratio of the bubble.

The 2D equation of motion of the bubble takes the form:

$$m\frac{d\vec{u}_b}{dt} = \vec{F}_B + \vec{F}_D + \vec{F}_M + \vec{F}_I \tag{4.18}$$

where $\vec{F}_B$ is the buoyancy force:

$$\vec{F}_B = \frac{4}{3}\pi a^3 \Delta\rho g \vec{z} \tag{4.19}$$

$\vec{F}_D$ is the drag force, based on bubble relative velocity:

$$\vec{F}_D = -\frac{1}{2}\pi a^2 \rho_l C_D u_b \vec{u}_b \tag{4.20}$$

We calculate the drag coefficient using a relation by Béguin (2010). It is valid for up to Re = 300, and takes the effect of void fraction into account:

$$\begin{aligned}
&C_D = \frac{16}{\mathrm{Re}}\left(1 + \frac{2\left(\dfrac{2+3\bar{\mu}}{2+2\bar{\mu}}\right)^2}{1+\dfrac{\mathrm{Re}_c}{\mathrm{Re}}}\right)\frac{1-\varepsilon}{(1-\varepsilon^{1/3})^3}\left[\frac{P_1+\bar{\mu}P_2}{P_3+\bar{\mu}P_4}\right]G(\chi)\\
&\text{with :}\\
&\bar{\mu} = \mu_g/\mu_l\\
&P_1 = 4 + 6\varepsilon^{5/3}\\
&P_2 = 6 - 6\varepsilon^{5/3}\\
&P_3 = 4 + 6\varepsilon^{1/3} + 6\varepsilon^{2/3} + \varepsilon\\
&P_4 = 4 + 3\varepsilon^{1/3} - 3\varepsilon^{2/3} - 4\varepsilon\\
&\mathrm{Re}_c = 33 + 8600\varepsilon^{2/3}\\
&G(\chi) = \tfrac{1}{3}\chi^{4/3}(\chi^2-1)^{3/2}\frac{\sqrt{\chi^2-1} - (2-\chi^2)\sec^{-1}\chi}{(\chi^2\sec^{-1}\chi - \sqrt{\chi^2-1})^2}
\end{aligned} \tag{4.21}$$

The oblateness χ of the bubble is calculated with a terminal velocity correlation by Kushch

et al. (2002) (first-order term only):

$$\chi = 1 + \frac{9}{64}\,We \tag{4.22}$$

where the Weber number We is defined as:

$$We = \frac{2a\rho_l u_b^2}{\sigma} \tag{4.23}$$

The relation of Eq. (4.22) is valid for a single bubble rising in stagnant liquid, so its application is questionable in our case. For instance, oblateness tends to increase with void fraction (Duineveld, 1995; Roig and Larue de Tournemine, 2007). However, our observations show that bubbles change shape depending on structure position, and so that velocity is the major parameter controlling the bubble deformations.

$\vec{F}_M$ is the added mass force:

$$\vec{F}_M = -\frac{4}{3}\pi a^3 \rho_l C_M \frac{d\vec{u}_b}{dt} \tag{4.24}$$

where C_M is the added mass coefficient. A few studies propose the effect of void fraction on the added mass of a bubble. See for instance the works by Zuber (1964) or Cai and Wallis (1994). However, added mass could increase or decrease with ε depending on certain hypotheses. A more recent study by Béguin *et al.* (2014) proposes a new semi-empirical correlation based on potential flow theory for random clouds of bubbles. It appears that C_M weakly increases with ε. Therefore, we will simply use the added mass coefficient $C_M = 0.5$ of an isolated sphere as a first approximation.

Finally, the bubble undergoes an inertia force $\vec{F}_I$ because of the pressure gradient caused by the accelerating tube on the water, in the transverse direction. This force can be expressed as:

$$\vec{F}_I = \frac{4}{3}\pi a^3 \rho_l \ddot{\vec{y}}_s \tag{4.25}$$

To sum up, the only input parameters for the model are a, j and β. The motion of the bubble is governed by its added mass and fluid viscosity. Thus, it has no mass nor rigidity, as modeled by Hara and Kohgo (1985).

4.7.2 Transverse amplitude

A few images of the oscillating structure at different instants were segmented in order to have an estimate of the bubble sizes and shapes, for $Y_s/D_h = 0.22$. The bubble radii

a were found to range within [1.2, 2] mm and oblateness χ within [1.2, 1.9], assuming a revolution ellipsoid. For the same conditions and $a = 1.4$, the model predicts χ up to 2.3, which seems reasonable considering the fact that the correlation we use do not take the effect of acceleration into account.

The predicted bubble relative amplitude $Y_{b|s}$ is presented on Fig. 4.17(a). The model tends to over-predict the amplitude by a factor 2. Thus, some effects have obviously been overlooked. Still, the trend seems very well respected. The limit cycle reached is mostly due

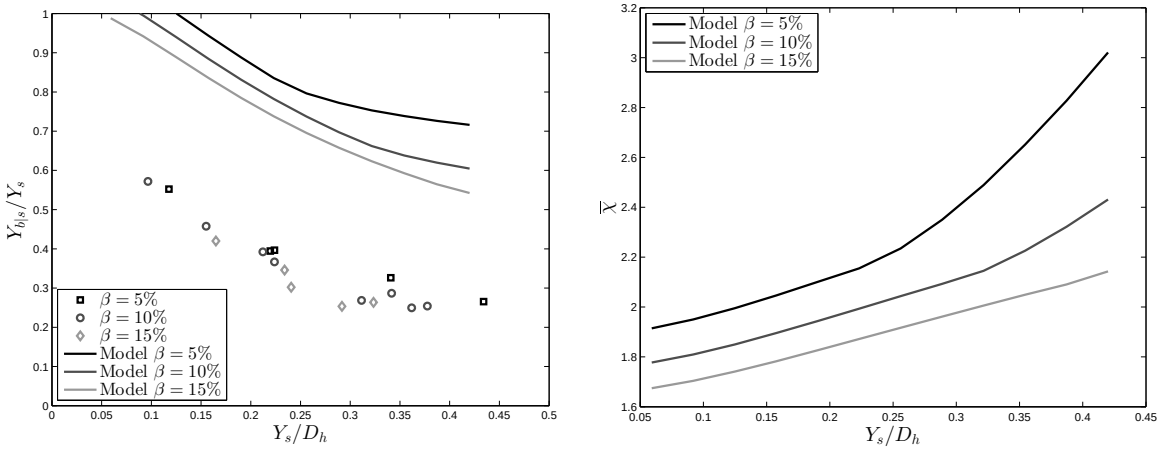

(a) Comparison between model and experimental values for gas phase transverse amplitude.

(b) Mean oblateness

Figure 4.17 Analytical model results.

to the oblateness of the bubbles, as attested by Fig. 4.17(b).

4.7.3 Dissipated energy

It is also useful to compare the model directly to the damping values measured for bubbly flow. We decided to compare the energy dissipated over one cycle of oscillation:

$$E_{2\varphi} = \int_0^{2\pi/\omega} F_{2\varphi} \frac{\mathrm{d}y_s}{\mathrm{d}t} \mathrm{d}t = \int_0^{2\pi/\omega} c_{2\varphi} {\dot{y}_s}^2 \mathrm{d}t = \pi c_{2\varphi} \omega Y_s^2 \tag{4.26}$$

where T is the oscillation period. This energy has to be compared with that dissipated by the work of the forces applied on the bubbles. We are only interested in the projection in the $\vec{y}$ direction of these forces since we try to explain two-phase damping with transverse motion of bubbles. The buoyancy force is vertical and as such is not accounted for. Added mass and inertia forces are purely inertial, hence they do not work over one cycle. Only the power of

the drag force is contributing, and can be written as:

$$W_D = N_b \int_0^{2\pi/\omega} \overrightarrow{F_D} \cdot \vec{y} \frac{\mathrm{d}y_{b|s}}{\mathrm{d}t} \mathrm{d}t \tag{4.27}$$

$\overrightarrow{F_D} \cdot \vec{y}$ is the projection of the drag force in the y-direction. N_b stands for the number of bubbles in the test section. It is calculated based on the void fraction:

$$N_b = \frac{\varepsilon AL}{\frac{4}{3}\pi a^3} \tag{4.28}$$

This equation is valid only for bubbly flow (up to $\beta \approx 50\%$ experimentally), so no effect of coalescence is considered. The void fraction depends on volumetric fraction and slip ratio (previously defined in the z direction). Comparison between the model and experiments is shown on Fig. 4.18.

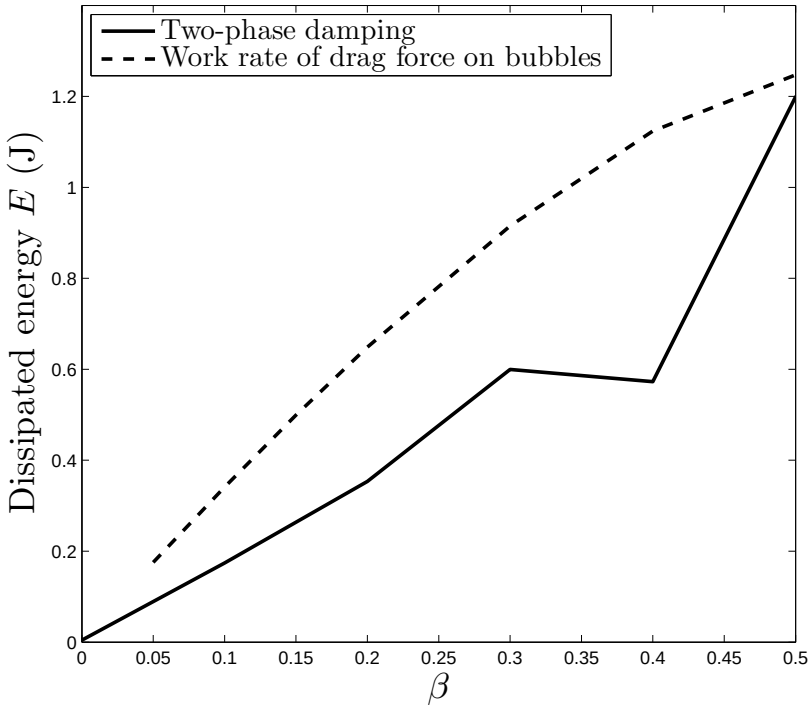

Figure 4.18 Energy dissipated over one oscillation cycle. – : by two-phase damping; - - : calculated with analytical model. Only the work rate of bubble drag forces is significant in the model. Calculations are presented for structure amplitude $Y_s = 18.8$ mm, superficial velocity $j = 0.6$ m/s and bubble radius $a = 1.4$ mm.

The model compares fairly well with two-phase damping in terms of dissipated energy. It is odd to have a good agreement for the work rate, and a poor one for relative amplitude.

Assuming that the drag relation is correct, we believe this is due to the fact that we measured relative amplitude of the gas phase with respect to the structure, and not the liquid, as underlined in the next section.

4.7.4 Model calibration with glycerin experiments

Changing the Reynolds number is a good way to test the validity of the model for other flow conditions. Other videos were taken with a stagnant glycerin solution ($j = 0$). Glycerin density is 1.21. Its viscosity was tested with a rheometer and was found to be of 0.163 Pa.s at 22°C. Single bubbles were injected with a needle. The Reynolds numbers based on bubble relative velocities were below 3. Using segmentation imaging techniques, we were able to measure bubble radii, transverse amplitude and vertical terminal velocity (cf. Fig. 4.19(a) and Fig. 4.19(b)).

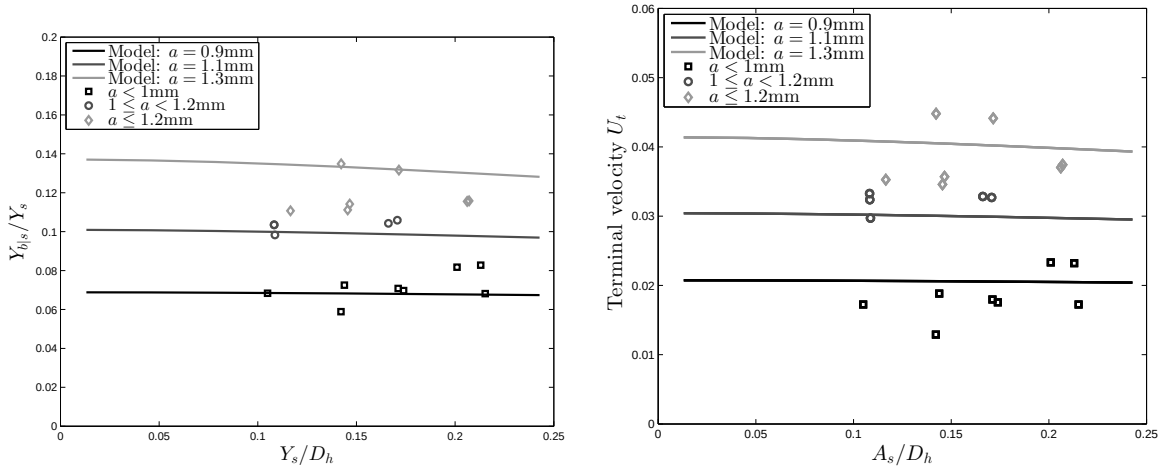

(a) Transverse amplitude.

(b) Terminal velocity.

Figure 4.19 Comparison between model and experiments with single bubbles rising in stagnant glycerin.

The scatter in the data is explained by the fact that we do not control the bubble radius. This is why the points were gathered in several radius categories, thus collapsing the data. The structural transverse amplitude does not have a strong effect on $Y_{b|s}$. Given the low Weber numbers of the experiments, the bubbles hardly deform ($\chi \approx 1$). Hence, no additional drag is induced. Also note that the graphs are basically identical on their respective scale. Experimentally, the bubbles would rise in glycerin in a straight line due to the very low Reynolds number (two path instabilities occur at higher Re, as reported extensively in the literature, *e.g.* Tomiyama *et al.* (2002) and Mougin and Magnaudet (2001). Hence, at this range of Re, transverse migration is only due to tube motion and depends directly on

bubble radius, as attested by Fig. 4.20. The figure summarizes the twenty-five experiments in stagnant glycerin and confirms that no coupling exists between the y and z directions.

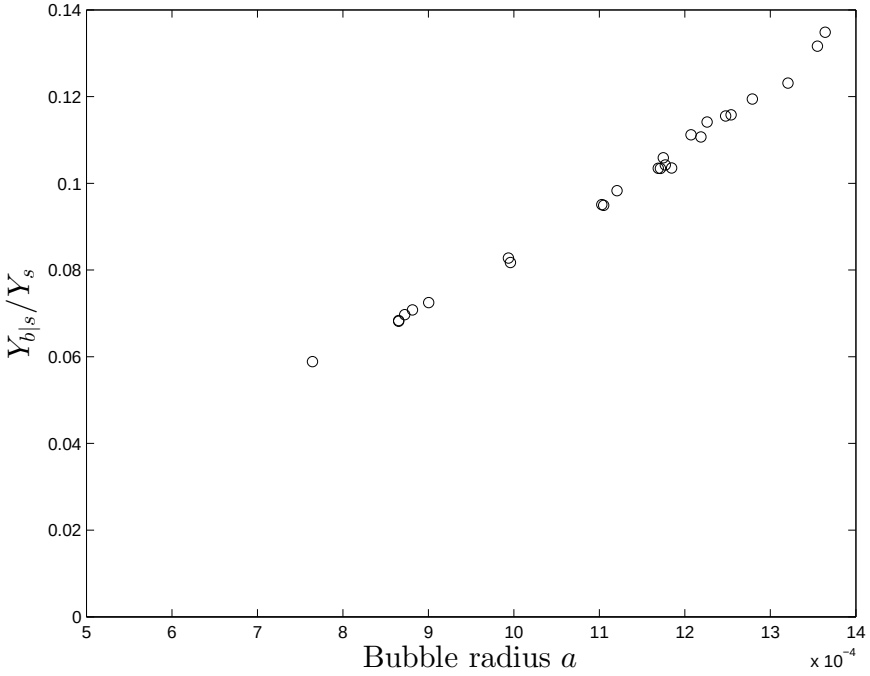

Figure 4.20 Gain of the bubbles as a function of bubble radius, in stagnant glycerin (experimental).

Contrary to Sec. 4.7.2, the agreement between the model and experiments on Fig. 4.19 is very good, for both U_t and $Y_{b|s}$. This suggests that considering the relative amplitude with respect to the structure or the liquid is the same. Hence, assuming solid body motion for the liquid is correct in this case. The poor agreement reported before for air-water mixture experiments may be caused by a recirculation of water around bubbles or a wrong drag coefficient given the bubbles' high Reynolds number. Indeed, the higher the void fraction, the more important the recirculation to fill the space between the moving bubbles. This interstitial flow would affect both drag on bubbles and relative velocity.

Furthermore, we stated in Sec. 4.6.2 that structural oscillation did not seem to onset bubble coalescence. The nature of the liquid film between bubbles would control their coalescence/break-up conditions (Razzaque *et al.*, 2003). The local gas-liquid interaction due to the relative bubble motion is given by pseudo-turbulence theory but is beyond the scope of this study. Bubble-induced liquid agitation was modeled (*e.g.* Elghobashi and Abou-Arab, 1983; Béguin, 2010) and characterized experimentally at moderate void fractions (Lance and Bataille, 1991; Riboux *et al.*, 2010). Information on local interstitial velocity in an oscillating structure with gas bubbles would allow to model turbulence forces on bubbles as well as lift

forces (through information on local vorticity) which were neglected in the present model. This effect is important even for two-phase flow in tubes at rest for void fractions larger than 2% (Roig and Larue de Tournemine, 2007). Thus, it is likely that structural oscillations cause additional pseudo-turbulence when inducing the relative motion of the gas phase. Characterizing this phenomenon might help to understand the two-phase damping mechanism more thoroughly.

4.8 Conclusion

In this paper, a new test section offering control over the excitation parameters in order to determine two-phase damping experimentally was presented. Observations as well as processing of high-speed videos gave novel information on the gas phase motion, especially on its relative motion with respect to the structure. A simple analytical model fed with correlations was derived. Although not entirely complete, the model gives useful information on the physical dissipative mechanism. It also underlines the missing information to catch the full nature of the phenomenon. We suspect that the latter lies in the complexity of the liquid phase motion. So far, the following conclusions and perspectives can be brought out:

(i) Two-phase damping can reach 3% in this square 76.2 mm tube. It is fairly proportional to volumetric fraction, until a change in slope at transition between bubbly and churn flow regime occurs.

(ii) The frequency response function of the tube subjected to internal two-phase flow confirms that two-phase damping is a viscous damping (velocity dependent) mechanism. This is supported by the fact that $\zeta_{2\varphi}$ seems independent of the excitation force magnitude F_0 for bubbly flow. For higher void fraction, the mechanism is different. We suspect that energy is extracted by sloshed liquid phase within the continuous gas phase. Damping is affected by the stochastic nature of the flow at this regime, causing an increase of standard deviation in the results.

(iii) There is definite relative motion of the gas phase with respect to the liquid for bubbly flow. The bubbles have a bulk body motion due to the tube oscillations, and are in phase lead with respect to the structure. The oscillations seem combined with a swirling motion. It is not very dissipative but helps to prevent a premature coalescence of the bubbles, keeping a maximum interface surface area prompt to transfer energy between the phases and the structure.

(iv) For bubbly flow, the power disspated by two-phase damping is equivalent to that dissipated by the drag forces on the bubbles. However, the discrepancy between bubble amplitudes predicted by the model and those measured suggests a complex interstitial

liquid flow between the bubbles under tube oscillations, affecting both drag and relative velocity. It seems like even though two-phase damping is observed on a large scale, small scale effects cannot be overlooked for $\zeta_{2\varphi}$ to be accurately modeled.

Acknowledgments

This work was sponsored by the Natural Sciences and Engineering Research Council, Babcock & Wilcox Canada and Atomic Energy of Canada Ltd., through the BWC/AECL/NSERC research chair in fluid-structure interactions.

References

AU-YANG, M. K., CHEN, S. S., PAÏDOUSSIS, M. P., PETTIGREW, M. J., WEAVER, D. S. and ZIADA, S. (2000). Flow-induced vibrations in power and process plant components - progress and prospects. *Journal of Pressure Vessel Technology*, 122, 339–348.

BÉGUIN, C. (2010). *Modélisation des écoulements diphasiques: amortissement, forces interfaciales et turbulence diphasique.* PhD thesis, École Polytechnique de Montréal.

BÉGUIN, C., ANSCUTTER, F., ROSS, A., PETTIGREW, M. J. and MUREITHI, N. W. (2009a). Two-phase damping and interface surface area in tubes with vertical internal flow. *Journal of Fluids and Structures*, 25, 178–204.

BÉGUIN, C., PELLETIER, E. and ÉTIENNE, S. (2014). Void fraction effect on added mass in bubbly flow. *ASME 2014 Pressure Vessels and Piping Conference*. American Society of Mechanical Engineers.

BÉGUIN, C., WEHBE, J., ROSS, A., PETTIGREW, M. J. and MUREITHI, N. W. (2009b). Influence of viscosity, density and surface tension on two-phase damping. *ASME 2009 Pressure Vessels and Piping Conference*. American Society of Mechanical Engineers, 247–257.

CAI, X. and WALLIS, G. B. (1994). A more general cell model for added mass in two-phase flow. *Chemical engineering science*, 49, 1631–1638.

CARLUCCI, L. N. (1980). Damping and hydrodynamic mass of a cylinder in simulated two-phase flow. *Journal of Mechanical Design*, 102, 597–602.

CARLUCCI, L. N. and BROWN, J. D. (1983). Experimental studies of damping and hydrodynamic mass of a cylinder in confined two-phase flow. *Journal of Vibration Acoustics Stress and Reliability in Design*, 105, 83.

CHENG, L., RIBATSKI, G. and THOME, J. R. (2008). Two-phase flow patterns and flow-pattern maps: fundamentals and applications. *Applied Mechanics Reviews*, 61, 050802.

COLEMAN, J. W. and GARIMELLA, S. (1999). Characterization of two-phase flow patterns in small diameter round and rectangular tubes. *International Journal of Heat and Mass Transfer*, 42, 2869–2881.

COLLIER, J. G. and THOME, J. R. (1994). *Convective boiling and condensation.* Oxford University Press.

DEN HARTOG, J. P. (1956). *Mechanical vibrations.* Dover Publications.

DUINEVELD, P. C. (1995). The rise velocity and shape of bubbles in pure water at high reynolds number. *Journal of Fluid Mechanics*, 292, 325–332.

ELGHOBASHI, S. E. and ABOU-ARAB, T. W. (1983). A two-equation turbulence model for two-phase flows. *Physics of Fluids (1958-1988)*, 26, 931–938.

GRAVELLE, A., ROSS, A., PETTIGREW, M. J. and MUREITHI, N. W. (2007). Damping of tubes due to internal two-phase flow. *Journal of Fluids and Structures*, 23, 447 – 462.

HARA, F. and KOHGO, O. (1985). Analytical model for evaluating added mass and damping of a vibrating circular rod in two-phase fluid. *Transactions of the 8. international conference on structural mechanics in reactor technology. Vol. F1 and F2.*

ISHII, M. and ZUBER, N. (1979). Drag coefficient and relative velocity in bubbly, droplet or particulate flows. *AIChE Journal*, 25, 843–855.

KUSHCH, V. I., SANGANI, A. S., SPELT, P. D. M. and KOCH, D. L. (2002). Finite-weber-number motion of bubbles through a nearly inviscid liquid. *Journal of Fluid Mechanics*, 460, 241–280.

LANCE, M. and BATAILLE, J. (1991). Turbulence in the liquid phase of a uniform bubbly air–water flow. *Journal of Fluid Mechanics*, 222, 95–118.

LINDKEN, R. and MERZKIRCH, W. (2002). A novel PIV technique for measurements in multiphase flows and its application to two-phase bubbly flows. *Experiments in fluids*, 33, 814–825.

MANDHANE, J. M., GREGORY, G. A. and AZIZ, K. (1974). A flow pattern map for gas—liquid flow in horizontal pipes. *International Journal of Multiphase Flow*, 1, 537–553.

MOUGIN, G. and MAGNAUDET, J. (2001). Path instability of a rising bubble. *Physical review letters*, 88, 014502.

OHNUKI, A. and AKIMOTO, H. (2000). Experimental study on transition of flow pattern and phase distribution in upward air–water two-phase flow along a large vertical pipe. *International journal of multiphase flow*, 26, 367–386.

OLSSON, H., ÅSTRÖM, K., DE WIT, C. C., GÄFVERT, M. and LISCHINSKY, P. (1998). Friction models and friction compensation. *European Journal of Control*, 4, 176 – 195.

PETTIGREW, M. J. and KNOWLES, G. D. (1997). Some aspects of heat-exchanger tube damping in two-phase mixtures. *Journal of fluids and structures*, 11, 929–945.

PETTIGREW, M. J. and TAYLOR, C. E. (1991). Fluidelastic instability of heat exchanger tube bundles; review and design recommendations. *Journal of Pressure Vessel Technology*, 113, 242–256.

PETTIGREW, M. J. and TAYLOR, C. E. (2004). Damping of heat exchanger tubes in two-phase flow: review and design guidelines. *Journal of pressure vessel technology*, 126, 523–533.

PRASSER, H.-M., BEYER, M., BÖTTGER, A., CARL, H., LUCAS, D., SCHAFFRATH, A., SCHUTZ, P., WEISS, F.-P. and ZSCHAU, J. (2005). Influence of the pipe diameter on the structure of the gas-liquid interface in a vertical two-phase pipe flow. *Nuclear technology*, 152, 3–22.

RAZZAQUE, M. M., AFACAN, A., LIU, S., NANDAKUMAR, K., MASLIYAH, J. H. and SANDERS, R. S. (2003). Bubble size in coalescence dominant regime of turbulent air–water flow through horizontal pipes. *International journal of multiphase flow*, 29, 1451–1471.

RIBOUX, G., RISSO, F. and LEGENDRE, D. (2010). Experimental characterization of the agitation generated by bubbles rising at high reynolds number. *Journal of Fluid Mechanics*, 643, 509–539.

ROIG, V. and LARUE DE TOURNEMINE, A. (2007). Measurement of interstitial velocity of homogeneous bubbly flows at low to moderate void fraction. *Journal of Fluid Mechanics*, 572, 87–110.

TAITEL, Y. and DUKLER, A. E. (1976). A model for predicting flow regime transitions in horizontal and near horizontal gas-liquid flow. *AIChE Journal*, 22, 47–55.

TOMIYAMA, A., CELATA, G. P., HOSOKAWA, S. and YOSHIDA, S. (2002). Terminal velocity of single bubbles in surface tension force dominant regime. *International Journal of Multiphase Flow*, 28, 1497–1519.

UCHIYAMA, T. (2003). Numerical prediction of added mass and damping for a cylinder oscillating in confined incompressible gas–liquid two-phase mixture. *Nuclear engineering and design*, 222, 68–78.

VAN BEEK, A. (2006). *Advanced engineering design: lifetime performance and reliability*, vol. 1.

WEAVER, D. S. and FITZPATRICK, J. A. (1988). A review of cross-flow induced vibrations in heat exchanger tube arrays. *Journal of Fluids and Structures*, 2, 73 – 93.

ZUBER, N. (1964). On the dispersed two-phase flow in the laminar flow regime. *Chemical Engineering Science*, 19, 897–917.

ZUBER, N. and HENCH, J. (1962). Steady state and transient void fraction of bubbling systems and their operating limits (part i, steady state operation). *General Electric Report 62GL100*.

CHAPITRE 5

DISCUSSION GÉNÉRALE

5.1 Expériences avec d'autres fluides

À la fin de l'article précédent, on propose un modèle simple fondé sur des corrélations qui, sans prétendre capturer précisément le mécanisme en jeu, permet de donner des ordres de grandeur. Il apparaît que le modèle prédit des valeurs convenables pour l'amortissement mais surestime l'amplitude des bulles. Cette erreur a été attribuée au fait que l'on considère un mouvement de corps solide de la phase liquide avec le mouvement du tube.

Il a donc été tenté de renouveler les expériences avec un écoulement diphasique air-glycérine. Elles auraient pour but d'une part de confirmer les résultats de Béguin qui montrent que $\zeta_{2\varphi}$ est indépendant de la viscosité pour l'écoulement à bulles, et d'autre part de mesurer l'amplitude de la phase gazeuse. La confrontation avec le modèle apporterait d'autres informations sur l'importance de la circulation interstitielle de la phase liquide. Malheureusement, les pertes de charge associées à l'écoulement extrêmement visqueux ont mis à rude épreuve les raccords de la section d'essais (section carrée vers circulaire), la colle n'adhérant pas bien sur le PVC usiné. Il est donc nécessaire de concevoir de nouveaux fittings filetés pour résister à la pression du fluide. Aussi, la vitesse du mélange devra être suffisamment faible pour éviter le flambement des tuyaux flexibles qui a été constaté à partir d'environ 0.1 m/s. Les tuyaux flexibles pourront éventuellement être raccourcis. Ce phénomène n'a pas été observé avec de l'eau même à des vitesses plus élevées. Il est donc surprenant qu'il apparaisse en glycérine étant donné que cette instabilité statique ne dépend que du nombre de Cauchy $Ca = \rho U^2/K$ où K est le module d'élasticité du tube, et que les densités de l'eau et de la glycérine sont semblables (de Langre, 2002).

5.2 Mouvement des bulles en liquide stagnant

En attendant, l'étude d'une bulle en élévation dans de la glycérine stagnante, sous oscillations du tube a été effectuée. À un régime ne dépassant pas $Re = 3$ ($\approx$ écoulement de Stokes), les bulles ont une une déformation de moins de 1% et une trajectoire parfaitement rectiligne à laquelle s'ajoute le mouvement transverse. Ceci est dû au fait que la bulle ne peut ressentir aucune force de portance pour un écoulement de Stokes (Bretherton, 1962). L'étude a permis de confirmer la validité du modèle à bas taux de vide et Reynolds, et justifie aussi l'hypothèse du mouvement de corps solide de la phase liquide pour une seule bulle. Le lecteur

pourra se demander avec raison pourquoi l'expérience n'a pas été réalisée avec de l'eau, et ainsi valider le modèle à taux de vide nul et Reynolds équivalent.

Nous avons vu qu'une bulle en eau stagnante (faible viscosité) adopte deux instabilités, en zigzag ou hélicoïdale (cf. Fig 5.1), en fonction du nombre de Reynolds et de la déformation initiale (Pelletier *et al.*, 2014). Ces instabilités sont liées aux décrochements alternatifs de vortex dans le sillage de la bulle. Les sillons créent des dépressions autour de la bulle, générant une force de portance (perpendiculaire à la vitesse relative de la bulle) oscillante (Mougin et Magnaudet, 2001).

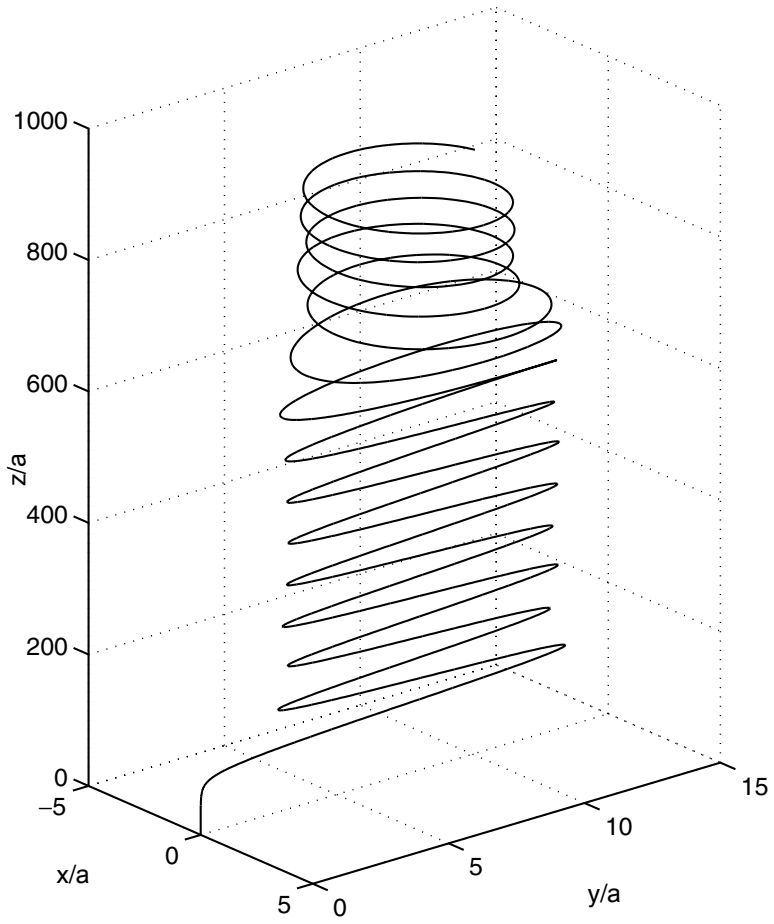

Figure 5.1 Oscillations naturelles d'une bulle millimétrique dans de l'eau stagnante. Après une courte élévation en ligne droite, la bulle adopte un mouvement de zigzag. Après un certain temps, un mouvement de spirale est amorcé (Mougin et Magnaudet, 2001).

Puisque l'on ne mesure son mouvement que dans un plan, on ne mesurerait donc que la projection de mouvement (la bulle ne va pas nécessairement osciller dans un plan parallèle à la fenêtre du tube). En guise de simplification, considérons donc un mouvement de zigzag

dans le plan d'étude.

La Fig. 5.2 montre la position relative en y et vitesse en z, pour une bulle millimétrique s'élevant dans de l'eau stagnante, en fonction du temps. Lors de la phase 1, le tube est

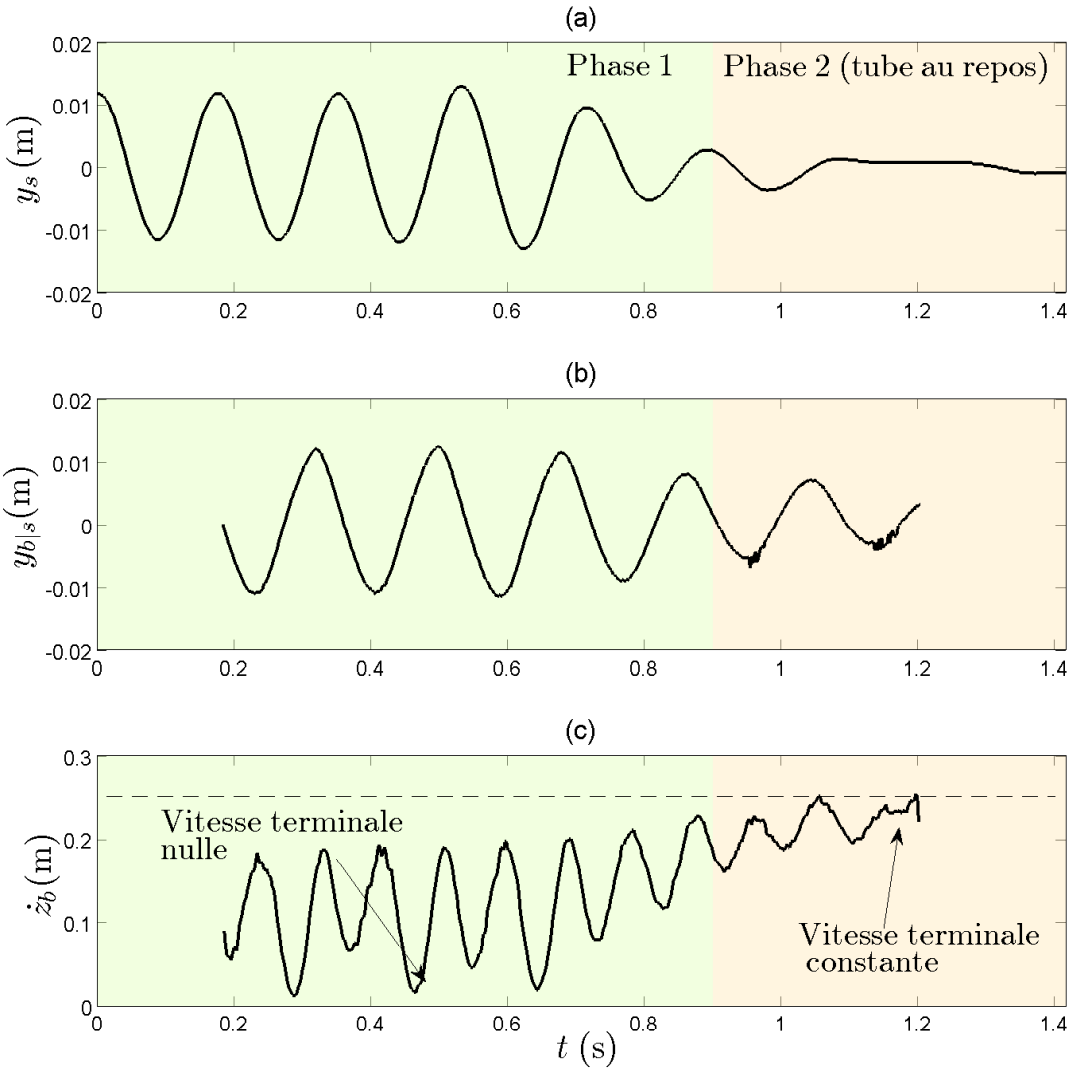

Figure 5.2 Effet des oscillations forcées suivi de l'arrêt du tube sur l'oscillation relative $y_{b|s}$ de la bulle s'élevant dans de l'eau stagnante, et sa vitesse verticale en z. (a) : Position transverse du tube ; (b) : Position transverse relative de la bulle ; (c) Vitesse ascensionnelle de la bulle. Fréquence d'excitation $f_s = 5.5$ Hz.

soumis à des oscillations forcées. Sans surprise, la bulle oscille de manière transverse, mais on remarque aussi que la vitesse en z varie périodiquement, en passant quasiment par 0. Lors de la phase 2, on arrête brusquement le mouvement du tube (on revient à des conditions

de liquide stagnant). Les oscillations liées à l'instabilité de la bulle subsistent, alors que la vitesse terminale se stabilise et atteint le 0.25 m/s attendu pour une bulle millimétrique en eau stagnante.

Ce comportement de la vitesse verticale est lié à la force de portance agissant sur la bulle. Lors de la phase 2, elle est purement dirigée selon y. En revanche, en présence du mouvement de la phase liquide, la force de portance a une composante négative selon z, et qui s'oppose à la flottaison. Ceci est dû au fait que la force de portance sur un objet est perpendiculaire à sa vitesse relative par rapport au fluide. La modélisation de la force de portance dans un liquide stagnant est extrêmement complexe. Cependant, la nature des autres forces (masse ajoutée et traînée) est bien connue. Partant de ce constat, Shew *et al.* (2006) font une mesure a posteriori de la force de portance sur une bulle. À partir du mouvement des bulles en 3D, ils en déduisent la portance dans l'équation du mouvement. Sa magnitude peut atteindre 20 μN pour une bulle de 1.12 mm, alors que la flottaison est de l'ordre de 0.5 μN donc il est possible que la projection de la portance soit responsable de l'arrêt vertical de la bulle. Cet effet n'est pas observé pour des taux de vide entre 3 et 11%, étant donné que les bulles en aval ont tendance à stabiliser les sillages de celles en amont, et que les bulles voisines empêchent sans doute une oscillation. Toujours est-il que ce phénomène complique l'étude de l'effet des oscillations forcées sur une bulle en eau stagnante.

Il convient aussi de noter sur la Fig. 5.2(b) que la fréquence d'oscillation propre à la bulle diffère peu de la fréquence d'excitation (5.5 Hz). En effet, Shew *et al.* (2006) ont mesuré des fréquences variant de 4.3 à 5.5 Hz pour des bulles millimétriques.

5.3 Mécanisme d'amortissement diphasique

Au vu de l'indépendance de l'amortissement diphasique vis-à-vis de la différence de viscosité entre les phases, Béguin (2010) en conclut que le mécanisme de dissipation est purement inertiel. Cependant, pour un mouvement harmonique, une force inertielle ne travaille pas sur un cycle, car la force est alors en quadrature de phase avec la vitesse. À partir du traitement vidéo et du modèle de forces sur la bulle, nous avons pu prouver que le travail des forces de traînée sur les bulles jouait un rôle majeur dans le mécanisme d'amortissement. Cependant, les forces de traînée dépendent directement du nombre de Reynolds et de la viscosité. La question que l'on est en droit de se poser est : comment l'amortissement diphasique peut-il être indépendant de la viscosité tout en étant causé par la force de traînée sur les bulles ?

On rappelle l'expression de la puissance dissipée par les bulles :

$$W_D = N_b \int_0^{2\pi/\omega} \overrightarrow{F_D} \cdot \vec{y} \frac{\mathrm{d}y_{b|s}}{\mathrm{d}t} \mathrm{d}t \tag{5.1}$$

Bien qu'en augmentant la viscosité, la force F_D a tendance à augmenter, l'amplitude du mouvement $y_{b|s}$ va quant à elle diminuer. Il est donc plausible que l'intégrale des deux reste relativement constant. Avec notre modèle, multiplier la viscosité du liquide par 10 cause une énergie divisée par 2. La sensibilité est relativement faible mais pas suffisamment pour expliquer une indépendance de l'amortissement vis-à-vis de la viscosité. Comme mentionné précédemment, le traitement de vidéos d'écoulements diphasiques avec d'autre fluides et l'amélioration du modèle aideraient à élucider ce point.

CHAPITRE 6

CONCLUSION ET RECOMMANDATIONS

Au cours de ces travaux, nous avons abordé le thème des vibrations dans les échangeurs de chaleur. L'accent a été porté sur l'instabilité fluidélastique, phénomène qui donne encore du fil à retordre à la recherche. Les principaux mécanismes d'instabilité ont été présentés, de même que plusieurs modèles théoriques. Le modèle quasi-stationnaire a été sélectionné car c'est un modèle linéaire et viable. Il permet d'identifier les paramètres cruciaux qui contrôlent l'IFE. Nous avons retenu la dérivée du coefficient de portance et l'amortissement diphasique.

6.1 Synthèse des travaux

Lors des travaux sur le coefficient de portance, nous avons :

- mesuré la dérivée du coefficient de portance à nombre de Reynolds modéré. Les résultats ont été corroborées par des simulations numériques DNS réalisées par les autres auteurs de l'article. Un Reynolds critique pour lequel la dérivée $C_{L,y}$ s'annule a été trouvé expérimentalement mais pas numériquement.
- adapté un code fondé sur la théorie des écoulements potentiels pour calculer la force de portance sur un cylindre. L'influence de paramètres géométriques tels que l'angle du faisceau et le *pitch* mettent en perspective la dispersion des résultats trouvés dans la littérature. Pour notre configuration triangulaire tournée avec $P/D = 1.5$, le code confirme la tendance asymptotique de $C_{L,y}$. Nous avons donc proposé une interpolation des résultats en fonction du nombre de Reynolds.
- étudié la stabilité d'un cylindre flexible avec le modèle quasi-stationnaire. L'influence du nombre de Reynolds a été discutée. Les limites du modèle ainsi que l'incertitude liée à la modélisation du paramètre de retard ont été dégagées.

En ce qui concerne l'amortissement diphasique, nous avons :

- Mesuré l'amortissement diphasique pour différentes vitesses du mélange et taux de vide dans un tube carré de 76.2 mm. Il peut atteindre environ 4%. Il est donc considérablement plus important que les amortissements structural et dû et à la viscosité de l'eau qui ne dépassent pas 1% chacun. Les courbes d'amortissement ont été corroborées à la transition d'écoulement entre écoulements à bulles et agité au moyen de photographies de la section d'essai.

- Étudié l'influence des paramètres d'excitation tels que la fréquence ou la force d'excitation. Cela a permis de prouver que le mécanisme dissipatif est purement visqueux (proportionnel à la vitesse), même à des fréquences si basses et des amplitudes du mouvement si élevées. Ce fait peut aider à la modélisation d'interactions fluide-structure faisant intervenir les écoulements diphasiques.
- Observé et quantifié le mouvement relatif de la phase gazeuse au moyen de vidéos acquises avec une caméra ultra-rapide. Les oscillations de la structure causent des oscillations de bulles en avance de phase, ainsi qu'une montée en spirale des bulles. Ce dernier mécanisme, non dissipatif étant donné les faibles vitesses de spirales, est la conséquence du fait qu'à l'approche d'un mur, les bulles vont avoir tendance à s'écraser et "glisser" dans une direction préférentielle. On aurait pu s'attendre à ce qu'elles rebondissent contre le mur, augmentant les chances de coalescence avec d'autre bulles. Ceci pourrait expliquer pourquoi l'amortissement diphasique reste relativement linéaire en fonction du taux de vide, même avec des amplitudes du tube relativement grandes. La transition d'écoulement ne semble pas affectée par l'excitation du tube.
- Proposé un modèle simple du mécanisme d'amortissement diphasique, fondé sur des corrélations tenant compte du taux de vide. Il a permis de prouver que les forces de traînée des bulles jouaient un rôle prédominant dans le mécanisme de dissipation. Cependant, le modèle sur-prédit les valeurs d'amplitude relative de la bulle par un facteur 2. Il est difficile à l'heure actuelle d'en conclure sur la cause de cet écart compte tenu des hauts nombre de Reynolds de la bulle. Il pourrait tout aussi bien être dû à l'influence de la recirculation d'eau autour des bulles soit la pseudo-turbulence, qu'à la validité de la relation du coefficient de traînée.

6.2 Améliorations futures

- Déterminer la dérivée de la portance d'un cylindre sur un code 3D commercial, afin d'atteindre le Reynolds critique pour lequel elle s'annule. On pourra aussi confirmer la tendance établie pour la configuration triangulaire tournée.
- Améliorer le traitement des vidéos afin de capturer plus d'information sur le mouvement des bulles. Aussi, l'utilisation de sondes optiques pourraient donner des informations intéressantes sur la répartition locale du taux de vide sous oscillations du tube.
- Nourrir le modèle d'amortissement diphasique avec de nouvelles corrélations plus pertinentes (le cas échéant), notamment une relation pour l'aplatissement de la bulle qui tiendrait compte de l'accélération.
- Tenir compte de la distribution des diamètres des bulles à partir d'images de l'écoule-

ment à différentes positions.

- Effectuer des mesures de l'amplitude du mouvement de la phase gazeuse avec d'autres fluides.
- Augmenter la capacité de la pompe pour atteindre des vitesses de mélange plus importantes.
- Changer les ressorts de compression du tube pour baisser la fréquence naturelle du système (à 1 ou 2 Hz) et voir la conséquence sur l'amplitude du mouvement des bulles et les valeurs d'amortissement.

RÉFÉRENCES

AU-YANG, M. K., CHEN, S. S., PAÏDOUSSIS, M. P., PETTIGREW, M. J., WEAVER, D. S. et ZIADA, S. (2000). Flow-induced vibrations in power and process plant components - progress and prospects. *Journal of Pressure Vessel Technology*, 122, 339–348.

AUSTERMANN, R. et POPP, K. (1995). Stability behaviour of a single flexible cylinder in rigid tube arrays of different geometry subjected to cross-flow. *Journal of Fluids and Structures*, 9, 303–322.

BÉGUIN, C. (2010). *Modélisation des écoulements diphasiques : amortissement, forces interfaciales et turbulence diphasique.* Thèse de doctorat, École Polytechnique de Montréal.

BÉGUIN, C., ANSCUTTER, F., ROSS, A., PETTIGREW, M. J. et MUREITHI, N. W. (2009a). Two-phase damping and interface surface area in tubes with vertical internal flow. *Journal of Fluids and Structures*, 25, 178–204.

BÉGUIN, C., PELLETIER, E. et ÉTIENNE, S. (2014). Void fraction effect on added mass in bubbly flow. *ASME 2014 Pressure Vessels and Piping Conference*. American Society of Mechanical Engineers.

BÉGUIN, C., WEHBE, J., ROSS, A., PETTIGREW, M. J. et MUREITHI, N. W. (2009b). Influence of viscosity, density and surface tension on two-phase damping. *ASME 2009 Pressure Vessels and Piping Conference*. American Society of Mechanical Engineers, 247–257.

BLEVINS, R. D. (1974). Fluidelastic whirling of a tube row. *Journal of Pressure Vessel Technology*, 96, 263–267.

BRETHERTON, F. P. (1962). The motion of rigid particles in a shear flow at low reynolds number. *Journal of Fluid Mechanics*, 14, 284–304.

CAI, X. et WALLIS, G. B. (1994). A more general cell model for added mass in two-phase flow. *Chemical engineering science*, 49, 1631–1638.

CARLUCCI, L. N. (1980). Damping and hydrodynamic mass of a cylinder in simulated two-phase flow. *Journal of Mechanical Design*, 102, 597–602.

CARLUCCI, L. N. et BROWN, J. D. (1983). Experimental studies of damping and hydrodynamic mass of a cylinder in confined two-phase flow. *Journal of Vibration Acoustics Stress and Reliability in Design*, 105, 83.

CHARRETON, C., BÉGUIN, C., YU, R. et ETIENNE, S. (2013). Stability derivatives in a parallel triangular tube bundle subject to cross-flow at moderated reynolds number. *ASME 2013 Pressure Vessels and Piping Conference*. American Society of Mechanical Engineers.

CHEN, S. S. (1983). Instability mechanisms and stability criteria of a group of circular cylinders subjected to cross-flow. Part i : theory. *Journal of Vibration, Acoustics, Stress, and Reliability in Design*, 105, 463–518.

CHEN, S. S. et SRIKANTIAH, G. S. (2001). Motion-dependent fluid force coefficients for tube arrays in crossflow. *Journal of pressure vessel technology*, 123, 429–436.

CHEN, S. S., WAMBSGANSS, M. W. et JENDRZEJCZYK, J. A. (1976). Added mass and damping of a vibrating rod in confined viscous fluids. *Journal of Applied Mechanics*, 43, 325–329.

CHENG, L., RIBATSKI, G. et THOME, J. R. (2008). Two-phase flow patterns and flow-pattern maps : fundamentals and applications. *Applied Mechanics Reviews*, 61, 050802.

COLEMAN, J. W. et GARIMELLA, S. (1999). Characterization of two-phase flow patterns in small diameter round and rectangular tubes. *International Journal of Heat and Mass Transfer*, 42, 2869–2881.

COLLIER, J. G. et THOME, J. R. (1994). *Convective boiling and condensation*. Oxford University Press.

CONNORS, H. J. (1970). Fluidelastic vibration of tube arrays excited by cross flow. *Flow induced vibration in Heat Exchangers*. New York : ASME, 42–56.

DE LANGRE, E. (2002). *Fluides et solides*. Editions Ecole Polytechnique.

DEN HARTOG, J. P. (1956). *Mechanical vibrations*. Dover Publications.

DUINEVELD, P. C. (1995). The rise velocity and shape of bubbles in pure water at high reynolds number. *Journal of Fluid Mechanics*, 292, 325–332.

ELGHOBASHI, S. E. et ABOU-ARAB, T. W. (1983). A two-equation turbulence model for two-phase flows. *Physics of Fluids (1958-1988)*, 26, 931–938.

ÉTIENNE, S. (1999). *Contribution à la Modélisation de l'Écoulement de Fluide Visqueux Autour de Faisceaux de Cylindres Circulaires*. Thèse de doctorat, École Supérieure de Mécanique de Marseille.

ÉTIENNE, S. et PELLETIER, D. (2011). Tube arrays flow-induced vibrations simulations with ale finite element method. *ASME 2011 Pressure Vessels and Piping Conference*. American Society of Mechanical Engineers, 329–336.

GILLEN, S. et MESKELL, C. (2009). Numerical analysis of fluidelastic instability in a normal triangular tube array. *ASME 2009 Pressure Vessels and Piping Conference*. American Society of Mechanical Engineers, 447–455.

GORMAN, D. J. (1978). Experimental development of design criteria to limit liquid cross-flow-induced vibration in nuclear reactor heat exchange equipment. *Nuclear Science and Technology*, 99, 324–336.

GRANGER, S. et PAÏDOUSSIS, M. P. (1996). An improvement to the quasi-steady model with application to cross-flow-induced vibration of tube arrays. *Journal of Fluid Mechanics*, 320, 163–184.

GRAVELLE, A., ROSS, A., PETTIGREW, M. J. et MUREITHI, N. W. (2007). Damping of tubes due to internal two-phase flow. *Journal of Fluids and Structures*, 23, 447 – 462.

HARA, F. et KOHGO, O. (1985). Analytical model for evaluating added mass and damping of a vibrating circular rod in two-phase fluid. *Transactions of the 8. international conference on structural mechanics in reactor technology. Vol. F1 and F2.*

ISHII, M. et ZUBER, N. (1979). Drag coefficient and relative velocity in bubbly, droplet or particulate flows. *AIChE Journal*, 25, 843–855.

KHALIFA, A., WEAVER, D. S. et ZIADA, S. (2012). A single flexible tube in a rigid array as a model for fluidelastic instability in tube bundles. *Journal of Fluids and Structures*, 34, 14–32.

KUSHCH, V. I., SANGANI, A. S., SPELT, P. D. M. et KOCH, D. L. (2002). Finite-weber-number motion of bubbles through a nearly inviscid liquid. *Journal of Fluid Mechanics*, 460, 241–280.

LANCE, M. et BATAILLE, J. (1991). Turbulence in the liquid phase of a uniform bubbly air–water flow. *Journal of Fluid Mechanics*, 222, 95–118.

LEVER, J. H. et WEAVER, D. S. (1982). A theoretical model for fluid-elastic instability in heat exchanger tube bundles. *Journal of Pressure Vessel Technology*, 104, 147–158.

LEVER, J. H. et WEAVER, D. S. (1986a). On the stability of heat exchanger tube bundles, part i : Modified theoretical model. *Journal of Sound and Vibration*, 107, 375–392.

LEVER, J. H. et WEAVER, D. S. (1986b). On the stability of heat exchanger tube bundles, part ii : Numerical results and comparison with experiments. *Journal of Sound and vibration*, 107, 393–410.

LINDKEN, R. et MERZKIRCH, W. (2002). A novel PIV technique for measurements in multiphase flows and its application to two-phase bubbly flows. *Experiments in fluids*, 33, 814–825.

LITTLE, J. (2003). *The Effect of Damping on Fluidelastic Instability in Heat Exchanger Tube Array.* Mémoire de maîtrise, McMaster University, Hamilton, Ontario, Canada.

MAHON, J. et MESKELL, C. (2009). Investigation of the underlying cause of the interaction between acoustic resonance and fluidelastic instability in normal triangular tube arrays. *Journal of Sound and Vibration*, 324, 91–106.

MAHON, J. et MESKELL, C. (2012). Surface pressure survey in a parallel triangular tube array. *Journal of Fluids and Structures*, 34, 123–137.

MANDHANE, J. M., GREGORY, G. A. et AZIZ, K. (1974). A flow pattern map for gas—liquid flow in horizontal pipes. *International Journal of Multiphase Flow*, 1, 537–553.

MESKELL, C. et FITZPATRICK, J. A. (2003). Investigation of the nonlinear behaviour of damping controlled fluidelastic instability in a normal triangular tube array. *Journal of Fluids and Structures*, 18, 573–593.

MOUGIN, G. et MAGNAUDET, J. (2001). Path instability of a rising bubble. *Physical review letters*, 88, 014502.

NOWLAN, I., ROSS, A. et PETTIGREW, M. J. (2009). Dynamic interaction between a straight tube and an anti-vibration bar. *ASME 2009 Pressure Vessels and Piping Conference*. American Society of Mechanical Engineers, 437–445.

OHNUKI, A. et AKIMOTO, H. (2000). Experimental study on transition of flow pattern and phase distribution in upward air–water two-phase flow along a large vertical pipe. *International journal of multiphase flow*, 26, 367–386.

OLSSON, H., ÅSTRÖM, K., DE WIT, C. C., GÄFVERT, M. et LISCHINSKY, P. (1998). Friction models and friction compensation. *European Journal of Control*, 4, 176 – 195.

PAÏDOUSSIS, M. P. (1980). Flow-induced vibrations in nuclear reactors and heat exchangers : practical experiences and state of knowledge. *Practical Experiences with Flow-Induced Vibrations*, 829, 1–81.

PAÏDOUSSIS, M. P. (1983). A review of flow-induced vibrations in reactors and reactor components. *Nuclear Engineering and Design*, 74, 31 – 60.

PAÏDOUSSIS, M. P. (2006). Real-life experiences with flow-induced vibration. *Journal of Fluids and Structures*, 22, 741 – 755.

PAÏDOUSSIS, M. P., MAVRIPLIS, D. et PRICE, S. J. (1984). A potential-flow theory for the dynamics of cylinder arrays in cross-flow. *Journal of Fluid Mechanics*, 146, 227–252.

PAÏDOUSSIS, M. P., PRICE, S. J. et DE LANGRE, E. (2011). *Fluid-structure interactions : cross-flow induced instabilities*. Cambridge University Press, Cambridge.

PAÏDOUSSIS, M. P., PRICE, S. J. et MUREITHI, N. W. (1993). Nonlinear and chaotic dynamics of a two-degree-of-freedom analytical model for a rotated triangular array in cross-flow. *Journal of fluids and structures*, 7, 497–520.

PAÏDOUSSIS, M. P., PRICE, S. J. et MUREITHI, N. W. (1996). On the virtual nonexistence of multiple instability regions for some heat-exchanger arrays in crossflow. *Journal of fluids engineering*, 118, 103–109.

PAÏDOUSSIS, M. P., PRICE, S. J., NAKAMURA, T., MARK, B. et MUREITHI, N. W. (1989). Flow-induced vibrations and instabilities in a rotated-square cylinder array in crossflow. *Journal of Fluids and Structures*, 3, 229–254.

PELLETIER, D. (1999). Adaptive finite element computations of complex flows. *Int. J. Numer. Meth. Fluids*, 31, 189–202.

PELLETIER, E., BÉGUIN, C. et ETIENNE, S. (2014). Simple model for bubble-wall interaction. *ASME 2014 Pressure Vessels and Piping Conference*. American Society of Mechanical Engineers.

PERROT, E. (2011). *Forces d'excitation vibratoire dans un faisceau de tubes en configuration triangulaire normale soumis à un écoulement diphasique*. Mémoire de maîtrise, École Polytechnique de Montréal.

PETTIGREW, M. J. et KNOWLES, G. D. (1997). Some aspects of heat-exchanger tube damping in two-phase mixtures. *Journal of fluids and structures*, 11, 929–945.

PETTIGREW, M. J., ROGERS, R. J. et AXISA, F. (2011). Damping of heat exchanger tubes in liquids : Review and design guidelines. *Journal of pressure vessel technology*, 133, 1–12.

PETTIGREW, M. J., SYLVESTRE, Y. et CAMPAGNA, A. O. (1978). Vibration analysis of heat exchanger and steam generator designs. *Nuclear Engineering and Design*, 48, 97 – 115.

PETTIGREW, M. J. et TAYLOR, C. E. (1991). Fluidelastic instability of heat exchanger tube bundles ; review and design recommendations. *Journal of Pressure Vessel Technology*, 113, 242–256.

PETTIGREW, M. J. et TAYLOR, C. E. (1994). Two-phase flow-induced vibration : an overview. *Journal of Pressure Vessel Technology*, 116, 233–253.

PETTIGREW, M. J. et TAYLOR, C. E. (2004). Damping of heat exchanger tubes in two-phase flow : review and design guidelines. *Journal of pressure vessel technology*, 126, 523–533.

PETTIGREW, M. J., TAYLOR, C. E., JANZEN, V. P. et WHAN, T. (2002). Vibration behavior of rotated triangular tube bundles in two-phase cross flows. *Journal of pressure vessel technology*, 124, 144–153.

PETTIGREW, M. J., TAYLOR, C. E. et KIM, B. S. (1989). Vibration of tube bundles in two-phase cross-flow : Part 1—hydrodynamic mass and damping. *Journal of Pressure Vessel Technology*, 111, 466–477.

PLAGNARD, T., BÉGUIN, C. et ÉTIENNE, S. (2014). Predicting fluidelastic instability in tube array with potential theory. *ASME 2014 Pressure Vessels and Piping Conference*. American Society of Mechanical Engineers.

PRASSER, H.-M., BEYER, M., BÖTTGER, A., CARL, H., LUCAS, D., SCHAFFRATH, A., SCHUTZ, P., WEISS, F.-P. et ZSCHAU, J. (2005). Influence of the pipe diameter on the structure of the gas-liquid interface in a vertical two-phase pipe flow. *Nuclear technology*, 152, 3–22.

PRICE, S. J. (1995). A review of theoretical models for fluidelastic instability of cylinder arrays in cross-flow. *Journal of Fluids and Structures*, 9, 463–518.

PRICE, S. J. (2001). An investigation on the use of connors' equation to predict fluidelastic instability in cylinder arrays. *Journal of pressure vessel technology*, 123, 448–453.

PRICE, S. J. et PAÏDOUSSIS, M. P. (1984). An improved mathematical model for the stability of cylinder rows subject to cross-flow. *Journal of Sound and Vibrations*, 97, 615–640.

PRICE, S. J. et PAÏDOUSSIS, M. P. (1986). A single-flexible-cylinder analysis for the fluidelastic instability of an array of flexible cylinders in cross-flow. *Journal of fluids engineering*, 108, 193–199.

RAZZAQUE, M. M., AFACAN, A., LIU, S., NANDAKUMAR, K., MASLIYAH, J. H. et SANDERS, R. S. (2003). Bubble size in coalescence dominant regime of turbulent air–water flow through horizontal pipes. *International journal of multiphase flow*, 29, 1451–1471.

RIBOUX, G., RISSO, F. et LEGENDRE, D. (2010). Experimental characterization of the agitation generated by bubbles rising at high reynolds number. *Journal of Fluid Mechanics*, 643, 509–539.

ROBERTS, B. W. (1966). Low frequency, aeroelastic vibrations in a cascade of circular cylinders. *Mechanical Engineering Science Monograph*, 4.

ROIG, V. et LARUE DE TOURNEMINE, A. (2007). Measurement of interstitial velocity of homogeneous bubbly flows at low to moderate void fraction. *Journal of Fluid Mechanics*, 572, 87–110.

ROUMY, R. (1969). *Structure des écoulements diphasiques eau-air. Etude de la fraction de vide moyenne et des configurations d'écoulement*. CEN Saclay.

SAWADOGO, T., HAN, Y. et MUREITHI, N. W. (2014). Implementation in vibic of an improved time-domain simulation model for fluidelastic instability in tube arrays. *ASME 2014 Pressure Vessels and Piping Conference*. American Society of Mechanical Engineers.

SAWADOGO, T. et MUREITHI, N. W. (2014a). Fluidelastic instability study in a rotated triangular tube array subject to two-phase cross-flow. part i : Fluid force measurements and time delay extraction. *Journal of Fluids and Structures*, 49, 1–15.

SAWADOGO, T. et MUREITHI, N. W. (2014b). Fluidelastic instability study on a rotated triangular tube array subject to two-phase cross-flow. part ii : Experimental tests and comparison with theoretical results. *Journal of Fluids and Structures*, 49, 16–28.

SCOTT, P. (1987). *Flow Visualization of Cross-flow Induced Vibrations in Tube Arrays*. Mémoire de maîtrise, McMaster University, Hamilton, Ontario, Canada.

SENEZ, H. et ÉTIENNE, S. (2011). Development of a numerical model to represent two-phase flow configurations in a tube bundle. *ASME 2011 Pressure Vessels and Piping Conference*. American Society of Mechanical Engineers, 195–209.

SHAHRIARY, S., MUREITHI, N. W. et PETTIGREW, M. J. (2007). Quasi-static forces and stability analysis in a triangular tube bundle subjected to two-phase cross-flow. *ASME 2007 Pressure Vessels and Piping Conference*. American Society of Mechanical Engineers, 245–252.

SHEW, W. L., PONCET, S. et PINTON, J.-F. (2006). Force measurements on rising bubbles. *Journal of Fluid Mechanics*, 569, 51–60.

SIMPSON, A. et FLOWER, J. (1977). An improved mathematical model for the aerodynamic forces on tandem cylinders in motion with aeroelastic applications. *Journal of Sound and Vibration*, 51, 183 – 217.

TAITEL, Y. et DUKLER, A. E. (1976). A model for predicting flow regime transitions in horizontal and near horizontal gas-liquid flow. *AIChE Journal*, 22, 47–55.

TANAKA, H. et TAKAHARA, S. (1980). Unsteady fluid dynamic force on tube bundle and its dynamic effect on vibration. *Flow-Induced Vibration of Power Plant Components - PVP New York ASME*, 41, 77–92.

TANAKA, H. et TAKAHARA, S. (1981). Fluidelastic vibration of tube array in cross-flow. *Journal of Sound and Vibration*, 77, 19–37.

TANAKA, H., TAKAHARA, S. et OHTA, K. (1983). Flow-induced vibration of tube arrays with various pitch-to-diameter ratios. *ASME Journal of Pressure Vessel Technology*, 104, 168–174.

TOMIYAMA, A., CELATA, G. P., HOSOKAWA, S. et YOSHIDA, S. (2002). Terminal velocity of single bubbles in surface tension force dominant regime. *International Journal of Multiphase Flow*, 28, 1497–1519.

UCHIYAMA, T. (2003). Numerical prediction of added mass and damping for a cylinder oscillating in confined incompressible gas–liquid two-phase mixture. *Nuclear engineering and design*, 222, 68–78.

VAN BEEK, A. (2006). *Advanced engineering design : lifetime performance and reliability*, vol. 1.

VIOLETTE, R., PETTIGREW, M. J. et MUREITHI, N. W. (2006). Fluidelastic instability of an array of tubes preferentially flexible in the flow direction subjected to two-phase cross flow. *Journal of pressure vessel technology*, 128, 148–159.

WATTEAUX, R. (2008). *Étude des facteurs d'influence d'un faisceau de cylindres dans un écoulement transverse à bas régime*. Mémoire de maîtrise, École Polytechnique de Montréal.

WATTEAUX, R., MUREITHI, N. et PELLETIER, D. (2007). Determination of Coupling Force Derivatives in Tube Bundles Using the Shape Sensitivity Equation Method. *ASME 2004 Pressure Vessels and Piping Conference*. American Society of Mechanical Engineers, San Antonio, TX, United states, 263–270.

WEAVER, D. S. et FITZPATRICK, J. A. (1988). A review of cross-flow induced vibrations in heat exchanger tube arrays. *Journal of Fluids and Structures*, 2, 73 – 93.

WEAVER, D. S. et GROVER, L. K. (1978). Cross-flow induced vibrations in a tube bank—turbulent buffeting and fluid elastic instability. *Journal of Sound and Vibration*, 59, 277–294.

WEAVER, D. S. et LEVER, J. H. (1977). Tube frequency effects on cross flow induced vibrations in tube arrays. *Proceedings of the Fifth Biennial Symposium on Turbulence*. vol. 1, 323–331.

YEUNG, H. C. et WEAVER, D. S. (1983). The effect of approach flow direction on the flow-induced vibrations of a triangular tube array. *Journal of Vibration and Acoustics*, 105, 76–81.

ZHU, J. Z. et ZIENKIEWICZ, O. C. (1987). A simple error estimator and adaptive procedure for pratical engineering analysis. *Int. J. Numer. Meth. Eng.*, 24, 337–357.

ZUBER, N. (1964). On the dispersed two-phase flow in the laminar flow regime. *Chemical Engineering Science*, 19, 897–917.

ZUBER, N. et HENCH, J. (1962). Steady state and transient void fraction of bubbling systems and their operating limits (part i, steady state operation). *General Electric Report 62GL100*.

ANNEXE A

Résultats expérimentaux

Cette annexe présente quelques résultats expérimentaux intermédiaires en complément à l'article du chapitre 3. La plupart de ces résultats ont été tirés de l'article de conférence par Charreton *et al.* (2013) aux Proceedings of ASME Pressure Vessels and Piping, Paris.

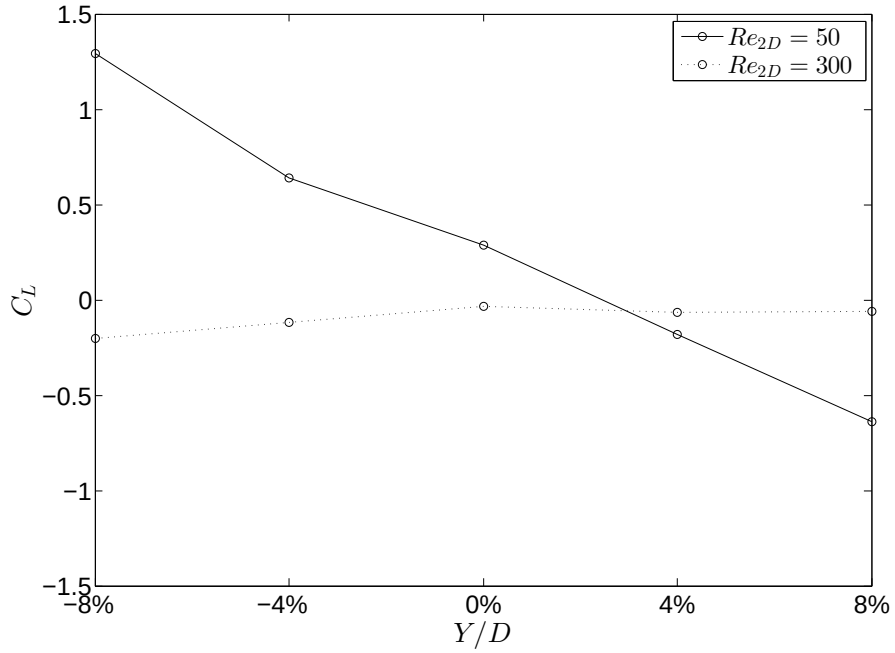

Figure A.1 Coefficient de portance en fonction du déplacement du cylindre pour deux nombres de Reynolds locaux. Remarquez l'inversion de signe de $\partial C_L/\partial y$.

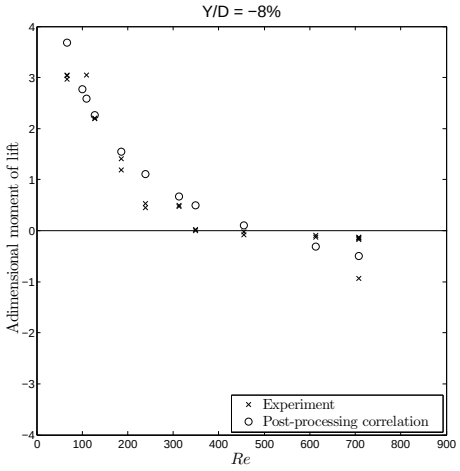

(a) $Y/D = -8\%$.

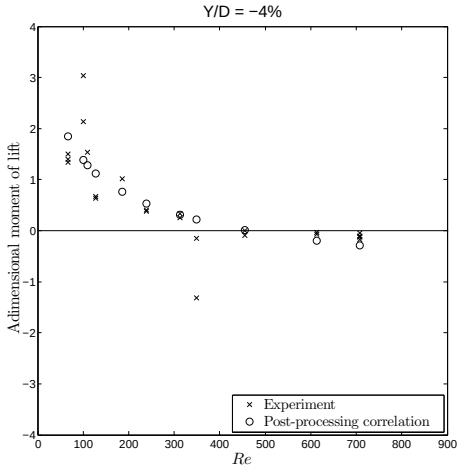

(b) $Y/D = -4\%$.

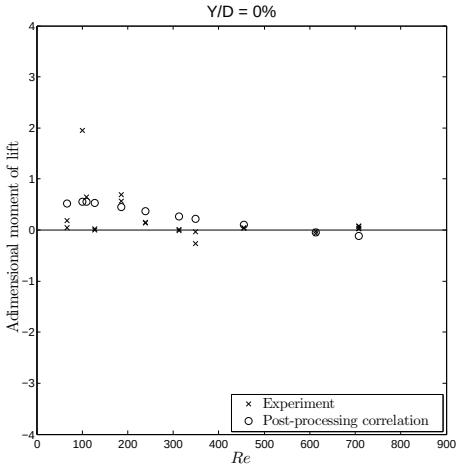

(c) $Y/D = 0\%$.

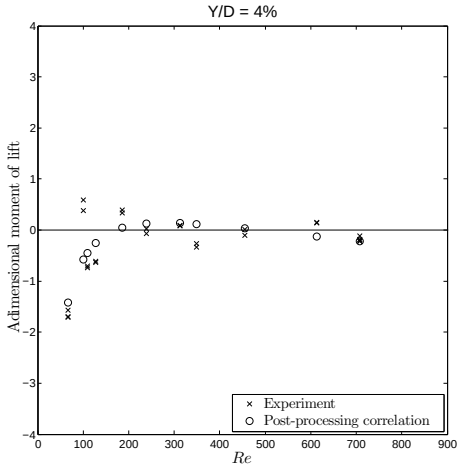

(d) $Y/D = 4\%$.

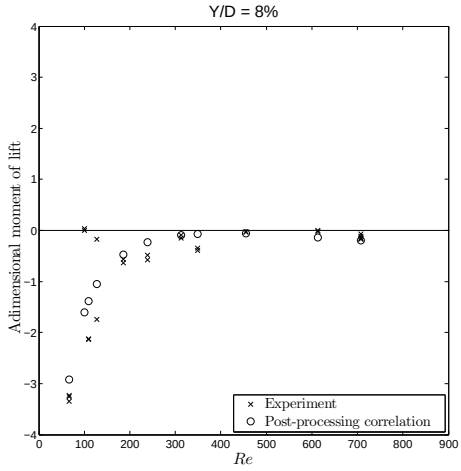

(e) $Y/D = 8\%$.

Figure A.2 Moments adimensionnels expérimentaux et théoriques après optimisation.